Ion-Atom Collisions:
a time-dependent density-functional-theory perspective

MATTHEW BAXTER

A DISSERTATION SUBMITTED TO THE FACULTY OF GRADUATE STUDIES IN PARTIAL
FULFILLMENT OF THE REQUIREMENTS FOR THE DEGREE OF DOCTOR OF PHILOSOPHY

GRADUATE PROGRAMME IN THE DEPARTMENT OF PHYSICS AND ASTRONOMY
YORK UNIVERSITY
TORONTO ONTARIO

November, 2017

Abstract

Time-dependent density functional theory (TDDFT) is an alternate formulation of time-dependent N-body quantum mechanics which allows one to describe a system via the single-particle density, n, rather than the full N-body wave function. While this reformulation is in theory exact in practice it necessitates at least two approximations. First, the exchange-correlation potential which encodes the two-particle interactions present in the time-dependent Schrödinger equation into the language of the single-particle description is not precisely known. Even if one had perfect knowledge of this potential a further approximation would be required when attempting to extract the values of observables as the exact relation between the one-particle density and most observables of interest is also unknown.

This dissertation investigates these issues using ion-atom collision systems as a testbed. First, the observable problem is explored in antiproton-helium, proton-helium, and He^{2+}-He collision systems. Total cross sections for all charge transfer processes in these systems, the observables of choice in the present situation, are determined using a two-centred extension of a correlation-integral model that was originally applied to single-centred situations.

Following this theoretical total cross section results for all ionization/capture processes in the He^+-He collision system are presented in the approximate impact energy range 10-1000 keV/amu. Calculations were performed within the framework of a spin-dependent extension of TDDFT. These cross sections are used as a benchmark to test an accurate exchange-correlation potential generated via the Krieger-Li-Iafrate approximation applied within the exchange-only limit in which correlation is ignored. The results of two models, one where electron translation factors in the orbitals used to calculate the potential are ignored and another where partial electron translation factors are included, are compared with available experimental data as well as a selection of previous theoretical calculations.

CONTENTS

List of Tables

LIST OF FIGURES

CHAPTER 1

INTRODUCTION

Atomic collision systems are of interest both on their own merits, and for their potential in applications. As a particular example the He^+-He collision system, a focus of a large portion of the present work, is applicable in such diverse areas as fusion reactors [1, 2], astrophysics [3, 4], and dark matter detection [5].

From the point of view of theory, atomic collision systems are often explored as testbeds for few-electron quantum dynamics. A helium-like target, consisting of two electrons and a nucleus, and a bare projectile represent the archetypal few-electron collision system. The simplest example of such a system uses an antiproton, the negatively charged antiparticle of the proton, as the projectile. With a negative projectile the collision may be treated as an effective one-centred system which involves electron excitation and ionization.

One might envision more complex systems by simply increasing the number of electrons on the target, however, a more useful course is to replace the negatively charged projectile with one that is positively charged. With a positive projectile one must consider electron transfer in addition to ionization processes.

Even more complex collision systems may be created by adding active electrons to the projectile. With this addition one must consider various combinations of ionization from both centres as well as transfers between target and projectile.

This chain of accruing complexity essentially describes the path of this work in which a series of increasingly involved collision systems are investigated. This

sequence begins with a negative projectile, that is with an antiproton-helium system. Following this two systems, proton-helium (p-He) and fully stripped helium ions on helium (He^{2+}-He), involving positively charged projectiles are investigated. Finally, a singly charged helium ion incident on a helium atom (He^+-He), a system which contains one electron on the projectile and two on the target, was studied.

Solving the Schrödinger equation describing a system of more than two particles is computationally taxing, even for a small number of particles (three or more). Thus, the so called few-body problem tests the limits of current computational power. As an example, recently Gainullin and Sonkin presented a method for directly solving the time-dependent Schrödinger equation [6]. In this work the authors performed a benchmark proton-hydrogen collision calculation. With code running on 16 GPUs their single electron calculation was completed in 16 hours. The authors then make the claim that similar performance for a two-electron system would require access to 1000 GPUs.

Perhaps the next best option for tackling a many-body system is the close-coupling method [7]. Rather then determine the N-body wave function directly this method relies on a truncated basis expansion to approximate the exact wave function. A balance must then be found between numerical accuracy and computational intensity. As one increases the number of included basis states the approximation will approach the exact solution provided the basis used is complete, however, the effort required to achieve a solution also approaches that of a direct calculation.

A popular alternative comes from perturbation theory. One makes use of the Born series to describe the transition matrix with respect to free-particle states which represent the collision system at asymptotic times before and after the collision. A general feature of perturbative methods is that they have a limited range of applicability. The Born computable series is generally convergent at high energies and for weak interactions (in the context of ion-atom collisions this means low charge-state projectiles). These methods can be improved and extended into the intermediate energy regime by clever choices for the unperturbed states [8, 9] (i.e. by using distorted instead of plane waves).

Another alternative is the classical trajectory Monte Carlo method [10]

(CTMC). In the CTMC multiple calculations are performed where particles are evolved according to the classical Hamiltonian with initial conditions randomly selected from a distribution, usually one describing the quantum mechanical initial state in coordinate or momentum space. The primary failing of this method is its classical nature: the CTMC is fundamentally incapable of capturing purely quantum mechanical phenomena such as tunnelling and exchange.

Time-dependent density functional theory [11, 12] (TDDFT), the method of choice of the current work, attempts to provide a solution to all of the problems inherent in the above mentioned methods. By reformulating the N-body problem in terms of the one-particle density rather than the N-electron wave function the problem is effectively reduced to the complexity of a single-particle calculation. Additionally as the reformulation is theoretically exact it avoids the restricted applicability of perturbative methods. While it may seem strange that all of the complexity of the N-body wave function can be captured by a single particle quantity like the one-particle density, TDDFT has been successfully applied to a wide range of problems. Most obviously given the title of this dissertation TDDFT has been applied to ion-atom collisions [13]. Many of the same techniques of this realm can be applied to the related field of laser interactions with atoms and molecules (see for example Chapters 24 and 25 in Ref. [11]). TDDFT has also been used to determine properties of extended solids (e.g. ionic crystals) [14] and of complex organic and inorganic molecules [15].

While useful TDDFT is not without its own drawbacks. One downside is that, unlike in standard quantum mechanics, observables are not readily calculable as they are from the many-electron wave function. While the Runge-Gross theorem [16] guarantees that all observables are expressible as functionals of the one-particle density, exact expressions are only available in a limited number of cases [17]. In most situations one is then forced to work with approximate observable functionals.

Additionally, when working within the context of TDDFT one typically determines the one-particle density via an auxiliary system of non-interacting particles. To obtain this a new potential, the Kohn-Sham potential (KS), which encodes the interacting system into the language of non-interacting particles, must be introduced. As with the observables, mentioned above, this potential is an unknown

functional of the one-particle density and, as such, must also be approximated.

This dissertation addresses both issues in the context of ion-atom collisions. The relevant DFT background is presented in Chap. 2. Chapter 3 of this work largely concerns itself with an investigation of the observable problem using antiproton-, proton-, and He^{2+}-He collision systems as testbeds. Here a correlation integral model [18] that was adapted to describe single-centred collision problems [19] is extended to characterize two-centred systems. The second of the main problems of DFT is explored in Chap. 4 where a procedure for accurately approximating the Kohn-Sham potential is implemented and applied to the He^+-He collision system. Finally, a summary of the results and conclusions of this work are given in Chap. 5.

Atomic units ($\hbar = m_e = e = 4\pi\epsilon_0 = 1$) are used throughout unless otherwise stated.

CHAPTER 2

DENSITY FUNCTIONAL THEORY

This chapter concerns itself with a brief introduction to the world of density-functional theory, both ground-state [20] (DFT) and time-dependent [11, 12, 21] (TDDFT). This discussion begins with an overview of various existence theorems central to density functional theory (Sec. 2.1). Next, the Kohn-Sham equations are introduced in Sec. 2.2. More practical matters are considered when two of the main problems of density functional theory, the observable problem (Sec. 2.3) and the determination of the exchange-correlation potential (Sec. 2.4) are presented. The discussion of the xc-potential is focused on the optimized potential method (Sec. 2.4.1) and the Krieger-Li-Iafrate approximation (Sec. 2.4.2).

2.1   DFT AND TDDFT EXISTENCE THEOREMS

In the standard treatment of non-relativistic many-body quantum mechanics a system is described by a wave function Ψ which, depending upon the situation, is determined by either the time-dependent Schrödinger equation (TDSE)

$$\hat{H}(t)\Psi(t) = i\frac{\mathrm{d}\Psi(t)}{\mathrm{d}t},\tag{2.1}$$

or the stationary Schrödinger equation (SSE)

$$\hat{H}\Psi = E\Psi.\tag{2.2}$$

If the system in question consists of N electrons then Ψ becomes a function of N position variables $\mathbf{r}_i$ and spin variables $\sigma_i = \uparrow, \downarrow$. The Hamiltonian, $\hat{H}$, may be decomposed into a kinetic energy term

$$\hat{T} = -\frac{1}{2} \sum_{j=1}^{N} \Delta_j, \tag{2.3}$$

an electron-electron term

$$\hat{V}_{ee} = \frac{1}{2} \sum_{k \neq j}^{N} \frac{1}{|\mathbf{r}_k - \mathbf{r}_j|}, \tag{2.4}$$

and a, possibly, time-dependent external potential

$$\hat{V}_{\text{ext}} = \sum_{j=1}^{n} v_{\text{ext}}(\mathbf{r}_j, \sigma_j, t). \tag{2.5}$$

The function $\hat{V}_{\text{ext}}$ contains all of the one-body interactions, including the nuclear and any external potentials.

Given the one-particle electronic density

$$n(\mathbf{r}, t) = N \sum_{\sigma_1 \ldots \sigma_N} \int d^3 r_2 \ldots d^3 r_N \, |\Psi(\mathbf{r}, \sigma_1, \mathbf{r}_2, \sigma_2, \ldots, \mathbf{r}_N, \sigma_N)|^2 \tag{2.6}$$

the Hohenberg–Kohn theorem [22] in the stationary case and the Runge-Gross theorem [16] in the time-dependent case establish a one-to-one mapping between the one-particle density n and the external potential $\hat{V}_{\text{ext}}$. The potential is then a unique functional of the one-particle density

$$\hat{V}_{\text{ext}} = \hat{V}_{\text{ext}}[n]. \tag{2.7}$$

It should be noted that for time-dependent systems this mapping is unique only up to the addition of an arbitrary time-dependent function. As this serves only to introduce a phase into the associated wave function $\Psi[\hat{V}_{\text{ext}}]$ it can be safely ignored in all future discussions. For more on this see the discussion following

Eq. (2.16).

In general, the time-dependent external potential will also be a functional of the initial state of the system Ψ_0. For a system consisting of a single electron no such initial-state dependence exists [23, 24], for two or more electrons the initial-state dependence is not necessarily unique [25–28]. Fortunately, in most cases of interest initial-state dependence is not an issue. As an example any system initially in the ground state, as is the case in this work, may appeal to the Hohenberg-Kohn theorem to guarantee that functionals depend uniquely on the initial state.

We have formulated the density-potential mapping for an explicitly spin-dependent system, it then must be noted that the original existence theorems were not formulated in such general terms. Luckily, generalizations for both the stationary [29, 30] and time-dependent [31] cases to spin-polarized systems exist.

2.2 THE KOHN-SHAM EQUATIONS

In practice the correspondence between the density and potential is used to map the interacting many-body SSE or TDSE onto an auxiliary non-interacting system. The density-potential mappings discussed in the previous section allow one to rewrite the interacting system in terms of an auxiliary system of non-interacting particles described by the functions $\varphi_{j\sigma}$ ($j = 1, \ldots, N_\sigma$, $N = N_\uparrow + N_\downarrow$) with

$$n = \sum_\sigma \sum_{j=1}^{N_\sigma} \left| \varphi_{j\sigma} \right|^2,$$ (2.8)

where n is the one-particle density of the fully interacting system. The orbitals $\varphi_{j\sigma}$ are determined through the stationary or time-dependent Kohn-Sham equations [29, 32–34] (SKS, TDKS respectively)

$$\left(-\frac{\Delta}{2} + v_{\text{KS}}^\sigma[n_\uparrow, n_\downarrow](\mathbf{r}) \right) \varphi_{j\sigma}(\mathbf{r}) = \epsilon_{j\sigma} \varphi_{j\sigma}(\mathbf{r}),$$ (2.9)

$$i\frac{\partial}{\partial t} \varphi_{j\sigma} = \left(-\frac{\Delta}{2} + v_{\text{KS}}^\sigma[n_\uparrow, n_\downarrow](\mathbf{r}, t) \right) \varphi_{j\sigma}(\mathbf{r}, t),$$ (2.10)

where the $\epsilon_{j\sigma}$ appearing in Eq. (2.9) are the Kohn-Sham eigenvalues and the quantities $n_\uparrow$, $n_\downarrow$ are the spin-up/down one-particle densities defined by

$$n_\sigma = \sum_{j=1}^{N_\sigma} \left|\varphi_{j\sigma}\right|^2,\tag{2.11}$$

such that

$$n = n_\uparrow + n_\downarrow.\tag{2.12}$$

The potential in Eqs. (2.9) and (2.10) is known as the Kohn-Sham potential. This potential may be simplified by splitting it into a series of less complex objects

$$v_{\text{KS}}^\sigma[n_\uparrow, n_\downarrow] = v_{\text{ext}} + v_{\text{H}}[n] + v_{\text{xc}}^\sigma[n_\uparrow, n_\downarrow].\tag{2.13}$$

The first term in this expression is the external potential (see the right hand side of Eq. 2.5). The next term is the Hartree screening potential

$$v_{\text{H}}(\mathbf{r}, t) = \int \frac{n(\mathbf{r}', t)}{|\mathbf{r} - \mathbf{r}'|}\, \mathrm{d}^3 r'.\tag{2.14}$$

The last term is the exchange-correlation potential which encodes the complicated electron-electron interaction potential into the language of the non-interacting system. For convenience this is often further broken down into separate exchange and correlation potentials

$$v_{\text{xc}}^\sigma = v_{\text{x}}^\sigma + v_{\text{c}}^\sigma.\tag{2.15}$$

2.3 OBSERVABLES

In the standard treatment of many-body quantum mechanics there is a well established process for calculating observables from the full many-body wave function describing the system. For any solution Ψ, unique up to a phase factor, of the SSE or TDSE and any observable $\hat{O}$ we immediately have the unique functional

$$O[\Psi] = \langle\Psi|\hat{O}|\Psi\rangle,\tag{2.16}$$

so long as $\hat{O}$ contains no time-derivative terms.

The density-potential mappings of Sec. 2.1 provide the relation

$$n \mapsto \hat{V}_{\text{ext}}[n] + c(t). \tag{2.17}$$

As the function c only serves to introduce another phase factor we may use the uniqueness of solutions of the SSE/TDSE to define a map

$$n \mapsto \hat{V}_{\text{ext}} \mapsto \Psi \mapsto O \tag{2.18}$$

or, $O = O[n]$.

In principle all observables are functionals of the one-particle density. However, in practice the exact functional is only known in a handful of cases [17, p. 211-213]. This discussion will be made far more explicit in Sec. 3.2 where the difficulties of extracting observables, total cross sections in this case, are described in detail.

2.4   XC-POTENTIAL

Consider the energy functional for the interacting system

$$E[n] = \langle \Psi[n] | \hat{H} | \Psi[n] \rangle = T[n] + E_{ee}[n] + E_{\text{ext}}[n] \tag{2.19}$$

where the energies on the right-hand side are the contributions from the constituent operators Eq. (2.3)–(2.5). Similarly, we may define the energy functional for the non-interacting, KS, system as

$$E_s[n] = T_s[n] + E_{\text{xc}}[n] + E_{\text{H}}[n] + E_{\text{ext}}[n]. \tag{2.20}$$

Making use of the fact that the energy is a unique functional of the density it follows that

$$E_{\text{xc}} = T - T_s + E_{ee} - E_{\text{H}}. \tag{2.21}$$

9

Finally making use of the fact that the ground-state one-particle density will minimize the energy it follows that

$$\frac{\delta E_{\text{xc}}[n]}{\delta n_\sigma(\mathbf{r})} = v_{\text{xc}}^\sigma[n](\mathbf{r}). \tag{2.22}$$

The universality of the xc-functional [20] means that once an approximation to E_{xc} has been found we may apply the resulting potential to any system. Of course, some approximations will be better suited to certain situations.

There are a few caveats to apply Eq. (2.22). First, the functional is only defined for the set of ground-state v-representable densities, those densities which arise as ground-state solutions of the SSE for some potential v. The second problem follows from the first. Due to the fact that not all densities are v-representable [35–37], one must establish that the set of functions for which the functional is defined is dense enough to ensure the existence of the functional derivative. For densities defined on a lattice [38] as well as the general case [35, 39–43] both the issue of v-representability and the existence of the functional derivatives of the energy functional have been addressed.

In the case of TDDFT one can no longer rely upon minimizing the energy functional when seeking solutions. Instead one looks for stationary points of the quantum mechanical action [44]

$$A[n] = \int_{t_i}^{t_f} \mathrm{d}t \, \langle \Psi[n] | i \frac{\partial}{\partial t} - \hat{H}(t) | \Psi[n] \rangle \,. \tag{2.23}$$

In analogy to the ground-state case the exchange-correlation part of the action may be defined in terms of the difference between the actions for the interacting and non-interacting systems. We then find at a stationary point:

$$\frac{\delta A_{\text{xc}}[n]}{\delta n_\sigma(\mathbf{r}, t)} = v_{\text{xc}}^\sigma[n](\mathbf{r}, t). \tag{2.24}$$

In addition to similar issues of v-representability and functional differentiability the action Eq. (2.23) does not distinguish the direction of time and thus its naive use may lead to violations of causality [45]. The existence of functional derivatives has been established in a similar style as in the stationary case [46].

The problem of which densities are v-representable has also been solved [47]. The causality problem may be solved in several ways including extending the time domain to the Keldysh contour [48] and relaxing the boundary condition on one end point of the time interval [49].

The simplest explicit density functional is the local density approximation [32] (LDA). At its simplest the LDA approximates the energy functional of a general system as that of the homogeneous electron gas (HEG)

$$E^{\text{LDA}}[n] = \int \mathrm{d}^3 r \, n(\mathbf{r}) \epsilon_{\text{HEG}}(n), \tag{2.25}$$

where ϵ_{HEG} is the energy density of the HEG, which is a function of the density of the gas. Exchange contributions to ϵ_{HEG} have been determined analytically [50].

Taking things further one is led to the hierarchy of increasingly complex generalized gradient approximations and hybrid functionals [51]. For time-dependent systems one may simply apply one of the many ground-state functionals to arrive at an adiabatic approximation in which the xc-potential depends only on the instantaneous density. Going beyond the adiabatic approximation is possible, however such functionals are much more complex. As an example the fully time-dependent version of the LDA, the local deformation approximation [52, 53] (TDLDefA) can be mentioned. A complete description of the time-time dependent xc-potential is a complicated task. Such a model would need to capture a wide range of phenomena. It has been shown that derivative discontinuities [54] and memory effects (see, for instance, the discussions in [11] and [12]) are important.

2.4.1 OPTIMIZED POTENTIAL METHOD

An alternate approach to the explicit density functionals mentioned above is to employ an implicit density functional. For an implicit functional the xc-potential may be determined indirectly from the KS-orbitals, and their eigenvalues, through a procedure known as the optimized potential method [55, 56] (OPM) for which there are several derivations [55–60].

Without reproducing too many long equations one may use Eq. (2.22) and several applications of the chain rule for functional derivatives to arrive at ($c.c.$

denoting the complex conjugate of the preceding term)

$$
\begin{aligned}
v_{\text{xc}}^{\sigma}(\mathbf{r}) = \int \mathrm{d}^3 r' \frac{\delta v_{\text{KS}}^{\sigma}(\mathbf{r}')}{\delta n_{\sigma}(\mathbf{r})} \\
\times \sum_{j} \left\{ \int \mathrm{d}^3 r'' \left[\frac{\delta E_{\text{xc}}}{\delta \varphi_{j\sigma}(\mathbf{r}'')} \frac{\delta \varphi_{j\sigma}(\mathbf{r}'')}{\delta v_{\text{KS}}^{\sigma}(\mathbf{r}')} + c.c. \right] + \frac{\delta \epsilon_k}{\delta v_{\text{KS}}^{\sigma}(\mathbf{r}')} \frac{\partial E_{\text{xc}}}{\partial \epsilon_k} \right\}
\end{aligned}
\tag{2.26}
$$

from which the OPM integral equation is then derived. A similar derivation for the time-dependent case leads to the time-dependent OPM equation [61]. In either situation an appropriate choice of E_{xc} or A_{xc} can include both exchange and correlation effects [59, 61]. With that said the OPM is typically used to calculate exact exchange using the functional

$$
\begin{aligned}
A_{\text{x}}[\varphi_{j\sigma}(\mathbf{r}, t)] &= \int \mathrm{d}t \, E_{\text{x}}[\varphi_{j\sigma}(\mathbf{r}, t)] \\
&= -\frac{1}{2} \int \mathrm{d}t \sum_{\sigma} \sum_{j,k} \int \mathrm{d}^3 r \mathrm{d}^3 r' \\
&\quad \times \frac{\varphi_{j\sigma}^{*}(\mathbf{r}', t)\varphi_{k\sigma}^{*}(\mathbf{r}, t)\varphi_{j\sigma}(\mathbf{r}, t)\varphi_{k\sigma}(\mathbf{r}', t)}{|\mathbf{r} - \mathbf{r}'|}.
\end{aligned}
\tag{2.27}
$$

After some work the stationary version of the exchange-only OPM will then follow from Eq. (2.26) and the Fock exchange energy in Eq. (2.27). The result may be expressed, adapting the notation of [62], as

$$
\sum_{j} \int \mathrm{d}^3 r' \left[v_{\text{x}}^{\sigma}(\mathbf{r}') - \tilde{v}_{j\sigma}(\mathbf{r}') \right] G_{j\sigma}(\mathbf{r}', \mathbf{r})\varphi_{j\sigma}^{*}(\mathbf{r}')\varphi_{j\sigma}(\mathbf{r}) + c.c. = 0,
\tag{2.28}
$$

where $G_{j\sigma}$ are the Green's functions

$$
G_{j\sigma}(\mathbf{r}, \mathbf{r}') = \sum_{k \neq j} \frac{\varphi_{k\sigma}(\mathbf{r})\varphi_{k\sigma}^{*}(\mathbf{r}')}{\epsilon_{k\sigma} - \epsilon_{j\sigma}}
\tag{2.29}
$$

and

$$
\tilde{v}_{j\sigma}(\mathbf{r}) = -\sum_{k} \int \mathrm{d}^3 r' \frac{\varphi_{j\sigma}^{*}(\mathbf{r}')\varphi_{k\sigma}^{*}(\mathbf{r}')\varphi_{k\sigma}(\mathbf{r})}{|\mathbf{r} - \mathbf{r}'| \, \varphi_{j\sigma}^{*}(\mathbf{r})}.
\tag{2.30}
$$

2.4.2 The Krieger-Li-Iafrate Approximation

Solving of the full OPM integral equation can be quite difficult. To aid in this process the Krieger-Li-Iafrate approximation [63] (KLI) may be used. One can think of KLI as a closure approximation where the complicated interactions between orbitals are simplified by the introduction of an average energy difference $\Delta \epsilon_\sigma \approx \epsilon_{k\sigma} - \epsilon_{j\sigma}$ in the Green's functions. Returning to the exchange-only example introduced earlier this approximation causes Eq. (2.28) to become

$$v_{\mathrm{x}}^\sigma(\mathbf{r}) = \frac{\sum\limits_j \varphi_{j\sigma}^*(\mathbf{r})\varphi_{j\sigma}(\mathbf{r})\left[\tilde{v}_{j\sigma}(\mathbf{r}) + \bar{v}_{j\sigma\mathrm{x}} - \bar{v}_{j\sigma}\right]}{n(\mathbf{r})}, \qquad (2.31)$$

where

$$\bar{v}_{j\sigma} = \int \mathrm{d}^3r \; \varphi_{j\sigma}^*(\mathbf{r})\varphi_{j\sigma}(\mathbf{r})\tilde{v}_{j\sigma}(\mathbf{r}) \qquad (2.32)$$

and $\bar{v}_{j\sigma\mathrm{x}}$ is defined similarly.

   If one then multiplies both sides of Eq. (2.31) by $\varphi_{l\sigma}^*(\mathbf{r})\varphi_{l\sigma}(\mathbf{r})$ and integrates over d^3r one is left with a set of linear equations for $\bar{v}_{l\sigma}^\sigma$. This approximation turns the complex OPM integral equation into a much simpler linear system of equations.

   It should be noted that while several variations of the KLI method exist [63–65] they differ by only a term proportional to $\partial E_{\mathrm{xc}}/\partial \epsilon_k$ which, for functionals such as the exact exchange functional that do not depend on the KS eigenvalues does not contribute. Of particular interest is the method of Ref. [64] where the the KLI is obtained from the exact OPM equation by neglecting certain higher order terms (i.e. if these terms are added to Eq. (2.31) the exact OPM is recovered). Later in this same work the authors incorporate an approximation to these higher order terms, the inclusion of which covers much of the difference between KLI and the full OPM, however even this approximation to the neglected portion of OPM is rarely included in practice. As one might expect the KLI approximation is also applicable in the time-dependent regime [66–68].

   For a wide range of systems KLI and the full OPM produce very similar results [60]. The success of both OPM and KLI potentials is due in part to the fact

that both capture the correct asymptotics of the exchange potential

$$\lim_{r \to \infty} v_{\mathrm{x}}^{\sigma}(\mathbf{r}) = -\frac{1}{r}. \tag{2.33}$$

This is not to say that the KLI is perfect, it is still an approximation. Both the exact and OPM exchange-correlation potentials satisfy

$$\int \mathrm{d}^3 r \; n(\mathbf{r}, t) \nabla v_{\mathrm{xc}}^{\sigma}(\mathbf{r}, t) = 0. \tag{2.34}$$

This relation is often referred to as the zero-force theorem, the name coming from the obvious interpretation that the force deriving from the exchange-correlation potential exerts no net force on the electron cloud. An unfortunate consequence of the KLI approximation is that it can lead to violations of the zero-force theorem which, in turn, can lead to auto-excitation [69]. This is particularly pertinent in collision systems where spurious excitations may artificially enhance electron transfer processes.

CHAPTER 3

BARE ION-HELIUM COLLISIONS

Correlation enters TDDFT calculations in two distinct ways. First of these is dynamic correlation, those effects which emerge from a fully time-dependent correlation potential. These are precisely the effects we ignore through the use of the frozen correlation model which is discussed alongside a description of the collision systems of interest in Sec. 3.1.

The second source of correlation comes from the density functional used in the determination of observables. This so-called functional correlation is the main focus of this chapter. The exploration of this topic begins in Sec. 3.2 were several observable functional approximations are introduced. The results of application of these models to p-He, He^{2+}-He, as well as $\bar{p}$-He collisions are presented and discussed in Sec. 3.4.

The analysis presented in this chapter closely follows that of [70]. Additionally, while some results for $\bar{p}$-He collision system are presented here the bulk of the theoretical underpinnings of this work are not, as this represents work undertaken during the completion of the author's Master's thesis [71]. The $\bar{p}$-He cross sections reproduced in this dissertation are an updated version of the previous results making use of the improved averaging scheme (Sec. 3.3) developed when investigating the p-He and He^{2+}-He systems.

3.1 COLLISION SYSTEM

For the current systems of interest, $\bar{p}$-He, p-He, and He^{2+}-He collisions, the TDKS [Eq. (2.10)] are greatly simplified. First, the initial state of the helium atom will be a spin-singlet. As a result of this we need only consider one KS-orbital

$$\varphi = \varphi_{1\uparrow} = \varphi_{1\downarrow}. \tag{3.1}$$

With this in mind all spin indices will be suppressed for the remainder of this chapter. An additional consequence of the spin-singlet nature of the system is that the exchange potential takes the form

$$v_{\text{x}} = -\tfrac{1}{2}v_{\text{H}}. \tag{3.2}$$

As in [19] the correlation potential v_{c} will be approximated using a frozen correlation model. This potential is determined by inverting the Kohn-Sham scheme for the density of an accurate multi-configuration Hartree-Fock [72] (MCHF) ground-state helium wave function. The details of this process can be found in [19, 71].

Finally, the external potential can be specified. For a collision system in the semi-classical approximation this consists of the Coulomb potentials of the nuclear centres of the target and projectile. We may write

$$v_{\text{ext}}(\mathbf{r}, t) = -\frac{Q_T}{r} - \frac{Q_P}{|\mathbf{r} - \mathbf{R}(t)|}, \tag{3.3}$$

where Q_T and Q_P are the charges of the target and projectile nuclei and $\mathbf{R}(t) = (b, 0, Vt)$ is the straight-line trajectory of the projectile with velocity V and impact parameter (distance of closest approach) b. In the current work we consider antiprotons, protons, and He^{2+} ions incident on helium atoms, thus $Q_T = 2$ and $Q_P = -1, 1$, and 2 respectively. Above impact energies of 1 keV/amu where the nuclear motion is well represented by a straight line the semi-classical approximation may be safely employed [13].

Having spent a few words addressing concerns at the lower end of our impact energy range it is only logical to turn ones eye to the other extreme. The largest

impact energy considered in this work, 2000 keV/amu, corresponds to an impact velocity $V \approx 9$ a.u. With the speed of light $c = 137$ a.u. a Lorentz factor γ may be determined

$$\gamma = \left(1 - \frac{V^2}{c^2}\right)^{-\frac{1}{2}} \approx 1.0027, \tag{3.4}$$

putting us safely in the non-relativistic regime.

The TDKS described above was solved with the basis generator method [73] (BGM) using a basis similar to the one employed in [74]. As in [19] the basis rooted in an x-only description of the helium atom in [74] is replaced by one that reflects the incorporation of the ground-state correlation potential. In the BGM we expand the time-dependent orbital in terms of the basis functions

$$\chi_k^{KJ}(\mathbf{r}, t) = W_T(r, \epsilon_T)^K W_P(\mathbf{r}, t, \epsilon_P)^J \chi_k^{00}(\mathbf{r}), \tag{3.5}$$

with

$$W_T(r, \epsilon_T) = \frac{1 - e^{-\epsilon_T r}}{r}, \tag{3.6}$$

$$W_P(\mathbf{r}, t, \epsilon_P) = \frac{1 - e^{-\epsilon_P |\mathbf{r} - \mathbf{R}(t)|}}{|\mathbf{r} - \mathbf{R}(t)|} \tag{3.7}$$

and χ_k^{00} the eigenstates of the initial Hamiltonian (in this case the ground-state Kohn-Sham system for the helium atom). In order to keep the number of states in the basis to a minimum and simplify the description only those states with $K = 0$ where included. This simplification has proved sufficient in the past [13]. The remaining regularizer is set to $\epsilon_P = 1$ and the basis chosen was similar to that of [74]. A more general two-centred version of the BGM (TC-BGM) which includes explicit basis states on both the target and the potential is also possible. The full machinery of the two-centred version will be discussed in the following chapter.

Before closing this section we will return a final time to the discussion of relativistic effects, this time in regards to the atomic orbitals. The primary effect of relativity on the orbitals is to contract or expand the orbitals. To lowest order in $1/c^2$ the change in average of the position operator for a relativistic hydrogen-like
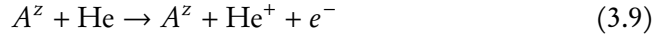
orbital follows the relation (see, for example, Ref. [75])

$$\langle \mathbf{r} \rangle_{\text{rel}} - \langle \mathbf{r} \rangle_{\text{nonrel}} \propto \frac{Qn}{c^2 \kappa}, \tag{3.8}$$

where $\kappa = j + 1/2$ wih total angular momentum quantum number j and Q the atomic charge. For the orbitals considered in this work n never exceeds 4, Q is at most 2, and κ is either 1/2, for spin singlet states, or 1 for atoms containing one (or three) electrons. All of this means that at worst the orbital distortion is on the order of 10^{-4}, and while the expression only holds for hydrogen-like orbitals the exact expression for a multi-electron atom does not disagree in a signifigant way [75]. With all this said it has been explicitly demonstrated that relativistic effects are negligible for helium collisions within the impact energy range considered in this work [76].

3.2 Approximating Observable Functionals

The discussion started in Sec. 2.3 may be elaborated upon by introducing the observables of interest for our ion-atom collision systems, the ionization and capture probabilities. For both negatively and positively charged projectiles we must consider the two pure ionization processes, single ionization

$$A^z + \text{He} \rightarrow A^z + \text{He}^+ + e^- \tag{3.9}$$

and double ionization

$$A^z + \text{He} \rightarrow A^z + \text{He}^{2+} + 2e^-, \tag{3.10}$$
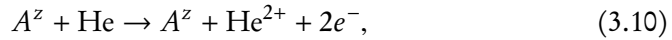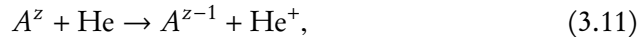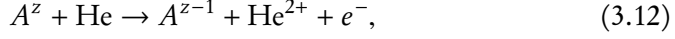
where $A^z = \text{H}^+$ or p for protons, $A^z = \text{He}^{2+}$, or $A^z = \bar{p}$, and assuming we exclude processes involving only excitation of the target.
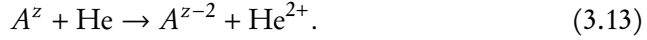
For positively charged projectiles additional processes involving capture must also be included. The three additional channels are single capture

$$A^z + \text{He} \rightarrow A^{z-1} + \text{He}^+, \tag{3.11}$$

transfer ionization

$$A^z + \text{He} \rightarrow A^{z-1} + \text{He}^{2+} + e^-,$$ (3.12)

and double capture

$$A^z + \text{He} \rightarrow A^{z-2} + \text{He}^{2+}.$$ (3.13)

The probabilities of finding an electron on the target (T), on the projectile (P), or in the continuum (I) are given exactly in terms of the two-particle density $\rho = 2|\Psi|^2$ by

$$p^{TT} = \frac{1}{2} \int_T \int_T d^3 r_1 d^3 r_2 \; \rho(\mathbf{r}_1, \mathbf{r}_2, t_f),$$ (3.14a)

$$p^{TI} = \int_T \int_I d^3 r_1 d^3 r_2 \; \rho(\mathbf{r}_1, \mathbf{r}_2, t_f),$$ (3.14b)

$$p^{II} = \frac{1}{2} \int_I \int_I d^3 r_1 d^3 r_2 \; \rho(\mathbf{r}_1, \mathbf{r}_2, t_f),$$ (3.14c)

$$p^{TP} = \int_T \int_P d^3 r_1 d^3 r_2 \; \rho(\mathbf{r}_1, \mathbf{r}_2, t_f),$$ (3.14d)

$$p^{IP} = \int_I \int_P d^3 r_1 d^3 r_2 \; \rho(\mathbf{r}_1, \mathbf{r}_2, t_f),$$ (3.14e)

$$p^{PP} = \frac{1}{2} \int_P \int_P d^3 r_1 d^3 r_2 \; \rho(\mathbf{r}_1, \mathbf{r}_2, t_f).$$ (3.14f)

In the above expressions T, P are disjoint regions containing the target and projectile, $I = \mathbb{R}^3 \setminus (T \cup P)$, and t_f is some time chosen far enough after the collision for the two nuclear centres to become independent. As the functional $\rho[n]$ is unknown these exact expressions are of limited utility.

By introducing the correlation integrals

$$I_c^{V_1 V_2} = \int_{V_1} \int_{V_2} d^3 r_1 \, d^3 r_2 \, g_c(\mathbf{r}_1, \mathbf{r}_2, t_f) \, n(\mathbf{r}_1, t_f) \, n(\mathbf{r}_2, t_f),$$ (3.15)

with

$$g_c = \frac{\rho(\mathbf{r}_1, \mathbf{r}_2, t_f)}{n(\mathbf{r}_1, t_f) n(\mathbf{r}_2, t_f)} - \frac{1}{2}$$ (3.16)

and $V_1, V_2 \in \{T, P, I\}$, and the single-particle probabilities to find an electron on

the target

$$p_T = \frac{1}{2} \int_T \mathrm{d}^3 r \; n(\mathbf{r}, t_f) \tag{3.17}$$

or the projectile

$$p_P = \frac{1}{2} \int_P \mathrm{d}^3 r \; n(\mathbf{r}, t_f) \tag{3.18}$$

Eq. (3.14) become

$$p^{TT} = p_T^2 + \tfrac{1}{2} I_{\mathrm{c}}^{TT}, \tag{3.19a}$$

$$p^{TI} = 2 p_T (1 - p_T - p_P) - I_{\mathrm{c}}^{TP} - I_{\mathrm{c}}^{TT}, \tag{3.19b}$$

$$p^{II} = (1 - p_T - p_P)^2 + \tfrac{1}{2} I_{\mathrm{c}}^{PP} + I_{\mathrm{c}}^{TP} + \tfrac{1}{2} I_{\mathrm{c}}^{TT}, \tag{3.19c}$$

$$p^{TP} = 2 p_T p_P + I_{\mathrm{c}}^{TP}, \tag{3.19d}$$

$$p^{IP} = 2 p_p (1 - p_T - p_P) - I_{\mathrm{c}}^{PP} - I_{\mathrm{c}}^{TP}, \tag{3.19e}$$

$$p^{PP} = p_P{}^2 + \tfrac{1}{2} I_{\mathrm{c}}^{PP}. \tag{3.19f}$$

With an appropriate choice of t_f Eq. (3.17) reduces to a sum over the occupations of the bound states of the basis defined in Eq. (3.5). The single-centred BGM, as opposed to the two-centred BGM discussed in Sec. 4.1, basis contains no explicit projectile states, thus one must first project the one-particle solutions onto an appropriate set of projectile states (H or He bound states) in order to generate a sum over projectile occupations analogous to that described for the target. The process of projecting onto projectile states may lead to inaccuracies depending on how well the final state is represented by a finite number of BGM basis states.

The expressions for no, single, and double ionization in $\bar{p}$-He collisions presented in [19] may be recovered by closing the capture channels, i.e. setting $p_p = I_{\mathrm{c}}^{PP} = I_{\mathrm{c}}^{TP} = 0$. Being explicit we have

$$p^{TT} = p_T^2 + \tfrac{1}{2} I_{\mathrm{c}}^{TT}, \tag{3.20a}$$

$$p^{TI} = 2 p_T (1 - p_T) - I_{\mathrm{c}}^{TT}, \tag{3.20b}$$

$$p^{II} = (1 - p_T)^2 + \tfrac{1}{2} I_{\mathrm{c}}^{TT} \tag{3.20c}$$

As in [19] we may proceed in one of two ways[1]. The first and simplest method is to ignore correlation in the functionals for observables. This is equivalent to setting $I^{V_1 V_2} = 0$ for $V_1, V_2 \in \{T, P\}$ and leads to an independent electron model (IEM) description

$$p_{\text{IEM}}^{TT} = p_T^2, \tag{3.21a}$$

$$p_{\text{IEM}}^{TI} = 2p_T(1 - p_T - p_P), \tag{3.21b}$$

$$p_{\text{IEM}}^{II} = (1 - p_T - p_P)^2, \tag{3.21c}$$

$$p_{\text{IEM}}^{TP} = 2p_T p_P, \tag{3.21d}$$

$$p_{\text{IEM}}^{IP} = 2p_P(1 - p_T - p_P), \tag{3.21e}$$

$$p_{\text{IEM}}^{PP} = p_P^2. \tag{3.21f}$$

The second option is to explicitly deal with the correlation integrals by employing the adiabatic model of Wilken and Bauer [18] (WB). In this approach the one- and two-particle densities appearing in Eq. (3.16) are approximated by, the so-called, adiabatic densities, which are modelled by linear interpolations between the ground-state densities for the given centre, hydrogen or helium, with no, one, or two electrons bound. Labelling the various densities with a subscript denoting the number of bound electrons, for example the one-particle densities will be n_0, n_1, and n_2 respectively, we then have

$$n^A(t_f) = \begin{cases} N_V n_1 & N_V \in [0, 1] \\ [2 - N_V] n_1 + [N_V - 1] n_2 & N_V \in [1, 2] \end{cases} \tag{3.22}$$

and

$$\rho^A(t_f) = \begin{cases} 0 & N_V \in [0, 1] \\ [N_V - 1] \rho_2 & N_V \in [1, 2], \end{cases} \tag{3.23}$$

where

$$N_V(t_f) = N_V(t_f) = \int_V d^3 r \, n(\mathbf{r}, t_f) \tag{3.24}$$

---

[1]A third model, the frozen correlation model, was also discussed in [19, 71] but was shown to essentially reproduce IEM results.

for $V \in \{T,P\}$.

The quantity I_c^{TT} will then be handled, as it was in [71] and [19], by

$$
I_c^{TT} = -2p_T^2 +
\begin{cases}
0 & N_T \leq 1 \\
\iint\limits_T \dfrac{\rho^A(\mathbf{r_1},\mathbf{r_2},t_f)}{n^A(\mathbf{r_1},t_f)n^A(\mathbf{r_1},t_f)}n(\mathbf{r_1},t_f)n(\mathbf{r_1},t_f)\mathrm{d}^3r_1\mathrm{d}^3r_2 & N_T > 1.
\end{cases}
\tag{3.25}
$$

I_c^{PP} is treated analogously with constituent parts appropriately replaced by their projectile counterparts. I_c^{TP} must be handled with more care. As there is no clear generalization of the WB model to an explicit two-centre situation a different approximation scheme must be found. A fair starting place is to consider the constraints placed on the probabilities

$$
p^{TT} + p^{TI} + p^{II} + p^{TP} + p^{IP} + p^{PP} = 1
\tag{3.26}
$$

and

$$
0 \leq p^{V_1 V_2} \leq 1 \quad V_1, V_2 \in \{T,P,I\}.
\tag{3.27}
$$

The satisfaction of Eq. (3.26) is guaranteed by the form of Eq. (3.19) regardless of the models chosen for the correlation integrals.

By considering the probabilities to be functions of the correlation integrals and single-particle probabilities,

$$
p^{V_1 V_2} = p^{V_1 V_2}\left(p_T,p_P,I_c^{TT},I_c^{TP},I_c^{PP}\right),
\tag{3.28}
$$

the expressions given by Eq. (3.27) may be inverted to place a set of upper/lower bounds on values of I_c^{TP} that will produce probabilities between zero and one. If we let U_i and L_i, $i = 1,\ldots,4$, be the upper and lower bounds placed on I_c^{TP}, we obtain

$$
L_1 = 2p_t(1 - p_T - p_P) - I_c^{TT} - 1,
\tag{3.29a}
$$

$$
U_1 = 2p_T(1 - p_T - p_P) - I_c^{TT},
\tag{3.29b}
$$

$$
L_2 = -(1 - p_T - p_P)^2 - \tfrac{1}{2}I_c^{PP} - \tfrac{1}{2}I_c^{TT},
\tag{3.29c}
$$

$$
U_2 = 1 - (1 - p_T - p_P)^2 - \tfrac{1}{2}I_c^{PP} - \tfrac{1}{2}I_c^{TT},
\tag{3.29d}
$$

$$L_3 = -2p_T p_P, \tag{3.29e}$$

$$U_3 = 1 - 2p_T p_P, \tag{3.29f}$$

$$L_4 = 2p_P(1 - p_T - p_P) - I_c^{PP} - 1, \tag{3.29g}$$

$$U_4 = 2p_P(1 - p_T - p_P) - I_c^{PP}. \tag{3.29h}$$

We may then calculate a consistent value by setting

$$I_c^{TP} = \frac{1}{2}\left[\min_{1 \le i \le 4}\{U_i\} + \max_{1 \le i \le 4}\{L_i\}\right]. \tag{3.30}$$

It can be shown that as the single-particle ionization probability ($p_I = 1 - p_P - p_T$) approaches zero the upper and lower bounds converge. Additionally, in all cases the viable I_c^{TP} range is small. For p-He collisions the interval is at most approximately 0.1 and is at least one order of magnitude less than this through the majority of the impact energy and parameter space considered. For the He^{2+}-He system the largest interval is around 0.25. The gap remains on this order for a much larger range of the impact energies considered. As mentioned above the interval width approaches zero rapidly as the impact parameter increases. Thus there is little actual choice available for the value of I_c^{TP}, and not much is lost by always choosing the midpoint of this interval.

3.3 CALCULATION DETAILS

As has been discussed in previous works, for example [19, 77], fluctuations in the density persist after the collision process has completed if the Kohn-Sham potential is explicitly density dependent. Due to this fact the values of observables must be averaged over some range of t_f. The added complexity of the proton-helium collision system compared to that for antiproton-helium restricts the range through which the calculations may be run. As a result an insufficient range of t_f is available for averaging to produce a curve as smooth as in the $\bar{p}$-He system. More explicitly, letting $z_f = Vt_f$ be the final target-projectile separation for impact velocity V, $\bar{p}$-He collisions may be run to a final separation of 45 a.u., whereas p-He collisions run to a maximum inter-nuclear distance of
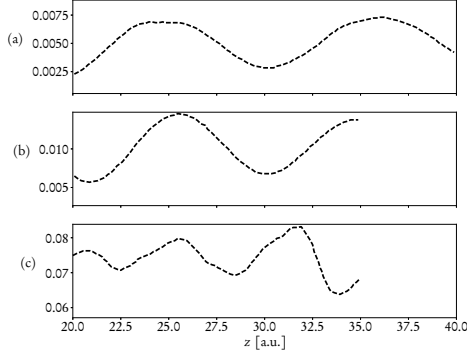
Figure 3.1: p^{II} as a function of z, an impact energy of 50 keV, and impact parameter of 1 a.u.: (a) $\bar{p}$-He, (b) p-He, (c) He^{2+}-He.
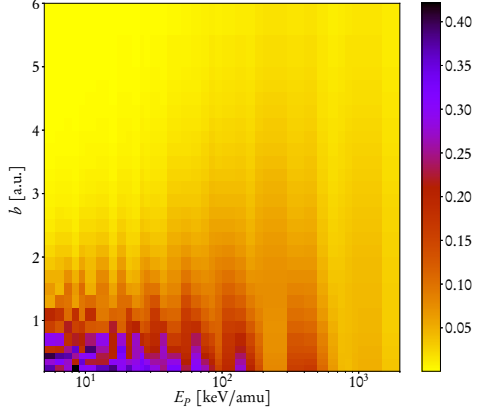

Figure 3.2: $\left|n_A(t_f) - n(t_f)\right|_1$ for the antiproton helium collision system.

around 35 a.u.

Figure 3.1, which depicts the values of p^{II} as a function of z for a prototypical choice of impact energy and parameter, makes these differences more apparent. Also of note is that the variances increase by about a factor of two between each of the collision systems.

We can get a sense of how well the adiabatic density approximates the true time-dependent density at t_f by considering their separation in function space. Owing to the fact that one-particle densities are necessarily L^1 functions (i.e. integrable functions) it is most natural to use the metric induced by the L^1-norm defined for any $f \in L^1(\mathbb{R})$ by

$$\left|f\right|_1 = \int \mathrm{d}^3 r \ \left|f(\mathbf{r})\right| \tag{3.31}$$

for measuring this distance.

Fig. 3.2 displays $\left|n(t_f) - n_A(t_f)\right|_1$, the difference between the adiabatic (n_A) and fully dynamic (n) densities at the final time t_f for the antiproton-helium system[2]. While it is possible to perform such an analysis for the p-He system as well, added complications brought on by having to deal with a two-centred

---

[2]All integrals were performed with the aid of the CUBA numerical integration package [78].

system make it much more difficult to produce and analyze such data. Intuitively one would expect that the difference between the two densities should follow the single-particle probability p_T. This belief is supported by the easily derived relation

$$\left|n(t_f) - n_A(t_f)\right|_1 \le 4p_T. \tag{3.32}$$

While Fig. 3.3 (which will be discussed in next section) demonstrates monotonic increase in p_T with increasing impact parameter, a general trend for all impact energies, Fig. 3.2 contains additional structures. Also of note is the minimum that appears along the impact-energy axis between 200 and 300 keV/amu. These unexpected features must be attributed to the fact that n_A contains only trivial angular dependence which makes a proper description of excitation and partial removal of electronic density impossible. This provides indications of the limitations of the WB model.

3.4 RESULTS

In the following subsections we present several plots of total cross sections for a variety of collision processes. Given an outcome probability p_{outcome} the total cross section associated with this probability is determined according to

$$\sigma_{\text{outcome}} = \int d^2b \, p_{\text{outcome}}(\mathbf{b}) = 2\pi \int_0^\infty db \, b \, p_{\text{outcome}}(b). \tag{3.33}$$

We will refer to our results using the acronyms IEM and WB corresponding to probabilities calculated using Eq. (3.21) and Eq. (3.19) using the WB model respectively. In both cases the dynamics include the frozen MCHF ground-state correlation potential.

The figures presented below were generated with several criteria in mind. First, a minimal number of older calculations was selected with the aim of covering as much of the impact energy range as possible while avoiding overburdening the figures with multiple overlapping curves. Second, works chosen must be the product of calculations that go beyond an IEM description of the collision process with preference given to fully correlated two-electron calculations. If
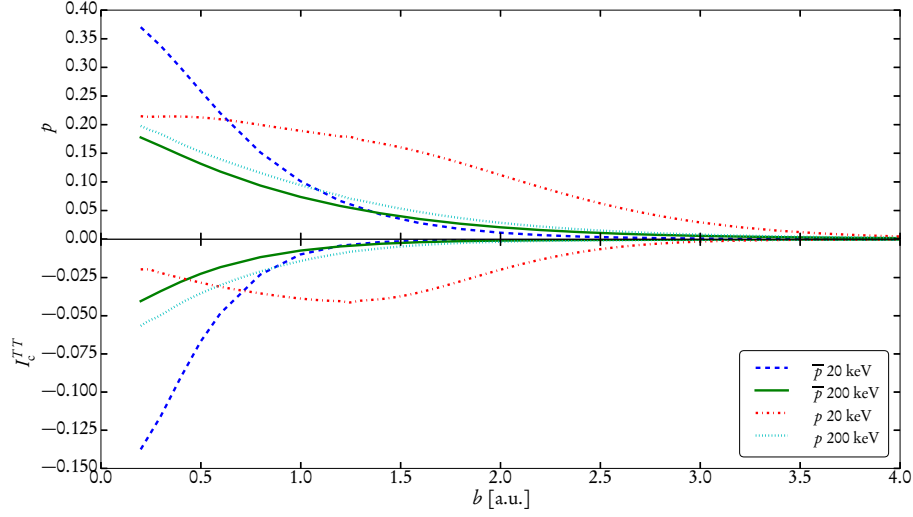
Figure 3.3: Single-particle removal probability, p, (upper pane) and correlation integral, I_c^{TT}, (lower pane) as functions of impact parameter for antiprotons and protons incident on helium atoms at 20 and 200 keV/amu.

one is interested in some of the calculations excluded from these comparisons there exist a plethora of independent-electron, independent-event, or related models [79–110], classical trajectory Monte Carlo calculations [111–120], and other classical statistical models such as the Bohr-Lindhard model [121, 122].

3.4.1 $\bar{p}$-He Vs. p-He Collisions

We begin the analysis of results with a comparison of proton and antiproton collisions with helium. To facilitate juxtaposition we will consider the zero-, one-, and two-electron removal processes in aggregate. The probabilities for these outcomes are given respectively by

$$p_0 = (1 - p)^2 + \tfrac{1}{2}I_c^{TT} = p^{TT}, \tag{3.34a}$$

$$p_+ = 2p(1 - p) - I_c^{TT} = p^{TI} + p^{TP}, \tag{3.34b}$$

$$p_{++} = p^2 + \tfrac{1}{2}I_c^{TT} = p^{II} + p^{IP} + p^{PP}, \tag{3.34c}$$
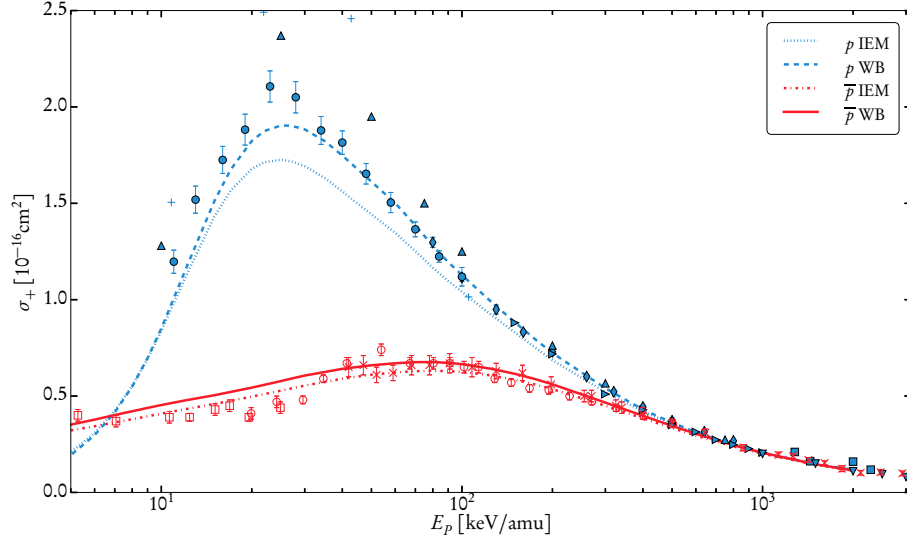
Figure 3.4: Total cross section for one-electron removal from helium by protons and antiprotons. Protons: dotted IEM and dashed WB (theory); ▲ [123], + [124], • [125], ◆ [126], ▶ [127], ▼ [128], and ■ [129] (experiment). Antiprotons: dashed-dotted IEM and solid WB (theory); □ [130], ◦ [131], and × [132] (experiment).

where the single-particle removal probability is given by

$$p = 1 - \tfrac{1}{2} \int_T \mathrm{d}^3 r \, n(\mathbf{r}, t_f) = 1 - p_T = p_P + p_I. \qquad (3.35)$$

For the $\bar{p}$-He system these are simply the probabilities presented in Eq. (3.20) making this choice of observables ideal for contrasting with the p-He system.

Presented in Fig. 3.3 are the single-particle removal probability and I_c^{TT} for both the proton and antiproton collision systems at 20 and 200 keV/amu as functions of the impact parameter. The correlation integral is always negative, decaying to zero in increasingly distant collisions as electron removal becomes less likely. This means that it provides a blanket enhancement to one-electron removal processes [cf. Eq. (3.34b)].

At 200 keV/amu the results for both p and I_c^{TT} become similar; at lower energies (i.e., 20 keV/amu) there are significant differences for proton and antiproton
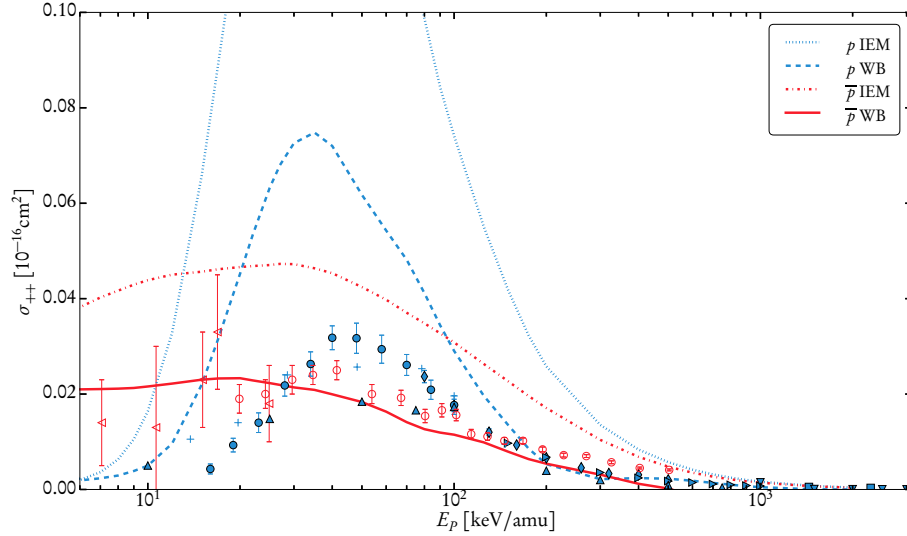
Figure 3.5: Total cross section for two-electron removal from helium atoms as a function of impact energy. Protons: dotted IEM and dashed WB (theory); ▲ [123], + [124], • [125], ♦ [126], ▶ [127], ▼ [128], and ■ [129] (experiment). Antiprotons: dashed-dotted IEM and solid WB (theory); ○ [131] and ◀ [133] (experiment).

collisions. In this range the single-removal probability for antiproton impact decays swiftly with rising impact parameter. On the other hand, the single-particle removal probability in low-energy proton-helium collisions remains appreciable over a much larger range. Such impact parameter profiles are a signature of electron capture which is the dominant electron removal process at lower impact energies. This behaviour is mirrored by that of I_c^{TT}.

A final feature of note is the spike in both antiproton curves at small impact parameter. In this region the antiproton passes through the charge density of the helium atom. Such close approaches result in destabilization of the electron binding and very efficient ionization [134].

Figures 3.4 and 3.5 present the total cross sections for one- and two-electron removal as functions of impact energy. These plots compare only the current proton-helium collision results to an updated version (denser impact energy grid and larger range of averaging as described in Sec. 3.3) of the antiproton-helium

28

results of [19] and to experimental data. For a comparison with other theoretical work see [71] (or [19]) and [135] ($\bar{p}$-He) and Sec. 3.4.2 (p-He).

For one-electron removal, Fig. 3.4, the WB model provides an increase for both protons and antiprotons over the IEM except at higher energies where the correlation integral tends to be small in magnitude as indicated by Fig. 3.3. In the case of proton-helium collisions this increase is an obvious improvement. The spread of the experimental data for antiproton-helium collisions makes it difficult to ascertain whether the enhancement in the cross section is preferable.

The two-electron removal cross sections, Fig. 3.5, for both proton and antiproton collisions are reduced significantly by the WB model. These reductions represent a clear improvement in either case. While the antiproton results are in fair agreement with experiment through the entire range explored the proton-helium results still differ notably below impact energies of 100 keV/amu. This is an indication that the WB model begins to display problems as capture becomes more important. These issues will be discussed in greater detail in the subsequent subsections.

3.4.2 p-He Collisions

Total cross sections for the various ionization and capture processes described by Eqs. (3.19) and (3.21) for both the WB model and the IEM are presented in Figs. 3.6–3.9. These results are compared to experiment as well as a selection of previous theoretical studies of p-He collisions that do account for electron correlation effects.

We will begin the discussion of these results by considering double capture. For our proton-helium collision calculations the single-particle capture probability, p_P, never rises above 1/2. From Eq. (3.25) it follows that $I_c^{PP} = -2p_P{}^2$, which implies that $p_{PP} \equiv 0$. Due to the triviality of this result no plot is displayed. The IEM so amplifies the double capture cross section that the WB model can be considered in better agreement with experiment even though it is zero for all impact energies and perceived as an improvement over IEM.

Similar to double capture, single capture, Fig. 3.6, only depends on one correlation integral. The IEM provides fair agreement with the experimental data
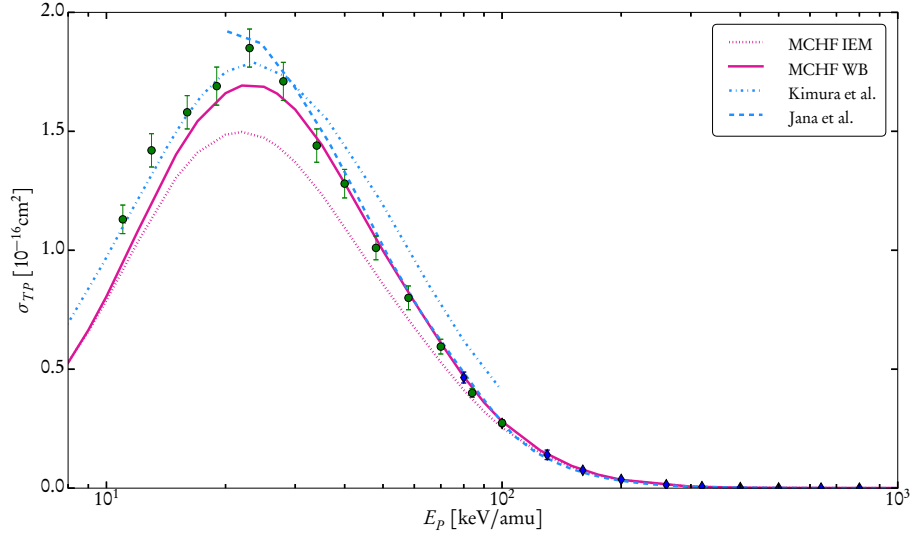
Figure 3.6: Total cross section for single capture in proton-helium collisions. Theoretical results: AO-MO model of Kimura et al. [136] and DW-4B (post form) of Jana et al. [137]. Experimental Data: • [125] and ◆ [126].

except that it underestimates the peak. This problem is corrected by the WB model which is in good agreement with experiment through most of the impact energy range considered. This fact helps to justify the model used for I_c^{TP} in Eq. (3.30) as single capture is expressed as the IEM result plus a correction coming solely from I_c^{TP} [cf. Eq. (3.19d)]. Also presented in Fig. 3.6 are the atomic orbital (AO) molecular orbital (MO) matching results of Kimura et al. [136] (AO-MO) and the post form, which includes explicit dynamic correlation contributions, of the four-body distorted-wave (DW-4B) results of Jana et al. [137]. It should be noted that what Jana et al. call dynamic correlation while not identical to TDDFT dynamic correlation (a time-dependent correlation potential v_c) is the analogue in two-electron calculations and ultimately both should describe the same effects. The DW-4B and WB models agree quite well above impact energies of 40 keV/amu. Below this they begin to deviate, with the DW-4B results remaining in better agreement with experiment (excluding the lower extremes of the data where the perturbative nature of the DW-4B model likely causes it to become less reliable). The opening of a gap between these two calculations coincides precisely
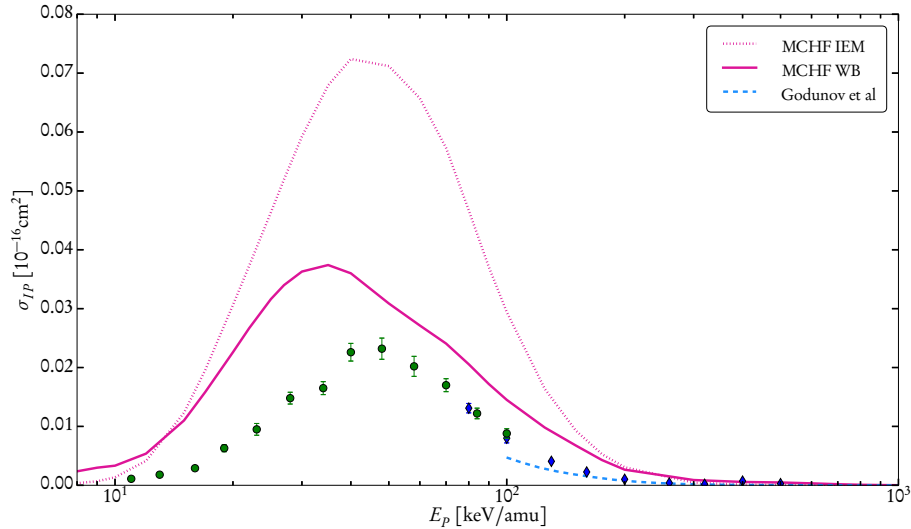
Figure 3.7: Total cross section for transfer ionization in proton-helium collisions. Theoretical results: Second order Born approximation of Godunov et al. [138]. Experimental data: ● [125] and ◆ [126].

with the increased role of dynamic correlation as impact energies decrease. This trend continues with the results of Kimura et al. throughout the remainder of the impact energy range. The discrepancy between the AO-MO results and the other calculations for energies above the peak is likely due to the dominance of the MO over the AO in the analysis [136]. The result of this appears to be an overestimate of the coupling between centres leading to a slight overestimate of the cross section at high energies.

Figure 3.7 presents the results for transfer ionization. Once again the WB model offers an improvement over IEM descriptions, lowering the cross section by as much as a factor of two. Even with this correction the WB still overestimates the data through the entire range. An unfortunate side effect of the model is a slight shift in the peak of the curve towards lower energies. The overestimation in this channel may be a result of the redistribution of probability which must occur with the double capture channel effectively closed by the WB model.

Our IEM and WB results are compared to the second-order Born approximation calculation of Godunov et al. [138] (on- and off-shell contributions included).
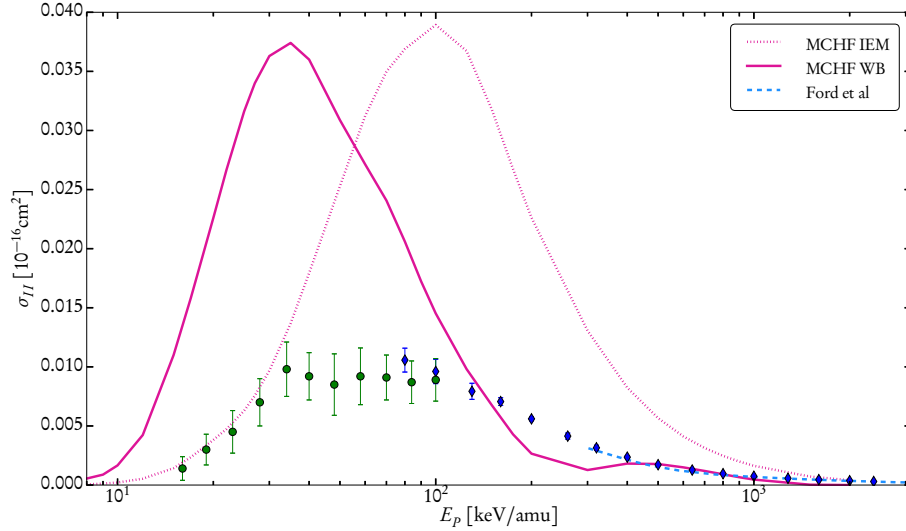
Figure 3.8: Total cross section for double ionization of helium by proton impact. Theoretical results: FIM of Ford et al. [139]. Experimental data: ● [125] and ◆ [126].

Few correlated transfer ionization calculations exist. As a result conclusions for the quality of correlation below 100 keV/amu are difficult. One additional calculation was performed by Belkić and Mančev [143]. However, their data cover less of the desired impact energy range and were thus excluded from Fig. 3.7. Godunov et al. are consistently below both IEM and WB. The fact that the IEM falls slightly below the WB results above 200 keV/amu points to a problem with the WB calculations. In this range the difficulty of separating target and projectile will naturally be emphasized as the relative errors due to the projection problem grow [see discussion following Eq. (3.19)]. It would seem that these issues are compounded when the density is forced through the additional machinery of the WB model. In this region it then becomes difficult to determine to what extent discrepancies are due to dynamic vs. functional correlation effects or issues of accuracy.

Next we turn our attention to the results for double ionization in Fig. 3.8. The WB model improves results by reducing those of the IEM at high energies. Agreement is lost as impact energy drops below 100 keV/amu. A close inspection
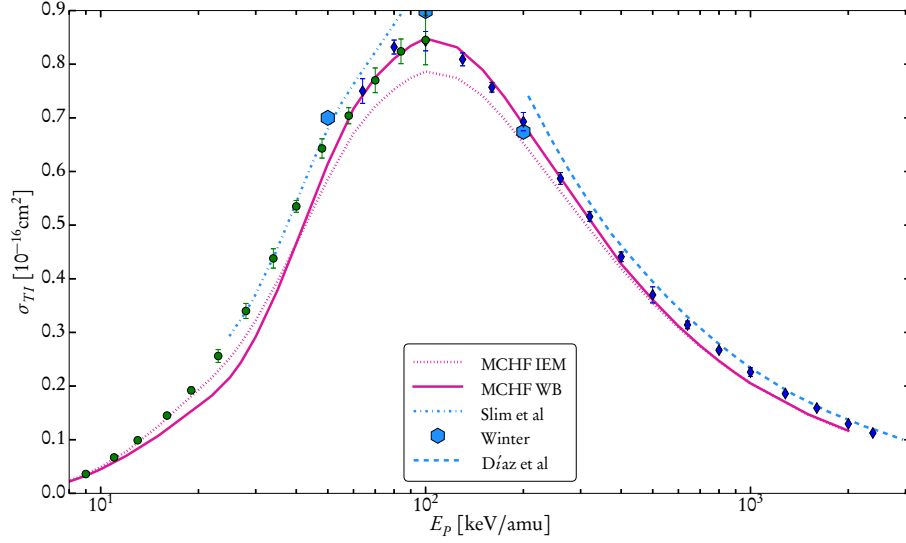
Figure 3.9: Total cross section for single ionization of helium by proton impact. Theoretical results: Slim et al. [140], Winter [141], and Díaz et al. [142] Experimental data: ● [125] and ◆ [126].

of the double ionization result reveals that they are identical to those for transfer ionization in the approximate range 10–300 keV/amu.

To understand what is causing this we must examine some of the ramifications of Eq. (3.30). It can be shown that whenever I_c^{TP} is sandwiched between either L_2 and U_4 or L_4 and U_2 we have $p^{II} = p^{IP}$. As the former is true for the majority of contributing impact parameters for the energy range mentioned above we fall in a situation where double ionization and transfer ionization are forced to be equal.

Another undesirable feature of the double ionization cross section is the dip below the experimental data between 100 and 400 keV/amu. As has been discussed in Sec. 3.3 the added complexity of the proton-helium collision system compared to that for antiproton-helium restricts the range through which the calculations may be run. Due to this fact an insufficient range of t_f is available for averaging to produce a curve as smooth as in the $\bar{p}$-He system (see Fig. 3.1 and Fig. 3.5), resulting in the additional structure in this region.

Above 300 keV/amu the wb model behaves in a manner consistent with that

seen in $\bar{p}$-He collisions, lowering IEM results into fair agreement with the data, then causing a drop below experiment as impact energy increases.

As with transfer ionization few correlated calculations exist for double ionization in p-He collisions. Displayed in Fig. 3.8 are the forced impulse method (FIM) results of Ford et al. [139]. The FIM and WB models agree well between 400 and 1000 keV/amu. Below this range the issue of final state stability causes a sizable disagreement between the two. Above this range issues with how the WB model distributes probabilities between channels force the double ionization cross section to become smaller than is physical far too quickly.

Finally we consider our single ionization results depicted in Fig. 3.9. The WB model corrects the discrepancy between the peaks of the IEM and experimental data. Both calculations are in good agreement with experiment, and each other, except where the WB results dip slightly below the expected values due to a loss of probability to the overestimated double ionization maximum around 35 keV/amu.

For this channel enough previous calculations exist to cover almost all of our impact energy range. These include the coupled-channel calculations of Slim et al. [140] and Winter [141] as well as the convergent frozen-correlation approximation (CFCA) of Díaz et al. [142]. Slim et al. obtain better agreement with experiment in the range 25–50 keV/amu. This is likely due to the overestimation of transfer and double ionization discussed earlier. Above this range the WB model performs better, this is likely due to what Slim et al. describe as the effects of an incomplete continuum description in their calculation [140].

In the energy range covered by Winter the WB model appears to be in almost exact agreement with experiment. Winter attributes much of his disagreement to his calculations' not fully accounting for channels beyond single capture and ionization [141].

The results of Díaz et al. provide a similar level of agreement as the WB model. Both models are essentially equidistant from experiment above 300 keV/amu. Díaz et al. attribute their overestimation of the cross section to a neglect of the capture channels [142], similarly the WB model falls below the experiment likely due to the overestimate of transfer ionization in this impact energy region.

Figure 3.10: Total cross section for single ionization of helium by He^{2+} impact. Theoretical results: Gramlich et al. [144], Barna et al. [145], and Pindzola et al. [146]. Experimental data: ♦ [126], ● [125], ▼ [147], and ▲ [129].

3.4.3 He^{2+}-He Collisions

The results of the He^{2+}-He calculations for both IEM and WB model and experimental data are presented in Figs. 3.10–3.14 along with an assortment of previous, correlated theoretical calculations. As with our proton-helium results single ionization (Fig. 3.9) in both the IEM and WB model are quite similar excluding an energy range around the maximum where the WB model increases the cross section significantly. In both cases the peak appears to be shifted to a slightly lower impact energy compared to the measurements. Similar behaviour below 100 keV/amu see the pair falling above experiment. Depicted alongside the current results in Fig. 3.10 are the previous coupled-channel calculations of Gramlich et al. [144], Barna et al. [145], and Pindzola et al. [146]. At the high end of the energy range explored all results are in agreement. At lower energies (approximately 15–80 keV/amu) the results of Gramlich et al. are in much better agreement with experiment. This region is precisely the range where capture is dominant and quite strong. As a result $p_T < 1/2$ for a significant portion of this range causing
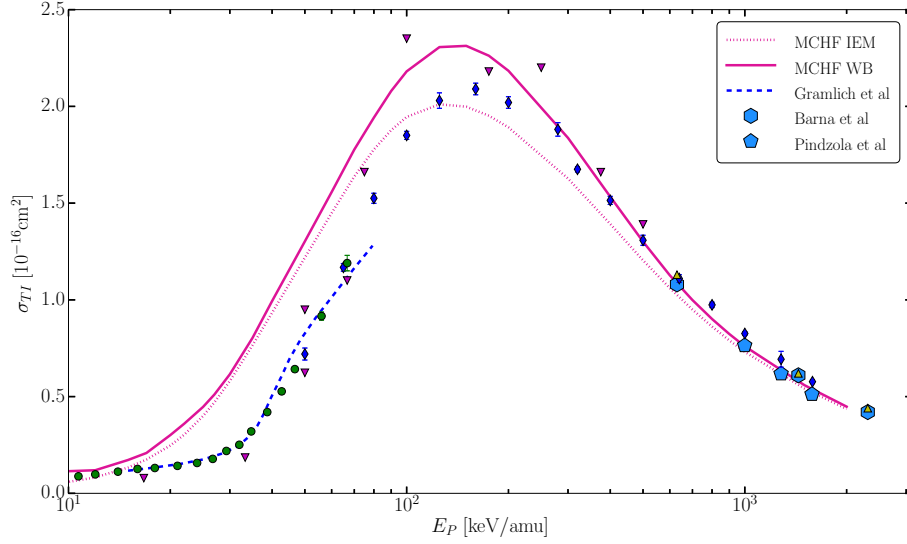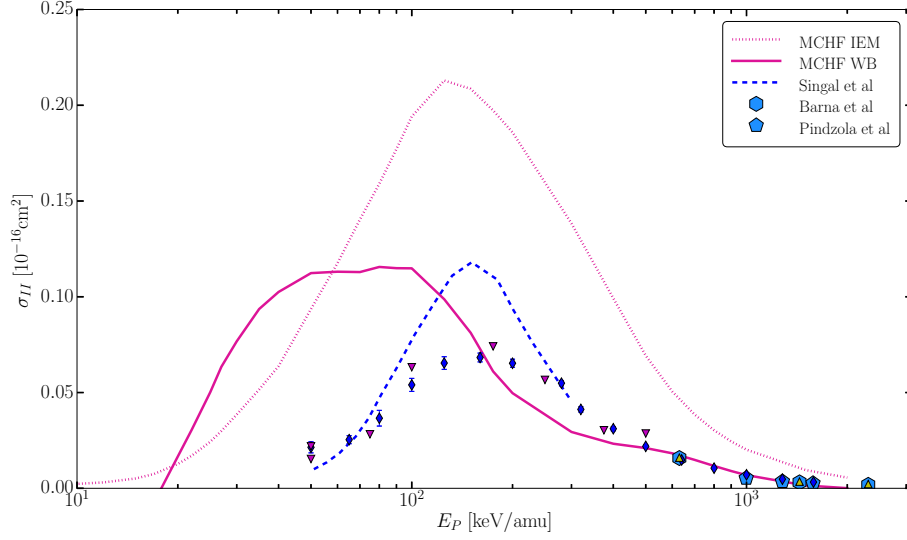
Figure 3.11: Total cross section for double ionization of helium by He^{2+} impact. Theoretical results: Singal et al. [91], Barna et al. [145], and Pindzola et al. [146] Experimental data: ◆ [126], ▼ [147], and ▲ [129].

$I_c^{TT} = -p_T{}^2$. A negative I_c^{TT} will increase p^{TI}, luckily I_c^{TP} is enough to keep the WB results from exceeding those of the IEM [cf. Eq. (3.19b)]. The lack of correlated calculations near the experimental maximum unfortunately means little can be concluded in this region of the curve.

The WB results for double ionization, Fig. 3.11, display the familiar pattern seen in both antiproton and proton collisions, namely, fair agreement with experiment at high impact energies coupled with overestimation of the data at lower energies and a reduction over IEM. It should be noted that due to the size of the error bars of the low energy $\bar{p}$-He data what constitutes an overestimation is difficult to determine (WB results do tend towards the upper limits of these error bars). It would seem that such behaviour is a general feature of the WB model. For the positively-charged projectiles the WB model causes a shift in the maximum to lower energies. Much like the p-He results there are slight fluctuations in the He^{2+}-He WB results due to instabilities in the dynamics.

As above the two-electron calculations by Barna et al. and Pindzola et al. support the high-energy WB results. Fig. 3.11 also includes the results of Singal et
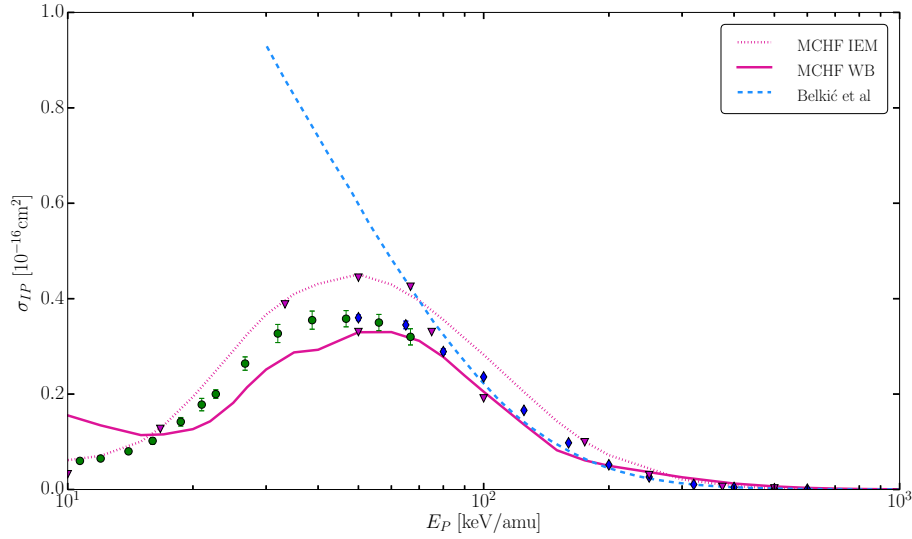
Figure 3.12: Total cross section for transfer ionization in He^{2+}-He Collisions. Theoretical results: Belkić et al. [148]. Experimental data: ♦ [126], • [125], and ▼ [147].

al.: while not a two-electron calculation it incorporates a modified single-particle potential designed to account for the increased difficulty of ionizing two electrons. These results confirm the location of the IEM cross section maximum. This confirms the belief that the WB model becomes less dependable at lower energies.

Unlike for the proton-helium system double ionization and transfer ionization, Fig. 3.12, are not identical. The increased role of capture due to the deeper potential well of the He^{2+} projectile has the important consequence of allowing the probability p_P to rise above the critical one half threshold. As a result I_c^{PP} is no longer trivial, and the bounds defining I_c^{TP} vary more freely. The WB model reduces IEM results through most of the impact energy range. A slight over-reduction occurs to the left of the peak. Below 20 keV/amu the results begin to swing drastically upwards to compensate for the fact that double ionization becomes zero in this region. As mentioned above the ripples present in the WB curve are due to instabilities in the dynamics.

Much like the p-He system few calculations exist beyond the level of the IEM for the transfer ionization channel. Presented is the post form of the four-body

Figure 3.13: Total cross section for single capture in He^{2+}-He collisions. Theoretical results: Fritsch [149] and DW-4B of Jana et al. [137]. Experimental data: ◆ [126], ● [125], ▼ [147], and ■ [150].

continuum distorted-wave approximation results of Belkić et al. [148]. The post form includes explicit dynamic correlation. At the extremes of the energy range Belkić et al. are in better agreement with experiment, as the WB and IEM slightly exaggerate the cross section (similar to the p-He results). These discrepancies become larger as the peak is approached from above. It is difficult to ascertain how much of this widening gap between our WB results and Belkić et al.'s calculation is a result of the increased importance of dynamic correlation. Certainly this is the primary difference down to 80 keV/amu, below which point the perturbative calculation appears to break down making it less useful for the current purpose.

Single capture cross sections, presented in Fig. 3.13, also follow a pattern similar to that laid out by the proton-helium case: an increase in the WB over IEM results. This increase results in good agreement with experiment above 50 keV/amu. Unlike previous results the enhancement in cross section persists to low energies, where the WB model overestimates the measured values.

In the high-energy region of the curve the WB model is in fair agreement with the DW-4B results of Jana et al. It would appear the effects of dynamic correlation
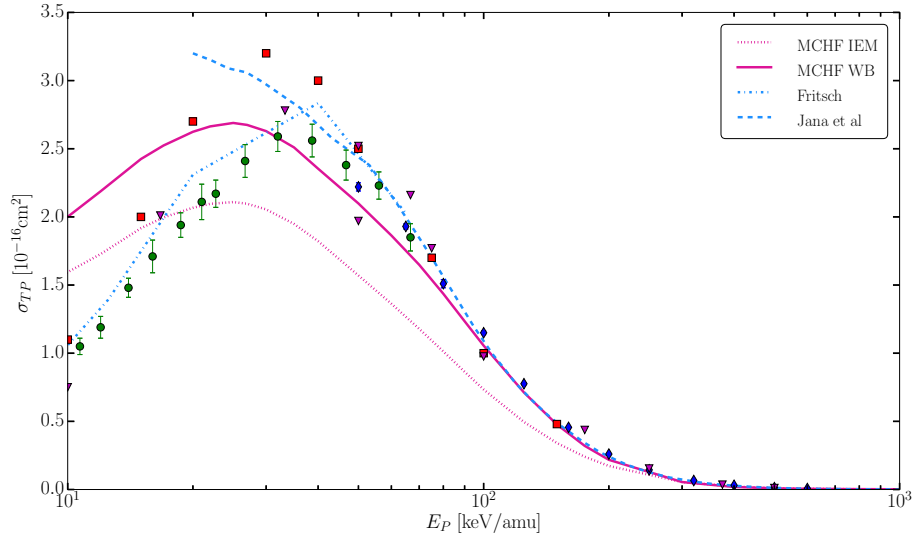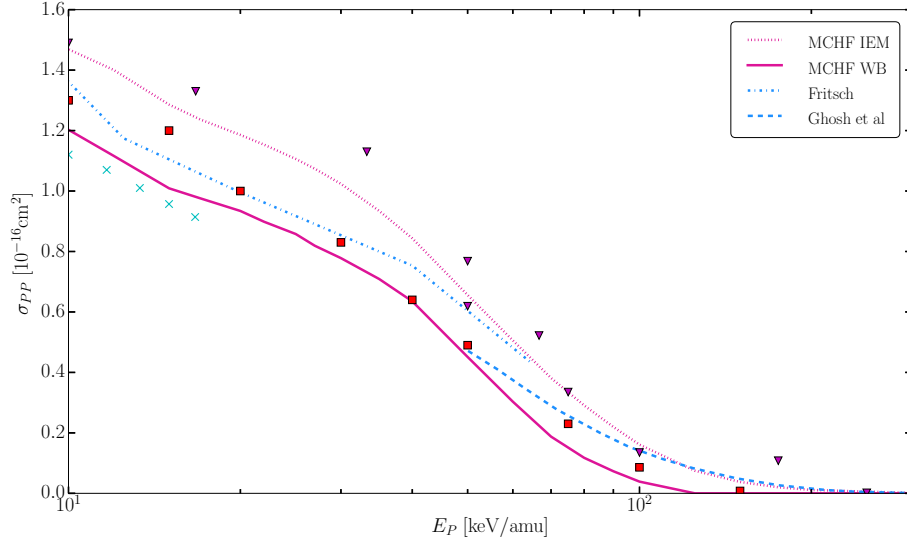
Figure 3.14: Total cross section for double capture in He^{2+}-He collisions. Theoretical results: Fritsch [149] and Ghosh et al. [151]. Experimental data: ▼ [147], ■ [150], and × [152].

may account for the slight underestimation of the WB model to the right of the maximum. Below the peak the coupled-channel results of Fritsch [149] lend credence to the experimental data. The failure of both the WB and IEM models to agree with these results (and by extension experiment) may point to a possible failure of the underlying dynamic calculation in separating the target, projectile and ionizing regions (T, P and I).

As mentioned above the expanded role of capture causes the correlation integral I_c^{PP} to no longer be trivial. This also means that double capture in the WB model is no longer identically zero. Results for double capture are presented in Fig. 3.14. While the WB decreases the cross section below IEM it is difficult to conclude whether this is an improvement due to the relatively wide spread in the experimental data.

To aid in this determination we compare our results to those of Fritsch [149] and the post form of the four-body boundary corrected continuum intermediate state approximation (BCCIS-4B) results of Ghosh et al. [151]. For the highest energies presented Ghosh et al. support the results of the IEM over those of

the WB model. In this region the same factors that force the p-He WB double capture channel to be identically zero force cross sections above 125 keV/amu into triviality. Below this limit the data of Ghosh et al. begin to fall more in line with the WB results. As the results of Fritsch enter the picture in the lower portion of the energy range the WB model appears to be favoured, the gap between Fritsch and the WB being less than that between IEM and Fritsch. The remaining discrepancy may be due once again to dynamic correlation effects.

CHAPTER 4

HE$^+$-HE COLLISIONS

The investigations of the previous chapter began with the simplest possible multi-electron collision system, one where a negatively-charged projectile is incident on helium. The situation was then complicated by allowing the projectile to be positive, thus forcing one to consider electron transfer in addition to ionization processes.

In this chapter the system of interest is expanded further by the inclusion of an active electron on the projectile. More specifically, the remainder of this work concerns itself with the He$^+$-He collision system.

While the external potential, v_{ext}, maintains the form of Eq. (3.3), the spin-polarized nature of the collision system suggests that the spin-free description utilized in the previous chapter should be replaced by the full spin-dependent TDKS presented in Eq. (2.10).

The determination of a spin-dependent exchange-correlation potential forms the bulk of this chapter (Sec. 4.1) in which a procedure for calculating an accurate exchange potential within the x-only approximation is discussed. This is followed by a brief discussion of the method used to extract cross sections from the one-particle density (Sec. 4.2) before presenting results in Sec. 4.3. This chapter can be seen as an extended version of the work presented in [153].

4.1 Calculating the x-Potential

While the correlation potential in Eq. (2.10) may be ignored, that is the x-only approximation may be used (with some understanding of the consequences), an accurate exchange potential is essential for a precise description of the He^+-He collision system. The spin-polarized nature of the system, which emphasizes exchange effects, makes this fact indisputable. To this end the KLI approximation to the OPM (see Sec. 2.4.2) was employed in the calculation of v_x^σ.

The ground-state density functional theory scheme of [154][1] has been adapted to calculate a time-dependent exchange potential. At any instant of time, t, the He^+-He system may be regarded as a diatomic quasi-molecule with an internuclear distance $R(t) = \sqrt{b^2 + Z(t)^2}$, where b and Z are the impact parameter and the z position of the projectile as described below Eq. (3.3). If at each time-step of the propagation the time-dependent Kohn-Sham orbitals, $\varphi_{j\sigma}(\mathbf{r}, t)$ are fed into the KLI functional (ignoring self consistency) an exchange potential, $v_x^\sigma[\{\varphi_{j\sigma'}\}; t]$, is obtained[2]. In Ref. [154] the KLI scheme has been implemented for eigenstates of a total KS potential which is invariant against rotation around the internuclear axis. This restriction complicates the use of the corresponding KLI potential, since the present $\varphi_{j\sigma}$ do not exhibit any specific symmetry.

In order to detail a solution to the symmetry problem a more thorough description of the TC-BGM [155] is necessary. Within the TC-BGM the Kohn-Sham (KS) orbitals are represented in a non-orthogonal basis

$$\varphi_{j\sigma}(\mathbf{r}, t) = \sum_{c \in \{P,T\}} \sum_{k,L,M} d_{ckL}^{\sigma j}(t) \tilde{\chi}_{ck}^{LM}(\mathbf{r}, t), \tag{4.1}$$

where

$$\tilde{\chi}_{ck}^{LM}(\mathbf{r}, t) = \begin{cases} e^{i\mathbf{v}_T \cdot \mathbf{r}} \chi_{ck}^{LM}(\mathbf{r}, t) & c = T, \\ e^{i\mathbf{v}_P \cdot \mathbf{r}} \chi_{ck}^{LM}(\mathbf{r}, t) & c = P, \end{cases} \tag{4.2}$$

which are the basis functions with electron translation factors (ETF) included.

---

[1] The details of this implementation may be found in [154]. The code was provided by the authors via private communication.

[2] The normalization of the KLI potential is chosen so that $v_x^{KLI}(\mathbf{r}, t) \xrightarrow{|\mathbf{r}| \to \infty} 0$.

Table 4.1: Description of the TC-BGM basis expansion.

state	1s	2s	2p	3s	3p	3d	4s	4p	4d	4f
k	1	2	3, 4	5	6, 7	8-10	11	12, 13	14-16	17-20
$L_{\max}$	0	0	1	1	2	2	2	3	3	3

The basis functions themselves are given by [similarly to the one-centre basis of Eq. (3.5)]

$$\chi_{ck}^{LM}(\mathbf{r}, t) = W_P(\mathbf{r}, t, \epsilon_P)^L W_T(\mathbf{r}_T, \epsilon_T)^M \chi_{ck}^{00}(\mathbf{r}), \tag{4.3}$$

with

$$W_T(\mathbf{r}_T, \epsilon_T) = \frac{1 - e^{-\epsilon_T r_T}}{r_T}, \tag{4.4}$$

and

$$W_P(\mathbf{r}, t, \epsilon_P) = \frac{1 - e^{-\epsilon_P |\mathbf{r} - \mathbf{R}(t)|}}{|\mathbf{r}_T - \mathbf{R}(t)|}, \tag{4.5}$$

where $\mathbf{r}_T$ represents the position vector with respect to the target centre and we are working in the centre-of-mass frame where $\mathbf{R} = \mathbf{r}_T - \mathbf{r}_P$.

In Eq. (4.3) the functions χ_{ck}^{00} are the bound orbitals for the target helium atom ($c = T$) and the projectile helium ion ($c = P$). Just like in the one-centred case discussed in Sec. 3.1 the basis is simplified by including only states generated from the projectile potential. The regularizer is once again set to $\epsilon_P = 1$. The complete basis set used may be described in terms of the maximum L value included for each bound sub-shell, 1s-4f, indexed by k, in the basis. These values are listed in Tab. 4.1 and total 124 basis states.

It is clear from the above description that only the basis states corresponding to s-type orbitals will make cylindrically symmetric contributions to the KS-orbitals. The simplest solution is to only feed the 1s contributions into the KLI functional. While higher s-states are also admissible they will no longer represent the most occupied subshell meaning their inclusion will do little to improve the accuracy of the description of a given orbital. Leaving out ETFs for the time being the orbitals will take the explicit form

$$\varphi_{j\sigma}^{1s}(\mathbf{r}, t) = a_T^{\sigma j}(t) \chi_{T1}^{00}(\mathbf{r}, t) + a_P^{\sigma j}(t) \chi_{P1}^{00}(\mathbf{r}, t). \tag{4.6}$$

43

The coefficients, $a_c^{\sigma j}$, are the result of projecting the KS-orbitals onto the two-dimensional subspace spanned by the target and projectile 1s-states

$$|\varphi_{j\sigma}^{1s}\rangle = \hat{P}|\varphi_{j\sigma}\rangle = \sum_{c_1,c_2 \in \{T,P\}} \tilde{S}_{c_1 c_2}^{-1} |\chi_{c_1 1}^{00}\rangle \langle \chi_{c_2 1}^{00}|\varphi_{j\sigma}\rangle \tag{4.7}$$

with $\tilde{S}_{c_1 c_2}^{-1}$ the inverse of the overlap matrix

$$\tilde{S}_{c_1 c_2} = \langle \chi_{c_1 1}^{00}|\chi_{c_2 1}^{00}\rangle . \tag{4.8}$$

The coefficients are then determined to be

$$a_c^{\sigma j} = \sum_{c_1,c_2 \in \{T,P\}} \sum_{k=1}^{K} \sum_{l=0}^{L} \tilde{S}_{cc_1}^{-1} S_{c\,1\,0}^{c_2\,k\,l} d_{c_2 kl}^{\sigma j}, \tag{4.9}$$

with

$$S_{c_1 k_1 l_1}^{c_2 k_2 l_2} = \langle \chi_{c_1 k_1}^{l_1 0}|\chi_{c_2 k_2}^{l_2 0}\rangle \tag{4.10}$$

the full overlap matrix.

Returning to the question of the ETFs, working in the rotating centre-of-mass frame in which the z-direction points along the internuclear axis the ETFs become

$$e^{i\mathbf{v}_T \cdot \mathbf{r}} = e^{\frac{iV}{2}(x \sin\theta - z \cos\theta)}, \tag{4.11a}$$

$$e^{i\mathbf{v}_P \cdot \mathbf{r}} = e^{\frac{iV}{2}(z \cos\theta - x \sin\theta)}, \tag{4.11b}$$

where $\theta = \arctan b/Z$ and V is the relative velocity of the centers, the same velocity appearing below Eq. (3.3). If we now introduce a two-centred coordinate system, placing the foci at the two nuclear centres it becomes clear that the portion of the ETFs containing x violates the desired cylindrical symmetry (see Sec. A.2).

Two obvious solutions present themselves. First, one may simply ignore the ETFs completely. This would amount to passing the orbitals described by Eq. (4.6) into the KLI functional. Alternatively the symmetry breaking portions of the ETFs

may be dropped. In this case the full 1s-only KS-orbital becomes

$$\tilde{\varphi}^{1s}_{\sigma j}(\mathbf{r}, t) = a^{\sigma j}_T(t) e^{-\frac{iVz\cos\theta}{2}} \chi^0_{T1}(\mathbf{r}, t) + a^{\sigma j}_P(t) e^{\frac{iVz\cos\theta}{2}} \chi^0_{P1}(\mathbf{r}, t). \qquad (4.12)$$

This will offer at least some of the correction provided by the full ETF. Unfortunately, as the internuclear coordinate $Z(t)$ approaches zero (corresponding to $\theta = \frac{\pi}{2}$) the partial ETF will tend to one, meaning that when the target and projectile are at their closest, i.e. in the most active region of the collision, no ETF will be present.

Any investigation of the impact of the ETFs is best carried out in an isolated environment. To achieve this we may introduce a no-response model. In such a model the initial occupations of the orbitals passed to the KLI functional will be frozen and the full orbitals will be propagated in the resulting potential. To be more concrete, if we have two spin-up and one spin-down electron the coefficients be given the fixed values

$$\tilde{a}^{\uparrow 1}_T = \tilde{a}^{\uparrow 2}_P = \tilde{a}^{\downarrow 1}_T = 1 \quad \text{and} \quad \tilde{a}^{\uparrow 1}_P = \tilde{a}^{\uparrow 2}_T = \tilde{a}^{\downarrow 1}_P = 0. \qquad (4.13)$$

In this way the only phase information entering the exchange functional will arise directly from the ETFs. The calculation in which the coefficients are obtained from Eq. (4.9) will be referred to as the response model in the following.

Regardless of which option is chosen it is important that v_H be determined with the same set of orbitals used in the calculation of v^σ_x, preserving the precise cancellation of the self interaction present in the Hartree potential. A description of some of the technical details of the process of propagating the KS-orbitals in these time-dependent potentials are provided in Appendix B. A collection of visualizations of this process may be found in Sec. 4.3.3 along with several figures which illustrate the time evolution of the collision system.

4.2   FINAL-STATE ANALYSIS

Of interest in any scattering problem is the probability of finding the system in some final state. If we represent the state being considered as $|f_1 f_2 f_3\rangle$ and the

initial state of the system propagated to some final time t_f by $|\varphi_{1\uparrow}\,\varphi_{2\uparrow}\,\varphi_{1\downarrow}(t_f)\rangle$ the exclusive probability to find the system in the given final state at time t_f will be given by

$$P_{f_1f_2f_3}(t_f) = \left|\langle f_1\,f_2\,f_3|\varphi_{1\uparrow}\,\varphi_{2\uparrow}\,\varphi_{1\downarrow}(t_f)\rangle\right|^2. \tag{4.14}$$

If one assumes that both the propagated and final states can be represented as single Slater determinants then the probability in question becomes

$$P_{f_1f_2f_3}(t_f) = \det\left[\gamma_{ff'}(t_f)\right], \tag{4.15}$$

where $\gamma_{ff'}$ is the one-particle density matrix

$$\gamma_{ff'}(t_f) = \sum_{\sigma}\sum_{j=1}^{N_\sigma} \langle f|\varphi_{j\sigma}(t_f)\rangle\,\langle\varphi_{j\sigma}(t_f)|f'\rangle, \tag{4.16}$$

with f and $f' \in \{f_1, f_2, f_3\}$, and the transition amplitudes

$$\langle f|\varphi_{j\sigma}(t_f)\rangle = \langle\tilde{\chi}_{ck}^{l0}|\varphi_{j\sigma}(t_f)\rangle \tag{4.17}$$

are readily calculable from the dynamics (for some k, l, c, and properly orthogonalized basis functions $\tilde{\chi}_{ck}^{l0}$).

Expressions similiar to Eq. (3.21) may be constructed in this context. The key to the derivation comes from expressing the single-particle probabilities in terms of the transition amplitudes, for example, p_T may be written

$$p_T = \frac{1}{3}\sum_{\sigma}\sum_{j=1}^{N_\sigma}\sum_{k=1}^{K} \left|\langle\tilde{\chi}_{Tk}^{00}|\varphi_{j\sigma}(t_f)\rangle\right|^2, \tag{4.18}$$

with p_P and p_I expressed similarly.

Alternatively, one could consider the probability to explicitly measure the states of some subset of the total number of particles. These so called inclusive probabilities can be expressed in terms of determinants of submatrices of the density matrix [156].

In the current problem we are interested in those probabilities which correspond to the possible outcome channels of in the He$^+$-He collision system. The

processes can be broadly categorized into those that involve one active electron:

$$\text{He}^+ + \text{He} \rightarrow \text{He}^+ + \text{He}^+ + e^- \tag{4.19}$$

$$\text{He}^+ + \text{He} \rightarrow \text{He} + \text{He}^+ \tag{4.20}$$

$$\text{He}^+ + \text{He} \rightarrow \text{He}^{2+} + \text{He} + e^-, \tag{4.21}$$

two active electrons:

$$\text{He}^+ + \text{He} \rightarrow \text{He}^+ + \text{He}^{2+} + 2e^- \tag{4.22}$$

$$\text{He}^+ + \text{He} \rightarrow \text{He}^{2+} + \text{He}^+ + 2e^- \tag{4.23}$$

$$\text{He}^+ + \text{He} \rightarrow \text{He} + \text{He}^{2+} + e^-, \tag{4.24}$$
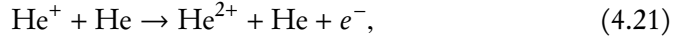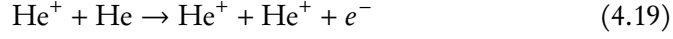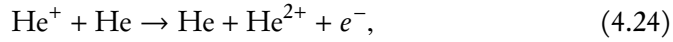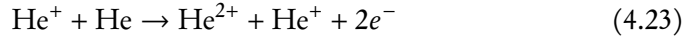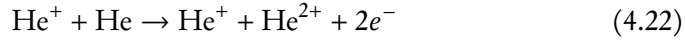
and three active electrons:

$$\text{He}^+ + \text{He} \rightarrow \text{He}^{2+} + \text{He}^{2+} + 3e^-. \tag{4.25}$$
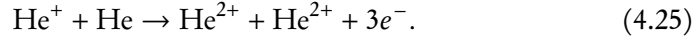
Additionally there is the channel where no charges are transferred and the two channels that result in the production of He⁻. Cross sections for the latter are known to be negligible [157, 158].

In such configurations we find k particles on the projectile, l particles in the continuum, and $3 - k - l$ on the target ($0 \leq k \leq 3$ and $0 \leq l \leq 3 - k$). The probabilities p_{kl} may be calculated in terms of sums of inclusive probabilities to find a given number of particles in the bound states of the target and projectile by applying the machinery of [156] (see for example [159–161]). In order to avoid the use of continuum states the probabilities of interest are determined indirectly through the probabilties p'_{jk} of finding j electron on the target and k electron on the projectile. These take the form

$$P''_{jk} = \sum_{\substack{f_1 < ... < f_j \\ f \in \mathcal{T}}} \sum_{\substack{f_{j+1} < ... < f_{j+k} \\ f \in \mathcal{P}}} P_{f_1 ... f_{f_{j+k}}}, \tag{4.26}$$

then one has

$$p'_{jk} = \sum_{u=j}^{N} \sum_{v=k}^{N-u} (-1)^{u-j+v-k} \binom{u}{u-k} \binom{v}{k-v} P'_{uv}. \tag{4.27}$$

With the probabilities of interest then given by

$$p_{kl} = p'_{N-k-l\,k}. \tag{4.28}$$

In the above expression $\mathcal{T}$ and $\mathcal{P}$ are the set of states on the target and on the projectile ($\tilde{\chi}^{00}_{Tk}$ and $\tilde{\chi}^{00}_{Pk}$ respectively). A model of this type which ignores the functional correlations discussed in Sec. 3.2 is consistent with an IEM description. An example of such a description is provided in Appendix C, in particular Eq. (C.11).

With the probabilities in hand the corresponding total cross section for each channel may then be calculated from

$$\sigma_{kl} = 2\pi \int_0^\infty b \, p_{kl}(b) \, \mathrm{d}b \tag{4.29}$$

in a similar manner to that of Eq. (3.33). It must be kept in mind that the above expression does not apply for σ_{10} which includes the elastic channel and must be treated with more care.

4.3 Results

4.3.1 1s-only Toy Model

Before presenting the results for the full system some of the details of a simplified toy model will be discussed. In this model only the $1s$ target and projectile states are included in the BGM basis. In this way one can ensure that the orbitals propagated by the dynamics code are the same as those passed into the KLI functional except that the former include the full ETFs while the latter can at most include partial ETFs.

(a) $E_P = 20$ keV/amu.

(b) $E_P = 1000$ keV/amu.
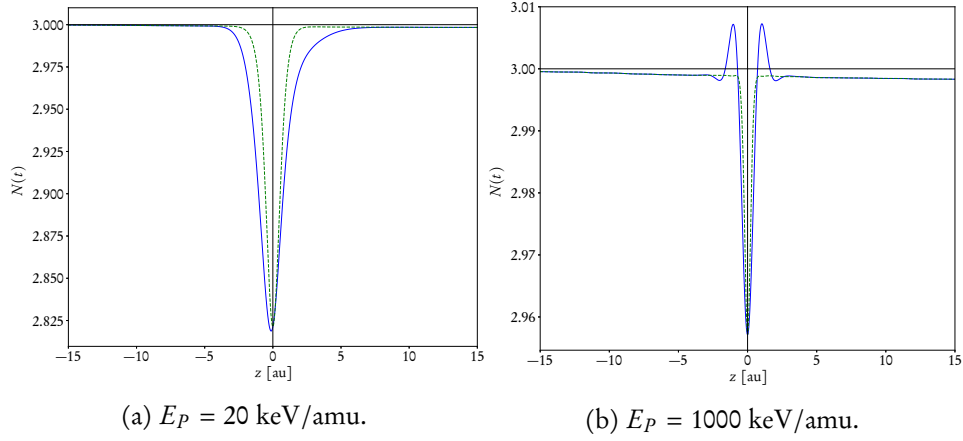
Figure 4.1: Number of particles as a function of z in $1s$-only toy model for $b = 1.0$ a.u. In both panels; solid line: ETF off, dashed line: partial ETF on.

A useful quantity to monitor is the norm of the one-particle density,

$$N(t) = \int \mathrm{d}^3 r \, n(\mathbf{r}, t). \tag{4.30}$$

Ionization having been excluded by construction within this model one should find $N(t) = 3$ for all time. Major violations of this can only be associated with the ETFs.

Figures 4.1a and 4.1b display N as a function of $z = Vt$ for collisions with impact energy of 20 keV/amu and 1000 keV/amu respectively. Both calculations including and excluding the partial ETFs use an impact parameter of 1 a.u and include response. While both curves show sizable norm violations the inclusion of a partial ETF offers clear benefits. The ETFs reduce the overall size of the violations and reduce the range of time over which these violations occur. This can be seen most clearly in Fig. 4.1a where the dashed curve detaches from the $N = 3$ line more slowly and reattaches more quickly. Additionally including ETFs corrects the unexpected asymmetry about $z = 0$ a.u.

The origins of the norm violations is easy to trace. According to Eq. (2.8) the

one-particle density may be written

$$n(\mathbf{r}, t) = \left|\varphi_{1\uparrow}\right|^2 + \left|\varphi_{2\uparrow}\right|^2 + \left|\varphi_{1\downarrow}\right|^2. \tag{4.31}$$

Each orbital in the above expression is normalized to 1 and takes the form

$$\varphi = a_T e^{i\mathbf{v}_T \cdot \mathbf{r}} \chi_T + a_P e^{-i\mathbf{v}_T \cdot \mathbf{r}} \chi_P. \tag{4.32}$$

Every orbital then contributes

$$\int d^3 r \, |\varphi|^2 = |a_T|^2 + |a_P|^2 + 2\Re \left[a_T^* a_P \tilde{S}_{TP} \right] \tag{4.33}$$

to N, where $\tilde{S}_{TP}$ are the matrix elements of the overlap matrix (including ETFs). It can then be seen that norm violations are due to the fact that the KLI implementation cannot fully account for the overlaps of the KS-orbitals, a direct consequence of its inability to deal with non-cylindrically symmetric orbitals.

The slight loss of norm noticeable in the tails of all four curves is on the order of 0.002. One can consider the small violation as a limit on the accuracy of calculations. This error is on the order of 0.06%.

4.3.2   IMPACT PARAMETER DEPENDENCE

Before discussing the total cross section results we present some of the lower level features of the full calculations. We consider the single-particle probabilities for each electron to ionize and to switch the nuclear centre to which it is bound. These probabilities can be calculated from the transition amplitudes. As an example, if $\varphi_{1\uparrow}$ begins initially on the target then the single-particle probability to ionize this electron can be written

$$p\left[\mathrm{He}(\uparrow_1) \to I\right] = \sum_{c \in \{T,P\}} \sum_{k=1}^{K} \sum_{l=1}^{L} \left|\langle \tilde{\chi}_{ck}^{l0} | \varphi_{1\uparrow}(t_f) \rangle\right|^2 \tag{4.34}$$

(a) $E_P = 10$ keV/amu.

(b) $E_P = 60$ keV/amu.

(c) $E_P = 250$ keV/amu.
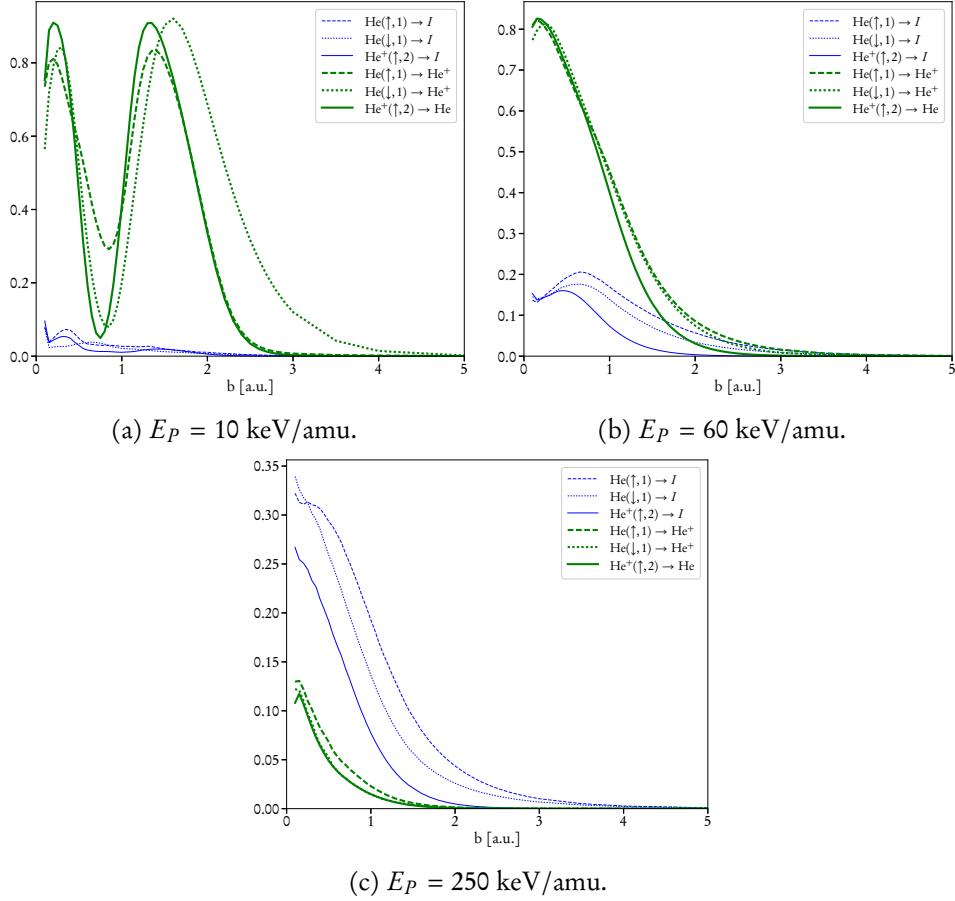
Figure 4.2: Single-particle transfer and ionization probabilities in He$^+$-He colli-sions at various impact energies.

and the single-particle probability to transfer to the projectile may be written

$$p\left[\text{He}(\uparrow_1) \to \text{He}^+\right] = \sum_{k=1}^{K} \left|\langle \tilde{\chi}_{Pk}^{00} | \varphi_{1\uparrow}(t_f) \rangle\right|^2, \qquad (4.35)$$

where the probabilities are defined in terms of orthogonalized orbitals including full ETFs. These probabilities are presented for the response model including partial ETFs at the impact energies of 10, 60 and 250 keV/amu in Fig. 4.2. When a distinction is made between response and no-response results the text refers to

cross sections calculated using either set of fully time-dependent 1s-only orbitals and those using the model described in the text surrounding Eq. (4.13) respectively. When no distinction is made the text refers simply to the response versions.

For low-energy collisions capture processes can be seen to be dominant, this is clearly depicted in Fiq. 4.2a where the single-particle ionization probabilities are negligible for the majority of impact parameters. In contrast, Fig. 4.2c shows the diminishing importance of capture over ionization as impact energies increase. As one would expect the probability to ionize the more tightly bound He^+ electron is consistently less than for either of the He electrons. Also of note is the obvious difference between the two He electrons, a clear reflection of the implementation of a spin-dependent potential.

One last point must be mentioned before closing the discussion of impact parameter dependent probabilities. Presented in Fig. 4.3 are integrands of Eq. (4.29) for several impact energies, that is, impact parameter dependent probabilities for the outcome channels of Eqs. (4.19)-(4.25) (with the addition of p_{00} and p_{30}) times the impact parameter. For $E_p \leq 500$ keV/amu the probabilities behave as one would expect. That is to say that the probabilities generally follow the relation $p(b) \sim b^{a_1} e^{-a_2 b}$ for some positive real numbers a_1 and a_2. However, above this level unphysical structures begin to emerge. As an example the p_{20} curve in Fig. 4.3c contains a large hump below 0.5 a.u.

These are the result of numerical issues that limit the minimum possible impact parameter for which the calculations produce results from 0.1 a.u. below 500 keV/amu gradually to 0.8 a.u. at 1000 keV/amu. In Eq. (4.29) the integrand, $b \, p_{kl}(b)$, is approximated by a cubic spline which is, in turn, integrated to arrive at a cross section. The structure of the integrand means that so long as $p_{kl}(0)$ is finite its value is irrelevant and we always know the integrand at $b = 0$. In Fig. 4.3 the solid portion of each curve represents the region where the probability may be determined at any point, the dashed sections represent the region where the spline interpolates between $b = 0$ and the next lowest available impact parameter. In the best possible scenario the lower bound on the error of a cubic spline will scale to the fourth power in the largest step between knots [162], for a spline s_f

(a) $E_P = 20$ keV/amu.

(b) $E_P = 500$ keV/amu.

(c) $E_P = 600$ keV/amu.
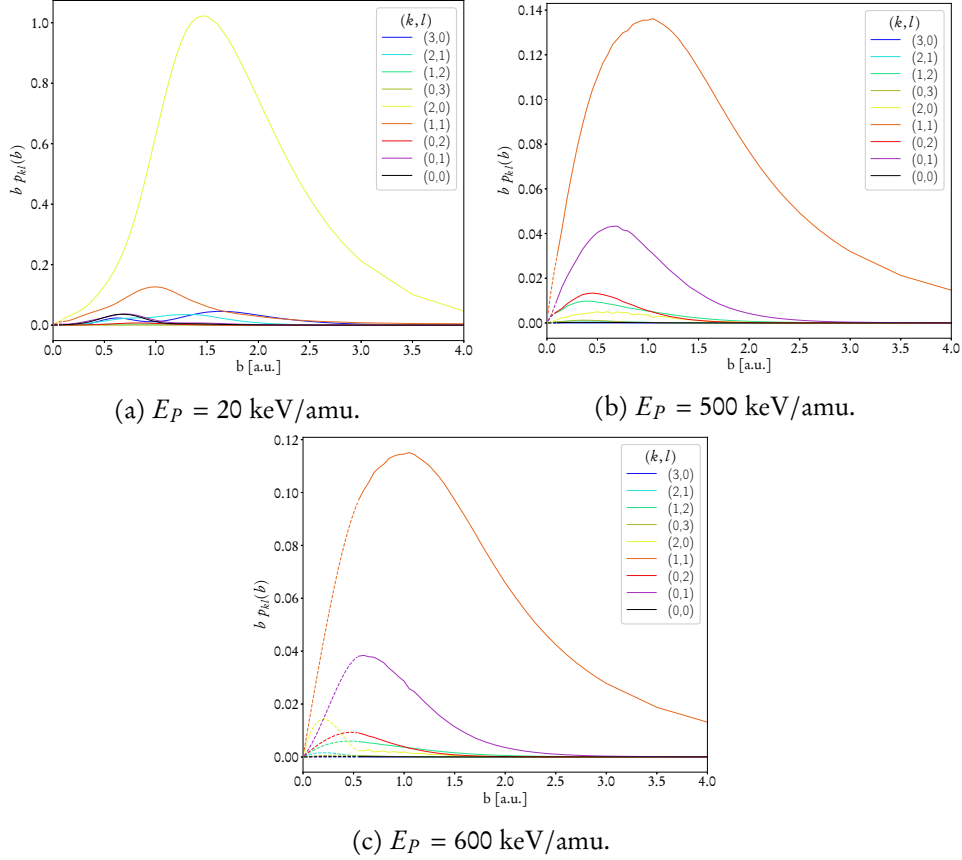
Figure 4.3: Impact parameter dependent probabilities for all outcome channels in He$^+$-He collisions. Dashed portions of curves represent the region where only the spline interpolant is available.

interpolating a function f one has

$$E(s_f) = \left| f - s_f \right|_\infty \leq \frac{5 \left| f^{(4)} \right|_\infty h^4}{384}, \tag{4.36}$$

where h is the largest separation between grid points used in determining the spline and

$$\left| g \right|_\infty = \sup_{x \in [a,b]} \left\{ \left| g(x) \right| \right\}. \tag{4.37}$$

The step size factor in the error bound then increases from 0.0001 to 0.4096, an

increase by an approximate factor of 4000. It is this decrease in the accuracy of the interpolation which results in the unphysical structures present in some outcome channels above 500 keV/amu. The presence of these structures are the reason for the lack of a data point at 800 keV/amu in Fig. 4.7, despite values having been calculated. These structures become most apparent in the inset to Fig. 4.8.

4.3.3 VISUALIZING THE TIME-DEPENDENT POTENTIAL

A considerable amount of information regarding the dynamics of the collision processes may be gleaned from an inspection of the KS-potential. If a picture is worth a thousand words then a thirty second long video at 24 fps is worth approximatetly 720 thousand words. To this end this subsection presents a collection of animations depicting the time evolution of the time-dependent KS potential. These videos may be found online[3].

When visualizing the KS potential it is best to consider only the electron-electron contributions, that is to ignore the external potential. This is beneficial because from the perspective of the current work we are primarily interested in the performance of our approximation to these portions of the potential. As the behaviour of the internuclear potential is well established tracking it is of little value. Additionally, the poles of the Couloumb potential will drown out the electron electron effects. For these reasons we will concern ourselves with just the electron-electron contributions

$$v_{\text{ee}}^{\sigma} = v_{\text{x}}^{\sigma} + v_{\text{H}}. \tag{4.38}$$

The spin-dependent electron-electron potentials are best shown along with the associated spin-densities, n_{σ} of Eq. (2.11) generated from the 1s-only orbitals in the PETF model. In this way one can more easily understand the appearance and time evolution of v_{ee}^{σ}. For example, $v_{\text{ee}}^{\uparrow}$ contains a single peak. This is due to the exact cancelation of self interaction that is present on the projectile centre where initially only one electron resides.

Figures 4.4 and 4.5 show a sample of several frames taken from the animation for a collision with an impact energy of 50 keV/amu and impact parameter

---

[3] https://tinyurl.com/ybo3yhqd

of 1.0 a.u. These figures depict the collisions process at the initial separation (Figs. 4.4a and 4.5a), at closest approach (Figs. 4.4b and 4.5b), and at the final time step (Figs. 4.4c and 4.5c). The arrangement of the collision system is easily determined by combining the initial spin-up and spin-down frames. Both of the density plots have peaks on the left, while only the spin-up density has a peak on the right clearly demonstrating that the target is on the left side of the figures. As these plots are presented in the rotating centre of mass frame the target and projectile remain on one side of the plane with the internuclear axis as normal.

At closest approach in Fig. 4.4b one may already see a second peak developing on the projectile as some of the norm is transfered between the collision centres. This interpretation is cemented in Fig. 4.4c where the one-particle density contains two distinct maxima.

The spin-up channels appear less active. This can be through the fact that up to closest approach the size and shape of the two peaks appear unchanged, only their positions are noticeably different. In the final frame a perceptible loss of norm from both centres is apparent. This may be seen as evidence that the Pauli exclusion promised by the x-potential is performing as advertised.

(a) $Z(t) = -40$ a.u..

(b) $Z(t) = 0$ a.u..

(c) $Z(t) = 40$ a.u..

Figure 4.4: Spin-down electron-electron potential compared with the spin-down component of the one-particle density intially (a), at closest approach (b), and finally. The parameters of the calculation are $E_P = 50$ keV/amu and $b = 1.0$ a.u.

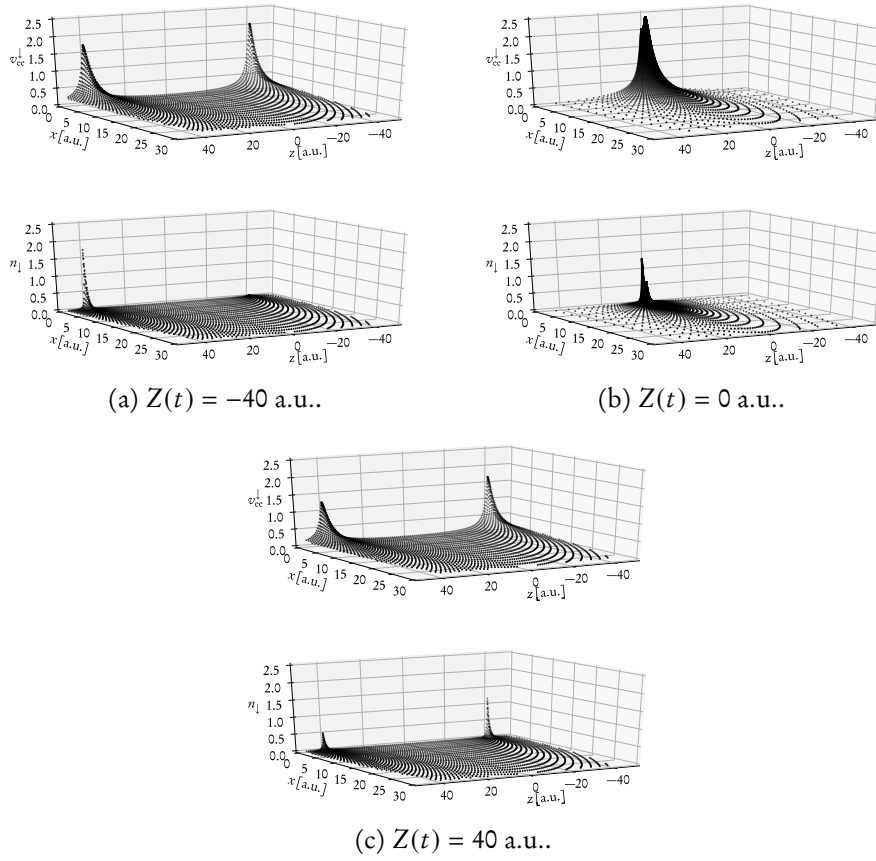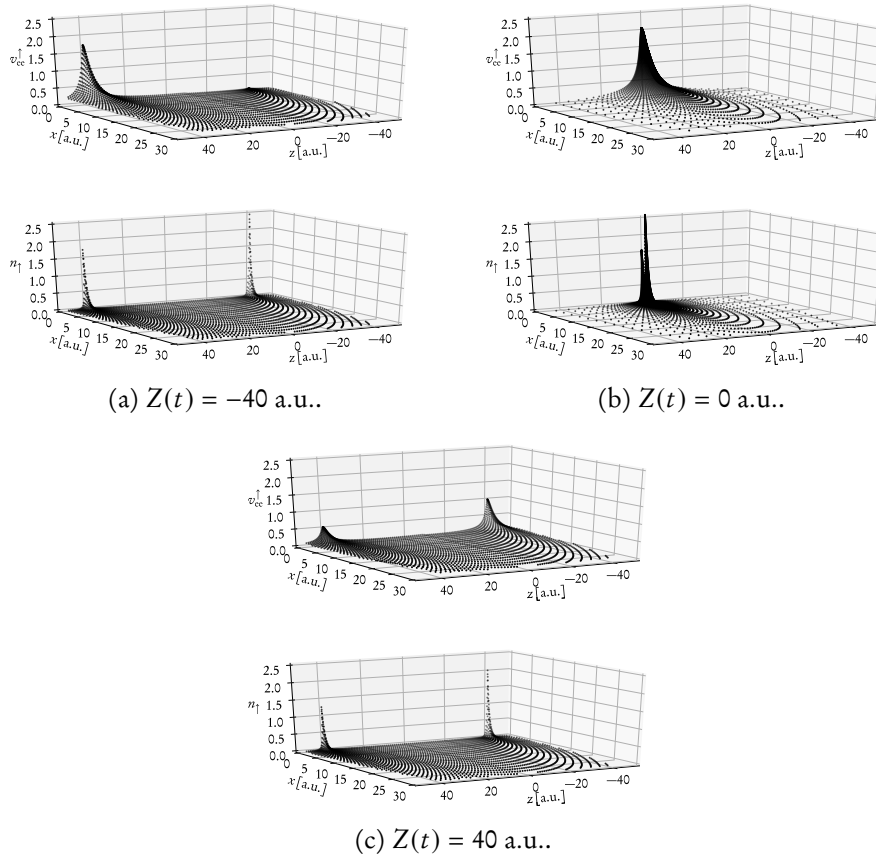(a) $Z(t) = -40$ a.u..

(b) $Z(t) = 0$ a.u..

(c) $Z(t) = 40$ a.u..

Figure 4.5: Spin-up electron-electron potential compared with the spin-up component of the one-particle density intially (a), at closest approach (b), and finally. The parameters of the calculation are $E_P = 50$ keV/amu and $b = 1.0$ a.u.

4.3.4 Cross Section Results

In what follows all results obtained by propagating the full KS orbitals in a potential generated from the 1s-only orbitals of Eq. (4.6) that include no electron translation factors will be designated by NETF. Those obtained by an application of the same processes using the 1s-only orbitals, with partial ETFs, of Eq. (4.12) will be referred to as PETF.

Where available the results of the current work are compared with calculations of other groups. It should be noted that only those calculations that describe the system quantum mechanically were considered, that is to say works that employ approaches such as the classical trajectory Monte Carlo method [163], the over the barrier model [164], or the Bohr–Lindhard model [121, 165] are not included.

We will begin our discussion of the total cross section results with a broad overview comparing the response and no-response calculations. In general for the cross sections presented in Figs. 4.6 through 4.14 the response calculations produce values that are noticeably lower with the exception of σ_{01} and σ_{00} (Figs. 4.7 and 4.13 respectively). Where the σ_{01} no-response curve drops below the response results appear to coincide with a spike in the response σ_{30} results (Fig. 4.14). The artificial nature of the σ_{00} channel makes determining whether the lower result is desirable or not difficult. The only other channel, apart from σ_{00}, where the no-response calculations are in better agreement with experiment is σ_{02}, Fig. 4.11, where lowering the results moves the response curve below experiment. The addition of response effects causing a decrease in charge-transfer cross sections is a typical result, see for example Ref. [77]. In general, response effects result in a transfer of of probability into the elastic channel, enhancing σ_{10}.

As was mentioned above the primary purpose of the no-response model in the present context was as a testbed for isolating the ETFs from other phase factors. If we consider only the physical outcome channels, i.e. exclude σ_{00} and σ_{03}, a clear pattern emerges. For low impact energies the NETF and PETF curves coincide, what one would expect as V approaches zero. As the impact energy increases a gap begins to open between the two sets of results. The only exceptions to this trend are σ_{20} (Fig. 4.8), where the cross sections are likely too large for small fluctuations to be apparent, and σ_{01} (Fig. 4.7) where the NETF and PETF

Figure 4.6: Total cross section for single ionization of the target. Theoretical results: ᴘᴇᴛꜰ response (solid line), ɴᴇᴛꜰ response (dotted line), ᴘᴇᴛꜰ no-response (dashed line), ɴᴇᴛꜰ no-response (dash-dotted line), and ᴄᴅᴡ-ᴇɪs of Miraglia and Gravielle [166] (thin solid line). Experimental data: diamonds [167], circles [168], and squares [169].

response curves are slightly erratic. Leaving aside this channel the tendencies of the response and no-response models in the presence, or absence, of the partial ᴇᴛꜰs are essentially identical. From the discussion in Sec. 4.3.1 it is clear that the ᴇᴛꜰs have no effect on v_H in the no-response model. One can interpret this to mean that the differences between the ɴᴇᴛꜰ and ᴘᴇᴛꜰ results are primarily attributable to the ᴇᴛꜰs and not the result of some unforeseen additional processes.

We now discuss the comparison of our response results with experimental data and other calculations by considering pure single ionization of the target, the process of Eq. (4.19). The results for this channel, σ_{11} are presented in Fig. 4.6. Both ɴᴇᴛꜰ and ᴘᴇᴛꜰ are in good agreement with experiment throughout the full range of impact energies. The slightly lower values for the ᴘᴇᴛꜰ version above 200 keV/amu make it a better fit to experiment. The underestimation of both curves below the peak corresponds almost exactly with the region where σ_{20} results begin to rise above the experimental results (see Fig. 4.8).
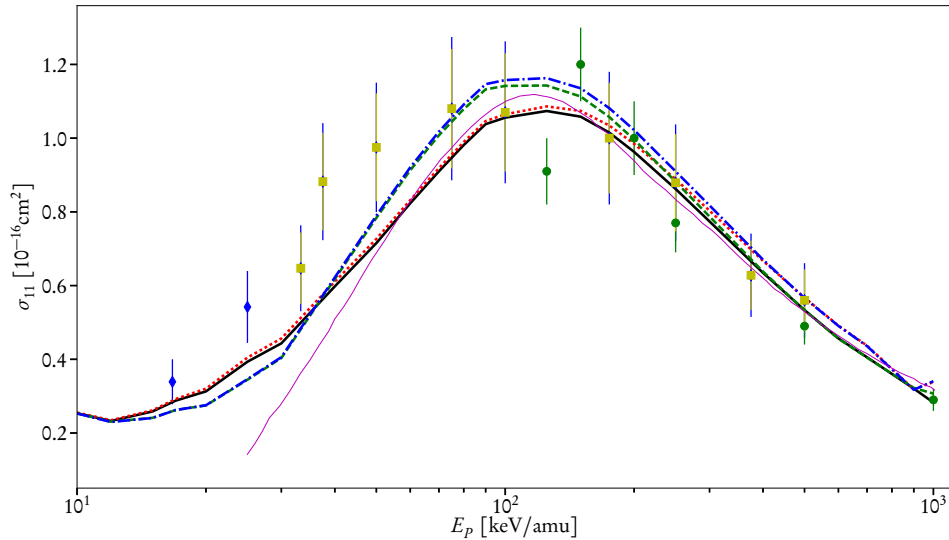
Figure 4.7: Total cross section for single ionization of the projectile. Theoretical results: PETF response (solid line), NETF response (dotted line), PETF no-response (dashed line), NETF no-response (dash-dotted line), and IEVM of Sigaud and Montenegro [170] (thin solid line). Experimental data: diamonds [167].

Also displayed in Fig. 4.6 are the continuum-distorted-wave eikonal-initial-state approximation (CDW-EIS) results of Miraglia and Gravielle [166]. These results seem to complement the results of the present work through the majority of the impact energy range. One notable exception to this is the slightly higher cross section maximum however. As there is a fairly large spread in the experimental data around this region it is difficult to say which is more accurate. The results of Miraglia and Gravielle also begin to diverge as one approaches lower impact energies. This feature is likely due in large part to the perturbative nature of CDW-EIS which becomes less reliable as one decreases the impact energy.

Next, we consider the results for σ_{01} [Eq. (4.21)] shown in Fig. 4.7. As with the previous channel both NETF and PETF results are in reasonable agreement with the experiment where it is available. Also following the general trend described above both models become essentially equal at low impact energies and separate as E_P increases. Both models begin to overestimate the data above the peak around 200 keV/amu. Once again the slightly lower PETF results are in better
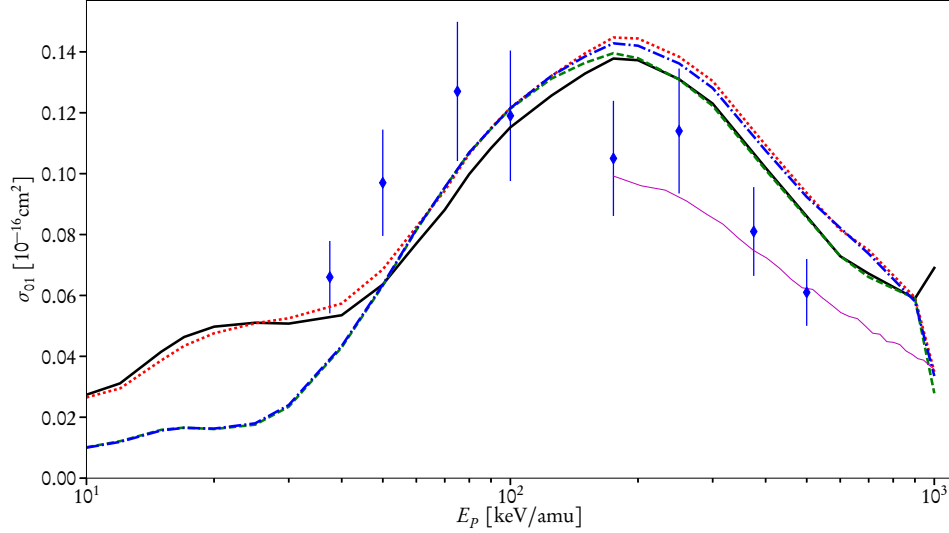
Figure 4.8: Total cross section for single capture to the projectile. Theoretical results: PETF response (solid line), NETF response (dotted line), PETF no-response (dashed line), NETF no-response (dash-dotted line), and CDBW-4B (post form) of Ghanbari-Adivi *et al.* [171] (thin solid line). Experimental data: diamonds [167] and circles [168]. Inset presents the same data on a log-log scale.

agreement with experiment. The slight unphysical structures in the curves below 40 keV/amu seem to correspond with the peaks of the σ_{00} channel. This issue will be discussed in greater detail below.

These calculations have been compared with the independent event model (IEVM) results of Sigaud and Montenegro [170]. While they do not directly report σ_{01} they do present σ_{02}, σ_{03}, and what they call total electron loss (we will denote this by σ_{total}). Using the relation

$$\sigma_{\text{total}} = \sigma_{01} + \sigma_{02} + \sigma_{03} \tag{4.39}$$

one can easily determine σ_{01} from their disclosed results. Their values seem to be in much better agreement with experiment in the high-energy range than either the NETF or PETF models. This can perhaps be explained by the presence of correlation in the IEVM calculations. As will be discussed in more detail
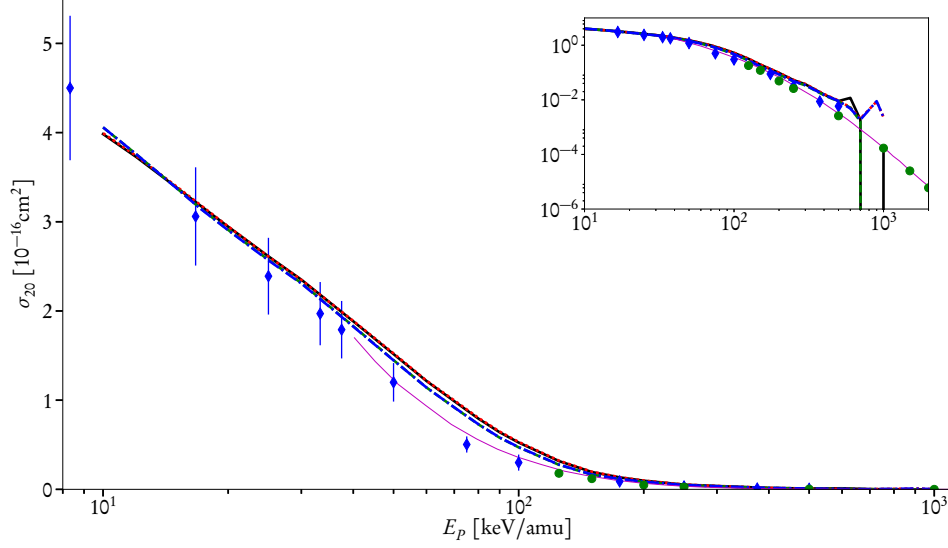
Figure 4.9: Total cross section for double ionization of the target. Theoretical results: PETF response (solid line), NETF response (dotted line). PETF no-response (dashed line), and NETF no-response (dash-dotted line). Experimental data: diamonds [167], circles [168], and squares [169].

below all of our models underestimate σ_{02} and σ_{03} in this impact energy range. Keeping in mind that $\sum p_{kl} = 1$ the increase in these channels resulting from the incorporation of correlation effects, so-called antiscreening in particular, would be drawn in part from the current channel of focus σ_{01} resulting in a decrease, putting our results and theirs in better agreement with both Sigaud and Montenegro and the experimental data.

For the results of single electron capture to the projectile, the process of Eq. (4.20) depicted in Fig. 4.8, both NETF and PETF models are essentially identical. This is what one would hope for as they are in good agreement with experiment in the entire range of impact energies, keeping in mind that the unphysical structures resulting from a lack of low impact parameter data for collisions with impact energies above 500 keV/amu (discussed in Sec. 4.3.2) are exaggerated by the log-log scale of the inset plot. A possible explanation of the slight discrepancy between theory and experiment in the 50-150 keV/amu interval is offered by a comparison with the four-body Coulomb–Born distorted wave approximation
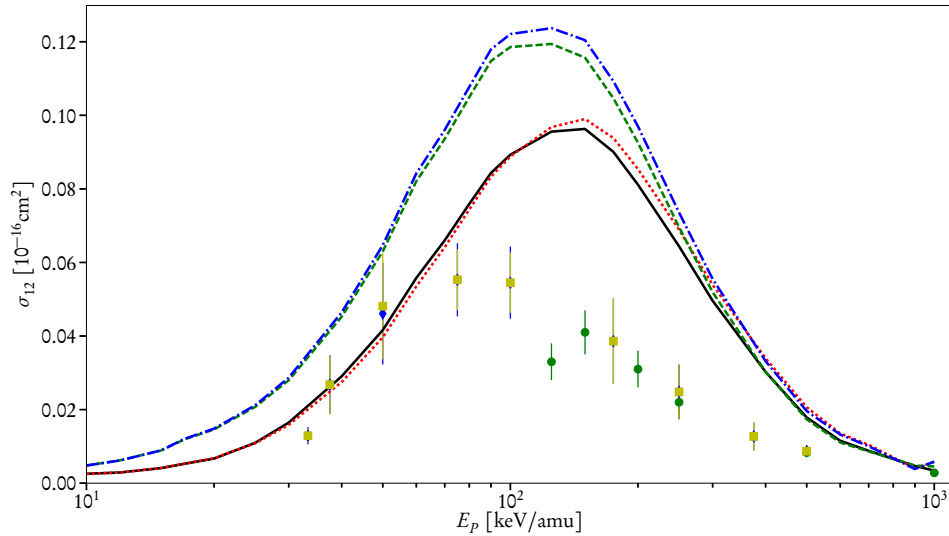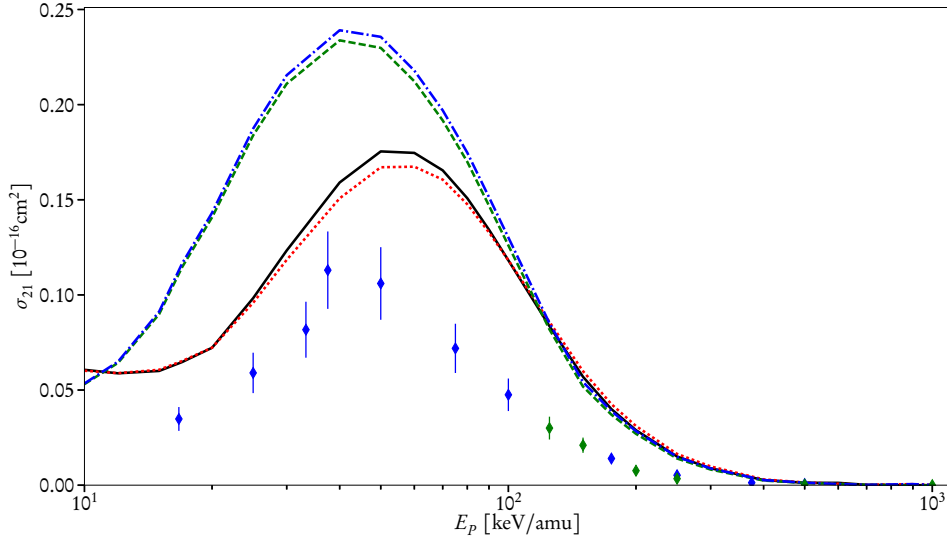
Figure 4.10: Total cross section for transfer ionization of the target. Theoretical results: pETF response (solid line), nETF response (dotted line), pETF no-response (dashed line), and nETF no-response (dash-dotted line). Experimental data: diamonds [167] and circles [168].

(CDBW-4B) results of Ghanbari-Adivi *et al.* [171]. The correlation effects included in this model may point to the slight rise in cross section being related to the fact that we have employed an IEM approximation. Alternatively, the rise may be due to a failure of the partial ETF.

The latter explanation may provide a more satisfying solution to this problem. One would expect that capture processes should be dominated by the contributions of slow and close collisions. The regions where the n/pETF models start to diverge from experiment is approximately the region where both models begin to diverge in other channels (see for example σ_{12} in Fig. 4.9), that is the lowest energies where ETFs are important. Additionally they begin to agree with experiment once the cross sections begin to rapidly approach zero, for fast collisions. This would seem to be an indication that correct ETFs are important for capture processes (a fact that should be at least intuitively obvious).

A few words should be spent addressing the choice for the theoretical calculation compared against. Unlike other channels there exists a relatively large
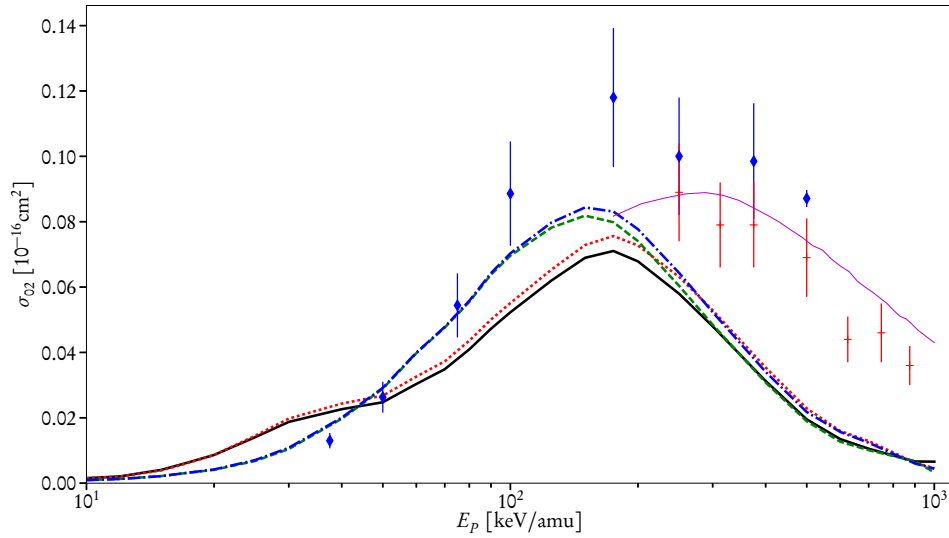
Figure 4.11: Total cross section for simultaneous single ionization of the target and projectile. Theoretical results: PETF response (solid line), NETF response (dotted line), PETF no-response (dashed line), NETF no-response (dash-dotted line), and IEVM of Sigaud and Montenegro [170] (thin solid line). Experimental data: diamonds [167] and crosses [172].

number of works to select from that fit the criteria listed above. As the majority of these belong to a family of related perturbative models [166, 171, 175–179] the latest, that of Ghanbari-Adivi *et al.*, was chosen. A comparison of the work of Ghanbari-Adivi *et al.* with several earlier perturbative calculations can be found in Ref. [171].

With the single-electron processes taken care of double target ionization, Eq. (4.22), the first of the two-electron processes will be considered next. The results for this channel are presented in Fig. 4.9. As with previous channels both NETF and PETF results appear to be very similar with a slight edge going to the PETF model's marginally lower results above 100 keV/amu. Both models seem to shift the peak in the cross section to higher impact energy than experiment would suggest is correct. As one would expect from an IEM the two models exaggerate double ionization, see for example Refs. [70, 134]. As there are no previous works fitting the conditions for inclusion listed earlier little else can be concluded about
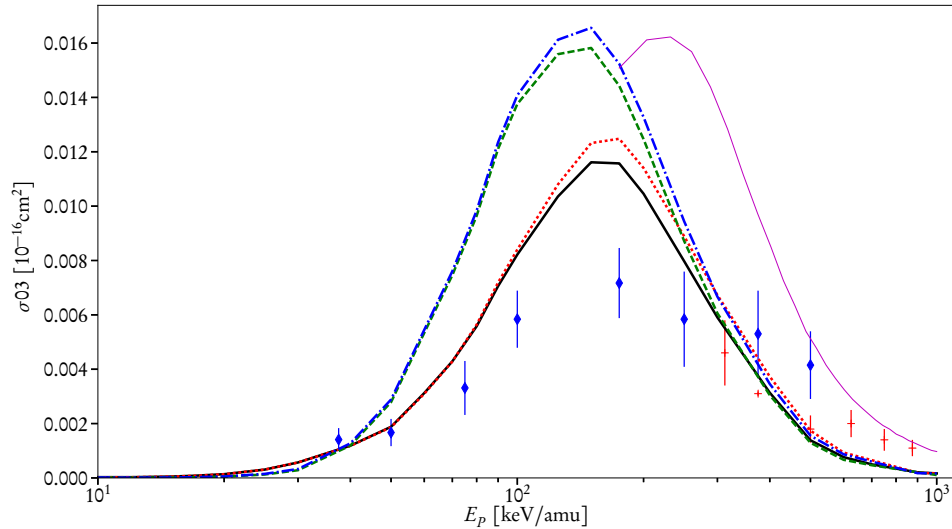
Figure 4.12: Total cross section simultaneous double target and single projectile ionization. Theoretical results: PETF response (solid line), NETF response (dotted line), PETF no-response (dashed line), NETF no-response (dash-dotted line), and IEVM of Sigaud and Montenegro [170] (thin solid line). Experimental data: diamonds [167] and crosses [172].

the results of the present work.

Another channel where the literature lacks a proper touchstone is that of transfer ionization [Eq. (4.24) shown in Fig. 4.10]. The trends for σ_{21} are very similar to those of σ_{12}. As with the previously discussed process both models are above experiment and shift the experimental peak to a higher impact energy. The only significant difference is that this is one of the few channels where the NETF model tends to give larger cross section values and is in slightly better agreement with experiment than the PETF. The flattening of the curves below 20 keV/amu is an artifact of the TC-BGM becoming less reliable at the lowest impact energies.

The last two-electron process is simultaneous single ionization of the target and projectile, Eq. (4.23). The results for our NETF and PETF models are presented in Fig. 4.11. These results both follow the trend of the data quite closely, arguably matching the position of the peak in the experimental cross sections. This channel is the second of two where the NETF model has a slight egde over the results of the

Figure 4.13: Total cross section for capture to the target in He$^+$-He collisions. Theoretical results: PETF response (solid line), NETF response (dotted line), PETF no-response (dashed line), and NETF no-response (dash-dotted line).

Figure 4.14: Total cross section for double capture to the projectile in He$^+$-He. Theoretical results: PETF response (solid line), NETF response (dotted line), PETF no-response (dashed line), and NETF no-response (dash-dotted line).

PETF. Unfortunately they fall below experiment for the majority of the impact energy range shown.

A comparison with the IEVM of Sigaud and Montenegro explains this fact. Sigaud and Montenegro claim to capture the effects of antiscreening, the direct interaction between target and projectile electrons, which becomes increasingly important for projectile ionization processes at larger impact energies. As the results of the current work are those of an IEM they make no effort to capture any correlation effects. Sigaud and Montenegro's efforts to capture antiscreening see their results fall within experiment for their entire extent. Encouragingly, if one were to extend the curve of Sigaud and Montenegro it would seem to overlap with the results of the present work lending credence to the curve in the region below the cross section peak, where antiscreening cannot contribute.

Next we consider the sole three electron process, simultaneous double target and single projectile ionization [Eq. (4.25)]. The results, presented in Fig. 4.12, again follow the general trends found in the previously discussed channels; over-estimation of the cross section peak and a slightly better showing for the PETF model over the results of the NETF model. Unlike for previous channels our results
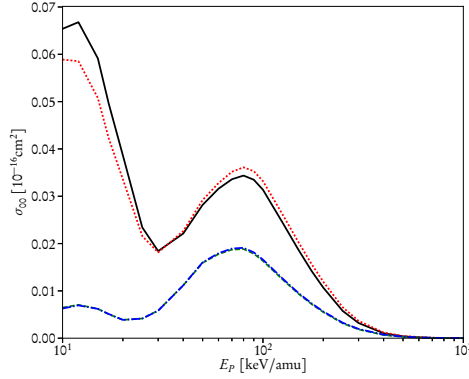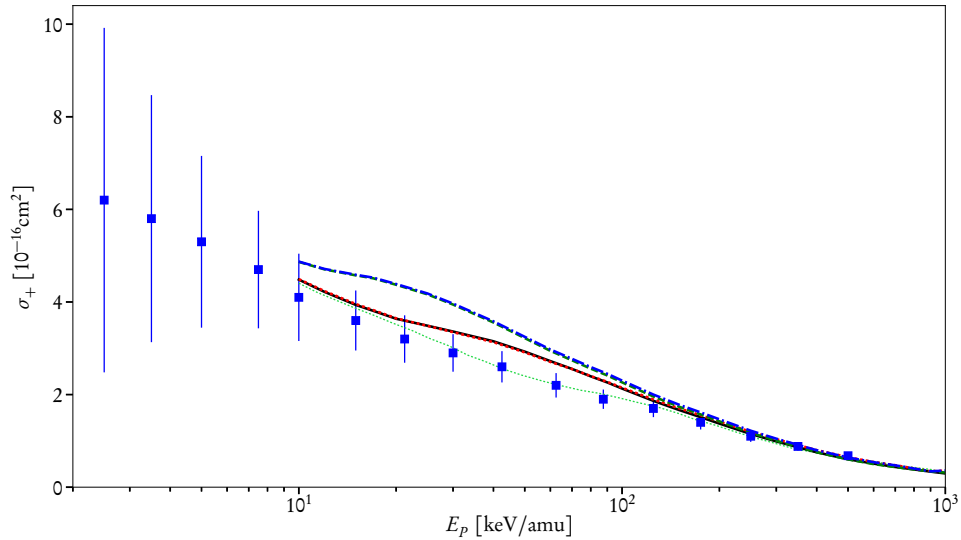
Figure 4.15: Total cross section for net recoil ion production in He$^+$-He collisions. Theoretical results: PETF response (solid line), NETF response (dotted line), PETF no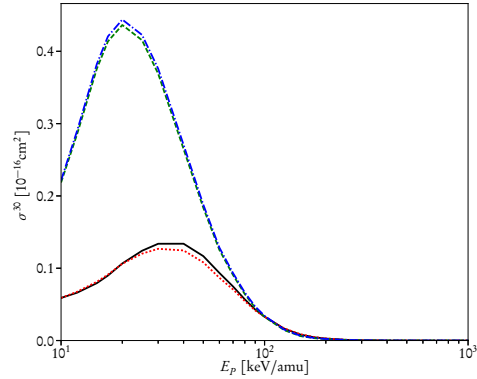-response (dashed line), NETF no-response (dash-dotted line), and CMF of Schenk [173] (thin dotted line). Experimental data: squares [174].

are in better agreement with experiment than those of Sigaud and Montenegro which overestimate the cross sections to a greater extent and over a larger impact energy range. As in previous channels the underestimation of our cross sections at larger impact energies may be attributed to correlation effects, in particular, to antiscreening which Sigaud and Montenegro seem to exaggerate in this channel.

In addition to the outcome channels discussed above there are three further processes. One, σ_{10}, has been left out as it involves no charge transfer. The other two, σ_{00} and σ_{30}, involve all three electrons bound to either the target or the projectile and are displayed in Figs. 4.13 and 4.14. As was pointed out earlier these channels should not be considered due to the fact that the production cross sections for these configurations should be negligible, but unfortunately in our results they are not. While modelling the initial and final states of the system as single Slater determinants accounts for Pauli exclusion which precludes all three electrons from occupying the ground state there is nothing in the model to stop additional electrons from being captured and remaining in excited states. Keeping

in mind that this model is simply an example of an IEM, albeit a sophisticated one, the probabilities for these unphysical channels will behave in a predictable manner $p_{00} \sim p_T{}^3$ and $p_{30} \sim p_P{}^3$. The inclusion of functional correlation should, in principle, provide an offset. An exaggerated example of this is provided in Chap. 3 where a WB type model could potentially cause both channels to be zero. The only recourse, short of implementing a model which contains at least some functional correlation, is to artificially redistribute the probability from p_{00} and p_{30} into other channels.

Two options immediately present themselves. The first possibility is to feed the extra probability into the corresponding ionization channels. In other words, p_{00} and p_{30} would augment p_{01} and p_{21} respectively. With the peak in σ_{30} approximately matching that of σ_{21} in both position and magnitude this solution would lead to a doubling of the overestimation present in the σ_{21} channel. A similar issue would arise in the lower impact energy range of the σ_{01} curve. This leaves one with the second option, to put the extra probability from p_{00} into p_{10} and feed p_{30} into p_{20}. The only effect this could have on the presented results would be to increase σ_{20} however, as σ_{30} is at worst an order of magnitude less than σ_{20} it would provide only a small shift in the curve displayed in Fig. 4.8.

To close out this section we will consider the total cross section for net recoil ion production. This quantity, presented in Fig. 4.15, may be calculated from previously presented results

$$\sigma_+ = \sigma_{11} + \sigma_{20} + \sigma_{02} + 2\sigma_{12} + 2\sigma_{21} + 2\sigma_{03} + 2\sigma_{30}. \tag{4.40}$$

Just as in the separate channels the response results are lower than those of the no-response model for the majority of the impact energy range putting them in fair agreement with experiment outside of the imtermediate energy range. No distinction between NETF and PETF curves is discernible.

Also depicted in Fig. 4.15 are the common mean field (CMF) results of Schenk [173], which are in good agreement with experiment. The difference between the CMF results and those of the current work can be traced to the overestimation of single capture (see discussion above and Fig. 4.8). As was discussed in Ref. [173] the CMF model is very well suited for describing processes involving

initial target electrons. This in large part due to the fact that in the CMF both target and projectile electrons are propagated with the same Hamiltonian, that of the target. One can see this as evidence that the current work trades an excellent description of a single centre for a slightly less realistic description of both atomic centres.

CHAPTER 5

CONCLUSIONS

Following the programme laid out in the introduction this work has presented investigations of an increasingly complex series of ion-atom collisions systems. This journey began with the relatively simple antiproton-helium system, continued with the proton-helium and He^{2+}-He systems, and culminated in a discussion of the He^+-He collision system. In the following subsections more detailed and collision specific conclusions will be offered for these investigations. Before embarking on a summary of individual results it is, perhaps, necessary to emphasize one of the overarching themes of this work. In most situations our results are competitive with the best models of others. In many cases our results are the only ones which can consistently describe all outcome channels for a given collision system, that is they produce some of the best results available without being focused on a specific process. This certainly demonstrates the utility of density functional theory techniques over a fairly wide range of systems.

5.1 p-HE AND He^{2+}-HE COLLISIONS

We have investigated correlation effects in p-He and He^{2+}-He collisions. By expanding the correlation integral model of Wilken and Bauer [18] applied previously to the antiproton-helium system [19] we have produced total cross sections for single, double, and transfer ionization as well as single and double capture. In order to incorporate electron capture processes into the WB model

two additional correlation integrals, one centred on the projectile (I_c^{PP}) and the other two-centred (I_c^{TP}), were introduced. While I_c^{PP} was dealt with using straightforward modification of the original wb model. I_c^{TP} was determined based on the values of the other correlation integrals and the single-particle probabilities, p_T and p_P. The use of this model was justified by the favourable p-He results for single capture that depend explicitly only on I_c^{TP}.

For the majority of the channels investigated the wb model represents a clear improvement over iem results, the most notable exceptions being the double ionization results at low and intermediate impact energies. Where enough correlated two-electron calculations exist to make a proper comparison these fully correlated calculations represent a much larger improvement over iem than wb results.

Overall it appears that the p-He results are superior to those of the He^{2+}-He system. The variation in the quality of results may be attributed to the increased charge of the projectile. The stronger potential well on the projectile results in an increase in the role of capture in the dynamics. Immediately, this means that the problems present in all calculations of separating the target, capture, and ionizing regions becomes amplified. The increased role of capture also enters into the wb model itself where the previously closed $p_P > 1/2$ branches of the correlation integrals are opened, further complicating the analysis. The lack of a full reference calculation over a wide impact energy range makes separating these issues all the more difficult.

The opening of the capture channels introduces additional complications into the wb model. First, it accentuates some of the shortcomings of the underlying dynamic calculation. While some gains may be made by rerunning these calculations using the full tc-bgm the base level accuracy of the method is essentially fixed (especially at low impact energies). One could take this as further confirmation that no single calculation is yet capable of covering vast tracts of impact energy space [180]. In this regard our results cover more channels, over a larger energy range than most.

Second, the wb model itself appears to distribute probabilities among the six outcome channels in unphysical ways (for example causing double and transfer ionization in p-He collisions to be equal). While the precise origin of these issues is not currently known at least some blame must be taken by the piece-wise

nature of the adiabatic approximation which causes only one of I_c^{TT} or I_c^{PP} to be nontrivial at any given impact parameter. Another source of poor probability partitioning is the model chosen for I_c^{TP} which, as mentioned above, causes $p_{II} = p_{IP}$. Regardless of the provenance of these issues further applications of the wb model in the context of capture are inadvisable. This should, however, not be interpreted as a criticism of correlation-integral models in general it is merely a reflection of the wb model's apparent limitations. Work in this vein can be made easier provided more correlated two-electron calculations become available.

5.2   He$^+$-He Collisions

The He$^+$-He collision system was investigated within time-dependent spin-density functional theory under the constraints of the exchange-only approximation. An accurate time-dependent exchange potential was determined through the application of the kli approximation. Total cross section results for all physical outcome channels were then offered in the approximate impact energy range of 10-1000 keV/amu for two models; one in which electron translation factors were ignored and a second model where partial etfs were used. The results of both models are in overall good agreement with experiment.

Without diminishing the results of this work it is necessary to highlight a few limitations and where the results may be improved in future iterations. First, the restriction of the implementation of the kli functional to systems of cylindrical symmetry is the impetus for both the 1s-only approximation as well as the need to consider both the netf and petf models. Future applications of the procedure laid out in this work would benefit greatly from a fully three-dimensional implementation of the kli functional that makes no symmetry assumptions. Failing this, it may be possible to express the ks orbitals in terms of a multipole expansion. In this way more complex, symmetry respecting orbitals may be obtained.

Comparisons of our results with the theoretical works of other groups points to the fact that the calculations would also gain from the inclusion of correlation effects. Treating this x-only version as a proof of concept there is nothing, apart from the added complexity of the calculations, precluding the addition of dynamic

correlation through the application of any number of ground-state correlation functionals in the future. It should be noted that such a model would still not offer a complete description of time-dependent correlation, it would, for example, lack memory effects [11]. It should then be clear that even an adiabatically exact potential could not produce ccompletely accurate dynamics [181]. An added difficulty would be the inclusion of functional correlation effects. In order to move beyond the IEM single Slater determinant description of outcome probabilities, one would have to adapt a model, preferably one that avoids the problems of the model of Wilken and Bauer [18] used in Chap. 3 (and Ref. [70]) to explicitly spin-polarized systems. A starting point for such a model is outlined in Appendix C.

REFERENCES

[1] R. C. Isler. "A review of charge-exchange spectroscopy and applications to fusion plasmas". In: *Physica Scripta* 35.5 (1987), p. 650.

[2] R. C. Isler. "An overview of charge-exchange spectroscopy as a plasma diagnostic". In: *Plasma Physics and Controlled Fusion* 36.2 (1994), p. 171.

[3] T. E. Cravens. "X-ray emission from comets". In: *Science* 296.5570 (2002), pp. 1042–1045.

[4] P. Beiersdorfer, K. R. Boyce, G. V. Brown, H. Chen, S. M. Kahn, R. L. Kelley, M. May, R. E. Olson, F. S. Porter, C. K. Stahle, and W. A. Tillotson. "Laboratory simulation of charge exchange-produced x-ray emission from comets". In: *Science* 300.5625 (2003), pp. 1558–1559.

[5] W. Guo and D. N. McKinsey. "Concept for a dark matter detector using liquid helium-4". In: *Phys. Rev. D* 87 (11 June 2013), p. 115001.

[6] I. K. Gainullin and M. A. Sonkin. "High-performance parallel solver for 3D time-dependent Schrodinger equation for large-scale nanosystems". In: *Computer Physics Communications* 88 (2015), pp. 68 –75.

[7] M. S. Pindzola, J. Colgan, F. Robicheaux, T. G. Lee, M. F. Ciappina, M. Foster, J. A. Ludlow, and S. A. Abdel-Naby. "Time-Dependent Close-Coupling Calculations for Ion-Impact Ionization of Atoms and Molecules". In: *Advances In Atomic, Molecular, and Optical Physics* 65 (2016), pp. 291 –319.

[8] D. Belkić, I. Mančev, and J. Hanssen. "Four-body methods for high-energy ion-atom collisions". In: *Rev. Mod. Phys.* 80 (1 Jan. 2008), pp. 249–314.

[9] D. Belkić. "Review of theories on double electron capture in fast ion-atom collisions". In: *Journal of Mathematical Chemistry* 47.4 (May 2010), pp. 1420–1467.

[10] R. Olson. "Classical Trajectory and Monte Carlo Techniques". In: *Springer Handbook of Atomic, Molecular, and Optical Physics*. Ed. by G. Drake. New York, NY: Springer New York, 2006. Chap. 58, pp. 869–874.

[11] M. A. Marques, N. T. Maitra, F. Fernando M.S. Nogueira, E. K. U. Gross, and A. Rubio, eds. *Fundamentals of time-dependent density functional theory*. Vol. 837. Lecture Notes in Physics. Berlin: Springer Berlin Heidelberg, 2012.

[12] C. A. Ullrich. *Time-dependent density-functional theory: Concepts and applications*. Oxford University Press, 2011.

[13] T. Kirchner, H. J. Lüdde, and M. Horbatsch. "A time-dependent quantal approach to electronic transitions in atomic collisions". In: *Recent Res. Devel. in Physics* 5 (2004), p. 433.

[14] S. Botti, A. Schindlmayr, R. Del Sole, and L. Reining. "Time-dependent density-functional theory for extended systems". In: *Reports on Progress in Physics* 70.3 (2007), p. 357.

[15] A. D. Laurent and D. Jacquemin. "TD-DFT benchmarks: A review". In: *International Journal of Quantum Chemistry* 113.17 (2013), pp. 2019–2039.

[16] E. Runge and E. K. U. Gross. "Density-Functional Theory for Time-Dependent Systems". In: *Phys. Rev. Lett.* 52 (12 Mar. 1984), pp. 997–1000.

[17] H. J. Lüdde. "Time-dependent density functional theory in atomic collisions". In: *Many-Particle Quantum Dynamics in Atomic and Molecular Fragmentation*. Ed. by J. Ullrich and V. Shevelko. Springer Series on Atomic, Optical, and Plasma Physics. Springer, 2003. Chap. 12.

[18] F. Wilken and D. Bauer. "Adiabatic approximation of the correlation function in the density-functional treatment of ionization processes". In: *Phys. Rev. Lett.* 97 (20 Nov. 2006), p. 203001.

[19] M. Baxter and T. Kirchner. "Correlation in time-dependent density-functional-theory studies of antiproton-helium collisions". In: *Phys. Rev. A* 87 (6 June 2013), p. 062507.

[20] E. Engel and R. M. Dreizler. *Density Functional Theory: an advanced course*. Berlin ; Heidelberg ; New York: Springer, 2011.

[21] E. K. U. Gross and K. Burke. "Basics". In: *Time-Dependent Density Functional Theory*. Ed. by M. A. Marques. Berlin: Springer-Verlag, 2006. Chap. 1.

[22] P. Hohenberg and W. Kohn. "Inhomogeneous Electron Gas". In: *Phys. Rev.* 136 (3B Nov. 1964), B864–B871.

[23] N. T. Maitra and K. Burke. "Demonstration of initial-state dependence in time-dependent density-functional theory". In: *Phys. Rev. A* 63 (4 Mar. 2001), p. 042501.

[24] N. T. Maitra and K. Burke. "Erratum: Demonstration of initial-state dependence in time-dependent density-functional theory [Phys. Rev. A 63, 042501 (2001)]". In: *Phys. Rev. A* 64 (3 Aug. 2001), p. 039901.

[25] N. T. Maitra and K. Burke. "On the Floquet formulation of time-dependent density functional theory". In: *Chemical Physics Letters* 359.3 (2002), pp. 237 –240.

[26] P. Samal and M. K. Harbola. "Analysis of Floquet formulation of time-dependent density-functional theory". In: *Chemical Physics Letters* 433.1–3 (2006), pp. 204 –210.

[27] N. T. Maitra and K. Burke. "Comment on "Analysis of Floquet formulation of time-dependent density-functional theory"[Chem. Phys. Lett. 433 (2006) 204]". In: *Chemical Physics Letters* 441.1 (2007), pp. 167 –169.

[28] A. Holas and R. Balawender. "Maitra-Burke example of initial-state dependence in time-dependent density-functional theory". In: *Phys. Rev. A* 65 (3 Mar. 2002), p. 034502.

[29] U. von Barth and L. Hedin. "A local exchange-correlation potential for the spin polarized case. I". In: *Journal of Physics C: Solid State Physics* 5.13 (1972), p. 1629.

[30] M. M. Pant and A. K. Rajagopal. "Theory of inhomogeneous magnetic electron-gas". In: *Solid State Communications* 10.12 (1972), pp. 1157 + .

[31] M. Petersilka and E. K. U. Gross. "Spin-multiplet energies from time-dependent density functional theory". In: *International Journal of Quantum Chemistry* 60.7 (Dec. 1996), pp. 1393–1401.

[32] W. Kohn and L. J. Sham. "Self-Consistent Equations Including Exchange and Correlation Effects". In: *Phys. Rev.* 140 (4A Nov. 1965), A1133–A1138.

[33] A. K. Rajagopal and J. Callaway. "Inhomogeneous Electron Gas". In: *Phys. Rev. B* 7 (5 Mar. 1973), pp. 1912–1919.

[34] S. K. Ghosh and A. K. Dhara. "Density-functional theory of many-electron systems subjected to time-dependent electric and magnetic fields". In: *Phys. Rev. A* 38 (3 Aug. 1988), pp. 1149–1158.

[35] M. Levy. "Electron densities in search of Hamiltonians". In: *Phys. Rev. A* 26 (3 Sept. 1982), pp. 1200–1208.

[36] E. H. Lieb. "Density functionals for Coulomb systems". In: *Physics as natural philosophy*. Ed. by A. Shimony and H. Feshbach. Cambridge, Massachusetts: MIT Press, 1982. Chap. 9, pp. 110–149.

[37] H. Englisch and R. Englisch. "Hohenberg-Kohn theorem and non-v-representable densities". In: *Physica A-statistical mechanics and its applications* 121.1-2 (1983), pp. 253–268.

[38] J. T. Chayes, L. Chayes, and M. B. Ruskai. "Density functional approach to quantum lattice systems". In: *Journal of Statistical Physics* 38.3 (1985), pp. 497–518.

[39] H. Englisch and R. Englisch. "Exact density functionals for ground-state energies .1. general results". In: *Physica Status Solidi B-Basic Research* 123.2 (1984), pp. 711–721.

[40] H. Englisch and R. Englisch. "Exact density functionals for ground-state energies .2. details and remarks". In: *Physica Status Solidi B-Basic Research* 124.1 (1984), pp. 373–379.

[41] M. Levy. "Universal variational functionals of electron-densities, first-order density-matrices, and natural spin-orbitals and solution of the v-representability problem". In: *Proceedings of the National Academy of Sciences of The United States of America* 76.12 (1979), pp. 6062–6065.

[42] E. H. Lieb. "Density functionals for coulomb-systems". In: *International Journal of Quantum Chemistry* 24.3 (1983), pp. 243–277.

[43] R. van Leeuwen. "Density functional approach to the many-body problem: Key concepts and exact functionals". In: *Advances in Quantum Chemistry, vol 43*. Ed. by J. R. Sabin and E. Brandas. Vol. 43. Advances in Quantum Chemistry. CA, USA: Elsevier Academic Press INC, 2003, pp. 25–94.

[44] P. O. Lowdin and P. K. Mukherjee. "Some comments on time-dependent variation principle". In: *Chemistry and Physics of Lipids* 14.1 (1972), pp. 1+.

[45] M. Y. Amusia and V. R. Shaginyan. "Relations between action integral, response functions, and causality in density functional theory". In: *Physics Letters A* 250.1-3 (Dec. 1998), pp. 157–162.

[46] H. Kohl and R. M. Dreizler. "Time-dependent density-functional theory: conceptual And practical aspects". In: *Phys. Rev. Lett.* 56 (19 May 1986), pp. 1993–1995.

[47] M. Ruggenthaler, M. Penz, and R. van Leeuwen. "Existence, uniqueness, and construction of the density-potential mapping in time-dependent density-functional theory". In: *Journal of Physics: Condensed Matter* 27.20 (2015), p. 203202.

[48] R. van Leeuwen. "Causality and symmetry in time-dependent density-functional theory". In: *Phys. Rev. Lett.* 80 (6 Feb. 1998), pp. 1280–1283.

[49] G. Vignale. "Real-time resolution of the causality paradox of time-dependent density-functional theory". In: *Phys. Rev. A* 77 (6 June 2008), p. 062511.

[50] P. A. M. Dirac. "Note on exchange phenomena in the Thomas atom". In: *Mathematical Proceedings of the Cambridge Philosophical Society* 26.3 (1930), 376–385.

[51] J. P. Perdew, A. Ruzsinszky, J. M. Tao, V. N. Staroverov, G. E. Scuseria, and G. I. Csonka. "Prescription for the design and selection of density functional approximations: More constraint satisfaction with fewer fits". In: *Journal of Chemical Physics* 123.6 (Aug. 2005).

[52] I. V. Tokatly. "Quantum many-body dynamics in a Lagrangian frame: I. Equations of motion and conservation laws". In: *Phys. Rev. B* 71 (16 Apr. 2005), p. 165104.

[53] I. V. Tokatly. "Quantum many-body dynamics in a Lagrangian frame: II. Geometric formulation of time-dependent density functional theory". In: *Phys. Rev. B* 71 (16 Apr. 2005), p. 165105.

[54] M. Lein and S. Kümmel. "Exact Time-Dependent Exchange-Correlation Potentials for Strong-Field Electron Dynamics". In: *Phys. Rev. Lett.* 94 (14 Apr. 2005), p. 143003.

[55] R. T. Sharp and G. K. Horton. "A variational approach to the unipotential many-electron problem". In: *Phys. Rev.* 90 (2 Apr. 1953), pp. 317–317.

[56] J. D. Talman and W. F. Shadwick. "Optimized effective atomic central potential". In: *Phys. Rev. A* 14 (1 July 1976), pp. 36–40.

[57] A. Görling and M. Levy. "Exact Kohn-Sham scheme based on perturbation theory". In: *Phys. Rev. A* 50 (1 July 1994), pp. 196–204.

[58] L. J. Sham and M. Schlüter. "Density-functional theory of the energy gap". In: *Phys. Rev. Lett.* 51 (20 Nov. 1983), pp. 1888–1891.

[59] M. E. Casida. "Generalization of the optimized-effective-potential model to include electron correlation: A variational derivation of the Sham-Schlüter equation for the exact exchange-correlation potential". In: *Phys. Rev. A* 51 (3 Mar. 1995), pp. 2005–2013.

[60] E. Engel and R. M. Dreizler. "From explicit to implicit density functionals". In: *Journal of Computational Chemistry* 20.1 (Jan. 1999), pp. 31–50.

[61] C. A. Ullrich, U. J. Gossmann, and E. K. U. Gross. "Time-dependent optimized effective potential". In: *Phys. Rev. Lett.* 74 (6 Feb. 1995), pp. 872–875.

[62] J. B. Krieger, Y. Li, and G. J. Iafrate. "Construction and application of an accurate local spin-polarized Kohn-Sham potential with integer discontinuity: Exchange-only theory". In: *Phys. Rev. A* 45 (1 Jan. 1992), pp. 101–126.

[63] J. B. Krieger, Y. Li, and G. J. Iafrate. "Derivation and application of an accurate Kohn-Sham potential with integer discontinuity". In: *Physics Letters A* 146.5 (May 1990), pp. 256–260.

[64] J. B. Krieger, Y. Li, and G. J. Iafrate. "Systematic approximations to the optimized effective potential: Application to orbital-density-functional theory". In: *Phys. Rev. A* 46 (9 Nov. 1992), pp. 5453–5458.

[65] T. Kreibich, E. K. U. Gross, and E. Engel. "Approximate relativistic optimized potential method". In: *Phys. Rev. A* 57 (1 Jan. 1998), pp. 138–148.

[66] M. A. L. Marques, A. Castro, and A. Rubio. "Assessment of exchange-correlation functionals for the calculation of dynamical properties of small clusters in time-dependent density functional theory". In: *Journal of Chemical Physics* 115.7 (Aug. 2001), pp. 3006–3014.

[67] S.-I. Chu. "Recent development of self-interaction-free time-dependent density-functional theory for nonperturbative treatment of atomic and molecular multiphoton processes in intense laser fields". In: *Journal of Chemical Physics* 123.6 (Aug. 2005), p. 062207.

[68] C. A. Ullrich, P.-G. Reinhard, and E. Suraud. "Simplified implementation of self-interaction correction in sodium clusters". In: *Phys. Rev. A* 62 (5 Oct. 2000), p. 053202.

[69] M. Mundt, S. Kümmel, R. van Leeuwen, and P.-G. Reinhard. "Violation of the zero-force theorem in the time-dependent Krieger-Li-Iafrate approximation". In: *Phys. Rev. A* 75 (5 May 2007), p. 050501.

[70] M. Baxter and T. Kirchner. "Time-dependent density-functional-theory studies of collisions involving He atoms: Extension of an adiabatic correlation-integral model". In: *Phys. Rev. A* 93 (1 Jan. 2016), p. 012502.

[71] M. Baxter. "Correlation in time-dependent density functional theory studies of antiproton-helium collisions". MA thesis. Toronto; Ontario: York University, Dec. 2012.

[72] C. Froese Fischer, T. Brage, and P. Jönsson. *Computational atomic structure: An MCHF approach*. Bristol, UK, UK: IOP Publishing Ltd., 1997.

[73] O. J. Kroneisen, H. J. Lüdde, T. Kirchner, and R. M. Dreizler. "The basis generator method: Optimized dynamical representation of the solution of time-dependent quantum problems". In: *Journal of Physics A: Mathematical and General* 32.11 (1999), p. 2141.

[74] M. Keim, A. Achenbach, H. J. Lüdde, and T. Kirchner. "Time-dependent density functional theory calculations for collisions of bare ions with helium". In: *Nuclear Instruments and Methods in Physics Research Section B: Beam Interactions with Materials and Atoms* 233.1–4 (2005). Fast Ion-Atom Collisions Proceedings of the eighth Workshop on Fast Ion-Atom Collisions Eighth Workshop on Fast Ion-Atom Collisions, pp. 240–243.

[75] E. J. Baerends, W. H. E. Schwarz, P. Schwerdtfeger, and J. G. Snijders. "Relativistic atomic orbital contractions and expansions: magnitudes and explanations". In: *Journal of Physics B: Atomic, Molecular and Optical Physics* 23.19 (1990), p. 3225.

[76] H.-C. Kao, T.-Y. Kuo, H.-P. Yen, C.-M. Wei, and K.-N. Huang. "Relativistic cross sections of electron-impact ionization of hydrogenic ions". In: *Phys. Rev. A* 45 (7 Apr. 1992), pp. 4646–4652.

[77] M. Keim, A. Achenbach, H. J. Lüdde, and T. Kirchner. "Microscopic response effects in collisions of antiprotons with helium atoms and lithium ions". In: *Phys. Rev. A* 67 (6 June 2003), p. 062711.

[78] T. Hahn. "CUBA–A library for multidimensional numerical integration". In: *Computer Physics Communications* 168.2 (2005), pp. 78 –95.

[79] W. Stich, H. J. Lüdde, and R. M. Dreizler. "Time-dependent Hartree-Fock description of one and two electron capture in collisions of $(He - He)^{2+}$". In: *Physics Letters A* 99.1 (1983), pp. 41 –45.

[80] G. R. Deco, J. M. Maidagan, and R. D. Rivarola. "Electron capture by proton and alpha particle impact on helium atoms". In: *Journal of Physics B: Atomic and Molecular Physics* 17.21 (1984), p. L707.

[81] W. Stich, H. J. Lüdde, and R. M. Dreizler. "TDHF calculations for two-electron systems". In: *Journal of Physics B: Atomic and Molecular Physics* 18.6 (1985), p. 1195.

[82] B. Gazdy and D. A. Micha. "Variational functional for transition amplitudes: Improving the time-dependent Hartree-Fock method". In: *Phys. Rev. A* 33 (6 June 1986), pp. 4446–4448.

[83] D. S. F. Crothers and R. McCarroll. "Correlated continuum distorted-wave resonant double electron capture in He^{2+}-He collisions". In: *Journal of Physics B: Atomic and Molecular Physics* 20.12 (1987), p. 2835.

[84] B. Gazdy and D. A. Micha. "Electron transfer and spin-flip processes in atom-atom collisions from variationally improved time-dependent Hartree-Fock results". In: *Phys. Rev. A* 36 (2 July 1987), pp. 546–556.

[85] A. Jain, C. D. Lin, and W. Fritsch. "State-selective double-electron capture in He^{2+} + He collisions at intermediate impact energies". In: *Phys. Rev. A* 39 (4 Feb. 1989), pp. 1741–1746.

[86] N. C. Deb and D. S. F. Crothers. "Double ionization of helium by alpha-particle impact". In: *Journal of Physics B: Atomic, Molecular and Optical Physics* 23.23 (1990), p. L799.

[87] N. C. Deb and D. S. F. Crothers. "Double ionization of helium by fully stripped ions in the independent-event model". In: *Journal of Physics B: Atomic, Molecular and Optical Physics* 24.9 (1991), p. 2359.

[88] K. M. Dunseath and D. S. F. Crothers. "Transfer and ionization processes during the collision of fast H^{+}, He^{2+} nuclei with helium". In: *Journal of Physics B: Atomic, Molecular and Optical Physics* 24.23 (1991), p. 5003.

[89] G. Deco and N. Grün. "An approximate description of the double capture process in He^{2+} +He collisions with static correlation". In: *Zeitschrift für Physik D Atoms, Molecules and Clusters* 18.4 (1991), pp. 339–343.

[90] K. J. Schaudt, N. H. Kwong, and J. D. Garcia. "Fully converged time-dependent Hartree-Fock results for He^{2+}-He: Correlation in inclusive charge transfer". In: *Phys. Rev. A* 43 (5 Mar. 1991), pp. 2294–2299.

[91] R. Singal and C. D. Lin. "Calculations of two-electron transition cross sections between fully stripped ions and helium atoms". In: *Journal of Physics B: Atomic, Molecular and Optical Physics* 24.1 (1991), p. 251.

[92] Y. R. Kuang. "Electron capture by protons and alpha particles from two-electron targets". In: *Journal of Physics B: Atomic, Molecular and Optical Physics* 25.1 (1992), p. 199.

[93] D. P. Marshall, C. Le Sechi, and D. S. F. Crothers. "Ionization of helium by alpha particles within the independent event model". In: *Journal of Physics B: Atomic, Molecular and Optical Physics* 26.8 (1993), p. L219.

[94] Z. Chen and A. Z. Msezane. "Calculation of the cross sections for positron- and proton-impact ionization of helium". In: *Phys. Rev. A* 49 (3 Mar. 1994), pp. 1752–1756.

[95] C. Chaudhuri, S. Sanyal, and T. K. Rai Dastidar. "Theoretical study of single and double charge transfer in He^{2+}-He collisions at kilo-electron-volt energies in a diabatic molecular representation". In: *Phys. Rev. A* 52 (2 Aug. 1995), pp. 1137–1142.

[96] B. Bhattacharjee, M. Das, N. C. Deb, and S. C. Mukherjee. "Two-electron capture by He^{2+}, Li^{3+}, and B^{5+} in the independent-event model". In: *Phys. Rev. A* 54 (4 Oct. 1996), pp. 2973–2976.

[97] A. E. Martínez, H. F. Busnengo, R. Gayet, J. Hanssen, and R. D. Rivarola. "Double electron capture in atomic collisions at intermediate and high collision energies: Contribution of capture into excited states". In: *Nuclear Instruments and Methods in Physics Research Section B: Beam Interactions with Materials and Atoms* 132.2 (1997). Atomic Collisions, pp. 344 –349.

[98] M. McCartney. "The double ionization of helium by ion impact". In: *Journal of Physics B: Atomic, Molecular and Optical Physics* 30.5 (1997), p. L155.

[99] M. McCartney. "Double ionisation of helium and lithium by ion impact using independent event models". In: *Nuclear Instruments and Methods in Physics Research Section B: Beam Interactions with Materials and Atoms* 155.4 (1999), pp. 343 –348.

[100] M. E. Galassi, P. N. Abufager, A. E. Martínez, R. D. Rivarola, and P. D. Fainstein. "The continuum distorted wave eikonal initial state model for transfer ionization in H^+, He^{2+} + He collisions". In: *Journal of Physics B: Atomic, Molecular and Optical Physics* 35.7 (2002), p. 1727.

[101] L. Gulyás, P. D. Fainstein, and T. Shirai. "Extended description for electron capture in ion-atom collisions: Application of model potentials within the framework of the continuum-distorted-wave theory". In: *Phys. Rev. A* 65 (5 May 2002), p. 052720.

[102] P. N. Abufager, A. E. Martínez, R. D. Rivarola, and P. D. Fainstein. "CDW-EIS model for single-electron capture in ion–atom collisions involving multielectronic targets". In: *Journal of Physics B: Atomic, Molecular and Optical Physics* 37.4 (2004), p. 817.

[103] J. Bradley, R. J. S. Lee, M. McCartney, and D. S. F. Crothers. "Multi-ionization of helium and lithium using the independent electron and independent event models with intrinsic CDW". In: *Journal of Physics B: Atomic, Molecular and Optical Physics* 37.18 (2004), p. 3723.

[104] M. Fiori, A. B. Rocha, C. E. Bielschowsky, G. Jalbert, and C. R. Garibotti. "Double ionization of atoms by ion impact: two-step models". In: *Journal of Physics B: Atomic, Molecular and Optical Physics* 39.7 (2006), p. 1751.

[105] M. Fiori, G. Jalbert, and C. R. Garibotti. "Double ionization of He and Li by ion impact: Final state correlation". In: *Journal of Electron Spectroscopy and Related Phenomena* 161.1–3 (2007), pp. 191 –193.

[106] L. Gulyás, A. Igarashi, P. D. Fainstein, and T. Kirchner. "Single and double ionization of helium: The axial symmetry". In: *Journal of Physics B: Atomic, Molecular and Optical Physics* 41.2 (2008), p. 025202.

[107] M. Zapukhlyak and T. Kirchner. "Projectile angular-differential cross sections for electron transfer processes in ion-helium collisions: Evidence for the applicability of the independent electron model". In: *Phys. Rev. A* 80 (6 Dec. 2009), p. 062705.

[108] E. Ghanbari-Adivi. "Coulomb–Born distorted wave approximation applied to the proton–helium single-electron capture process". In: *Journal of Physics B: Atomic, Molecular and Optical Physics* 44.16 (2011), p. 165204.

[109] S. D. López, M. Fiori, and C. R. Garibotti. "Analysis of the approximations applied in the continuum-distorted-wave–eikonal-initial-state theory for the evaluation of ionization cross sections: Post-prior discrepancy, axial symmetry, and ion-ion interaction". In: *Phys. Rev. A* 83 (3 Mar. 2011), p. 032716.

[110] E. Ghanbari-Adivi and H. Ghavaminia. "Electron capture by alpha particles from helium atoms in a Coulomb–Born distorted-wave approximation". In: *Journal of Physics B: Atomic, Molecular and Optical Physics* 45.23 (2012), p. 235202.

[111] D. Zajfman and D. Maor. ""Heisenberg core" in classical-trajectory Monte Carlo calculations of ionization and charge exchange". In: *Phys. Rev. Lett.* 56 (4 Jan. 1986), pp. 320–323.

[112] R. E. Olson, A. E. Wetmore, and M. L. McKenzie. "Double electron transitions in collisions between multiply charged ions and helium atoms". In: *Journal of Physics B: Atomic and Molecular Physics* 19.18 (1986), p. L629.

[113] M. L. McKenzie and R. E. Olson. "Ionization and charge exchange in multiply-charged-ion – helium collisions at intermediate energies". In: *Phys. Rev. A* 35 (7 Apr. 1987), pp. 2863–2868.

[114] A. E. Wetmore and R. E. Olson. "Electron loss from helium atoms by collisions with fully stripped ions". In: *Phys. Rev. A* 38 (11 Dec. 1988), pp. 5563–5570.

[115] V. J. Montemayor and G. Schiwietz. "Dynamic target screening for two-active-electron classical-trajectory Monte Carlo calculations for $H^+ + He$ collisions". In: *Phys. Rev. A* 40 (11 Dec. 1989), pp. 6223–6230.

[116] J. S. Cohen. "Quasiclassical-trajectory Monte Carlo methods for collisions with two-electron atoms". In: *Phys. Rev. A* 54 (1 July 1996), pp. 573–586.

[117] K. Tőkési and G. Hock. "Double electron capture in He^{2+}-He collisions up to 1500 keV/amu projectile impact". In: *Journal of Physics B: Atomic, Molecular and Optical Physics* 29.4 (1996), p. L119.

[118] S. Morita, N. Matsuda, N. Toshima, and K. Hino. "Ionization of stabilized helium atoms by proton and antiproton impacts". In: *Phys. Rev. A* 66 (4 Oct. 2002), p. 042719.

[119] K. Dimitriou, F. Aumayr, K. Katsonis, and H. P. Winter. "H^+–$He(1s^2)$ collisions: CTMC calculations of single ionisation and excitation cross sections". In: *International Journal of Mass Spectrometry* 233.1–3 (2004). Special Issue: In honour of Tilmann Mark, pp. 137 –144.

[120] F. Guzmán, L. F. Errea, and B. Pons. "Two active-electron classical trajectory Monte Carlo methods for ion-He collisions". In: *Phys. Rev. A* 80 (4 Oct. 2009), p. 042708.

[121] B. W. Ding, D. Y. Yu, and X. M. Chen. "Cross sections for transfer ionization in ion-helium collisions". In: *Nuclear Instruments and Methods in Physics Research Section B: Beam Interactions with Materials and Atoms* 266.6 (2008), pp. 886 –888.

[122] B. Ding. "Absolute cross-sections in collisions of ions with helium atoms at low and intermediate energies". In: *Physica Scripta* 85.1 (2012), p. 015302.

[123] R. D. DuBois, L. H. Toburen, and M. E. Rudd. "Multiple ionization of rare gases by H^+ and He^+ impact". In: *Phys. Rev. A* 29 (1 Jan. 1984), pp. 70–76.

[124] E. S. Solovev, R. N. Ilin, V. A. Oparin, and N. V. Fedorenko. "Ionization of gases by fast hydrogen atoms and by protons". In: *Soviet Physics JETP-USSR* 15.3 (1962), pp. 459–464.

[125] M. B. Shah, P. McCallion, and H. B. Gilbody. "Electron-capture and ionization in collisions of slow H^+ and He^{2+} ions with helium". In: *Journal of Physics B-Atomic Molecular and Optical Physics* 22.19 (Oct. 1989), pp. 3037–3045.

[126] M. B. Shah and H. B. Gilbody. "Single and double ionization of helium by H^+, He^{2+}, and Li^{3+} ions". In: *Journal of Physics B-Atomic Molecular and Optical Physics* 18.5 (1985), pp. 899–913.

[127] L. J. Puckett and D. W. Martin. "Analysis of Recoil He^+ and He^{++} Ions Produced by Fast Protons in Helium Gas". In: *Phys. Rev. A* 1 (5 May 1970), pp. 1432–1439.

[128] S. Wexler. "Partial ionization cross sections for noble gases bombarded with 0.8-3.75-MeV protons". In: *Journal of Chemical Physics* 41.6 (1964), p. 1714.

[129] H. Knudsen, L. H. Andersen, P. Hvelplund, G. Astner, H. Cederquist, H. Danared, L. Liljeby, and K. G. Rensfelt. "An experimental investigation of double ionization of helium-atoms in collisions with fast, fully stripped ions". In: *Journal of Physics B-Atomic Molecular and Optical Physics* 17.17 (1984), pp. 3545–3564.

[130] H. Knudsen, H.-P. E. Kristiansen, H. D. Thomsen, U. I. Uggerhøj, T. Ichioka, S. P. Møller, C. A. Hunniford, R. W. McCullough, M. Charlton, N. Kuroda, Y. Nagata, H. A. Torii, Y. Yamazaki, H. Imao, H. H. Andersen, and K. Tőkési. "Ionization of helium and argon by very slow antiproton impact". In: *Phys. Rev. Lett.* 101 (4 July 2008), p. 043201.

[131] P. Hvelplund, H. Knudsen, U. Mikkelsen, E. Morenzoni, S. P. Møller, E. Uggerhøj, and T. Worm. "Ionization of helium and molecular-hydrogen by slow antiprotons". In: *Journal of Physics B-Atomic Molecular and Optical Physics* 27.5 (Mar. 1994), pp. 925–934.

[132] L. H. Andersen, P. Hvelplund, H. Knudsen, S. P. Møller, J. O. P. Pedersen, S. Tangpetersen, E. Uggerhøj, K. Elsener, and E. Morenzoni. "Single ionization of helium by 40-3000-keV antiprotons". In: *Physical Review A* 41.11 (June 1990), pp. 6536–6539.

[133] H. Knudsen, H.-P. E. Kristiansen, H. D. Thomsen, U. I. Uggerhoj, T. Ichioka, S. P. Moller, C. A. Hunniford, R. W. McCullough, M. Charlton, N. Kuroda, Y. Nagata, H. A. Torii, Y. Yamazaki, H. Imao, H. H. Andersen, and K. Tőkési. "On the double ionization of helium by very slow antiproton impact". In: *Nuclear Instruments and Methods in Physics*

Research Section B-Beam Interactions With Materials and Atoms 267.2 (Jan. 2009), pp. 244–247.

[134] T. Kirchner and H. Knudsen. "Current status of antiproton impact ionization of atoms and molecules: Theoretical and experimental perspectives". In: *Journal of Physics B: Atomic, Molecular and Optical Physics* 44.12 (2011), p. 122001.

[135] S. Borbély, J. Feist, K. Tőkési, S. Nagele, L. Nagy, and J. Burgdörfer. "Ionization of helium by slow antiproton impact: Total and differential cross sections". In: *Phys. Rev. A* 90 (5 Nov. 2014), p. 052706.

[136] M. Kimura and C. D. Lin. "Charge transfer and excitation processes in *p*-He collisions studied using a unified atomic-orbital – molecular-orbital matching method". In: *Phys. Rev. A* 34 (1 July 1986), pp. 176–184.

[137] S. Jana, C. R. Mandal, and M. Purkait. "Four-body charge transfer processes in collisions of bare projectile ions with helium atoms". In: *Journal of Physics B: Atomic, Molecular and Optical Physics* 48.4 (2015), p. 045203.

[138] A. L. Godunov, J. H. McGuire, V. S. Schipakov, H. R. J. Walters, and C. T. Whelan. "Total cross sections for transfer ionization in fast ion–helium collisions". In: *Journal of Physics B: Atomic, Molecular and Optical Physics* 39.4 (2006), p. 987.

[139] A. L. Ford and J. F. Reading. "Improved forced impulse method calculations of single and double ionization of helium by collision with high-energy protons and antiprotons". In: *Journal of Physics B: Atomic, Molecular and Optical Physics* 27.18 (1994), p. 4215.

[140] H. A. Slim, E. L. Heck, B. H. Bransden, and D. R. Flower. "Ionization and charge transfer in proton-helium collisions". In: *Journal of Physics B: Atomic, Molecular and Optical Physics* 24.17 (1991), p. L421.

[141] T. G. Winter. "Electron transfer and ionization in proton-helium collisions studied using a Sturmian basis". In: *Phys. Rev. A* 44 (7 Oct. 1991), pp. 4353–4367.

[142] C. Díaz, F. Martín, and A. Salin. "The role of dynamic correlation in double ionization of He by high-energy protons and antiprotons". In: *Journal of Physics B: Atomic, Molecular and Optical Physics* 33.20 (2000), p. 4373.

[143] D. Belkić and I. Mančev. "Transfer ionization in fast ion-atom collisions: Four-body Born distorted-wave theory". In: *Phys. Rev. A* 83 (1 Jan. 2011), p. 012703.

[144] K. Gramlich, N. Grün, and W. Scheid. "Coupled-channel calculations with Gauss-type orbitals for charge transfer and ionisation in collisions of the (He-He)$^{2+}$ system". In: *Journal of Physics B: Atomic, Molecular and Optical Physics* 22.16 (1989), p. 2567.

[145] I. F. Barna, K. Tőkési, and J. Burgdörfer. "Single and double ionization of helium in heavy-ion impact". In: *Journal of Physics B: Atomic, Molecular and Optical Physics* 38.7 (2005), p. 1001.

[146] M. S. Pindzola, F. Robicheaux, and J. Colgan. "Double ionization of helium by fast bare ion collisions". In: *Journal of Physics B: Atomic, Molecular and Optical Physics* 40.10 (2007), p. 1695.

[147] R. D. DuBois. "Ionization and charge transfer in He^{2+}–rare-gas collisions. II". In: *Phys. Rev. A* 36 (6 Sept. 1987), pp. 2585–2593.

[148] D. Belkić, I. Mančev, and V. Mergel. "Four-body model for transfer ionization in fast ion-atom collisions". In: *Phys. Rev. A* 55 (1 Jan. 1997), pp. 378–395.

[149] W. Fritsch. "Theoretical study of electron processes in slow He^{2+}-He collisions". In: *Journal of Physics B: Atomic, Molecular and Optical Physics* 27.15 (1994), p. 3461.

[150] M. E. Rudd, T. V. Goffe, and A. Itoh. "Ionization cross sections for 10 – 300-keV/u and electron-capture cross sections for 5 – 150-keV/u ^{3}He^{2+} ions in gases". In: *Phys. Rev. A* 32 (4 Oct. 1985), pp. 2128–2133.

[151] S. Ghosh, A. Dhara, C. R. Mandal, and M. Purkait. "Double-electron-capture cross sections from helium by fully stripped projectile ions in intermediate-to-high energies". In: *Phys. Rev. A* 78 (4 Oct. 2008), p. 042708.

[152] M. B. Shah and H. B. Gilbody. "Formation of He^{+} (2S) metastable ions in passage of 10-60 keV ^{3}He^{2+} ions through gases". In: *Journal of Physics B: Atomic and Molecular Physics* 7.2 (1974), p. 256.

[153] M. Baxter, T. Kirchner, and E. Engel. "Time-dependent spin-density-functional-theory description of He^{+}-He collisions". In: *Phys. Rev. A* 96 (3 Sept. 2017), p. 032708.

[154] E. Engel, A. Höck, and R. M. Dreizler. "Accuracy of the Krieger-Li-Iafrate approximation for molecules". In: *Phys. Rev. A* 62 (4 Sept. 2000), p. 042502.

[155] M. Zapukhlyak, T. Kirchner, H. J. Lüdde, S. Knoop, R. Morgenstern, and R. Hoekstra. "Inner- and outer-shell electron dynamics in proton collisions with sodium atoms". In: *Journal of Physics B: Atomic, Molecular and Optical Physics* 38.14 (2005), p. 2353.

[156] H. J. Lüdde and R. M. Dreizler. "Comment on inclusive cross sections". In: *Journal of Physics B: Atomic and Molecular Physics* 18.1 (1985), p. 107.

[157] R. E. Miers, A. S. Schlachter, and L. W. Anderson. "Production and Loss of Fast Metastable Helium Atoms in Collisions with Xe, H_2, Ar, and He". In: *Phys. Rev.* 183 (1 July 1969), pp. 213–216.

[158] S. K. Allison. "Experimental Results on Charge-Changing Collisions of Hydrogen and Helium Atoms and Ions at Kinetic Energies above 0.2 kev". In: *Rev. Mod. Phys.* 30 (4 Oct. 1958), pp. 1137–1168.

[159] T. Kirchner, A. C. F. Santos, H. Luna, M. M. Sant'Anna, W. S. Melo, G. M. Sigaud, and E. C. Montenegro. "Charge-state-correlated cross sections for electron loss, capture, and ionization in C^{3+}-Ne collisions". In: *Phys. Rev. A* 72 (1 July 2005), p. 012707.

[160] M. Murakami, T. Kirchner, M. Horbatsch, and H. J. Lüdde. "Single and multiple electron removal processes in proton–water-molecule collisions". In: *Phys. Rev. A* 85 (5 May 2012), p. 052704.

[161] G. Schenk and T. Kirchner. "Multiple ionization of neon atoms in collisions with bare and dressed ions: A mean-field description considering target response". In: *Phys. Rev. A* 91 (5 May 2015), p. 052712.

[162] C. A. Hall and W. W. Meyer. "Optimal error bounds for cubic spline interpolation". In: *journal of approximation theory* 16.2 (1976), pp. 105–122.

[163] D. L. Guo, X. Ma, R. T. Zhang, S. F. Zhang, X. L. Zhu, W. T. Feng, Y. Gao, B. Hai, M. Zhang, H. B. Wang, and Z. K. Huang. "State-selective electron capture in 30- and 100-keV He^+ + He collisions". In: *Phys. Rev. A* 95 (1 Jan. 2017), p. 012707.

[164] L. Chen and X. Chen. "One and two electron transitions in multiply charged ions and helium collisions". In: *Nuclear instruments and methods in physics research section B: Beam interactions with materials and atoms* 262.1 (Aug. 2007), pp. 33–38.

[165] B. Ding, H. Li, and W. Zhang. "Electron loss accompanied by target ionization for He+ and Li2+ on H and He in low- to intermediate-energy regime". In: *International Journal of Mass Spectrometry* 313 (2012), pp. 41–46.

[166]   J. E. Miraglia and M. S. Gravielle. "Ionization of He, Ne, Ar, Kr, and Xe by impact of He$^+$ ions". In: *Phys. Rev. A* 81 (4 Apr. 2010), p. 042709.

[167]   R. D. DuBois. "Multiple ionization in He$^+$–rare-gas collisions". In: *Phys. Rev. A* 39 (9 May 1989), pp. 4440–4450.

[168]   J. L. Forest, J. A. Tanis, S. M. Ferguson, R. R. Haar, K. Lifrieri, and V. L. Plano. "Single and double ionization of helium by intermediate-to-high-velocity He$^+$ projectiles". In: *Phys. Rev. A* 52 (1 July 1995), pp. 350–356.

[169]   R. D. DuBois and L. H. Toburen. "Single and double ionization of helium by neutral-particle to fully stripped ion impact". In: *Phys. Rev. A* 38 (8 Oct. 1988), pp. 3960–3968.

[170]   G. M. Sigaud and E. C. Montenegro. "Two-center electron-electron correlation within the independent event model". en. In: *Brazilian Journal of Physics* 33 (June 2003), pp. 382 –391.

[171]   E. Ghanbari-Adivi and H. Ghavaminia. "Projectile angular-differential cross sections for single electron transfer in fast He$^+$-He collisions". In: *Chinese Physics B* 24.3 (Mar. 2015).

[172]   A. C. F. Santos, G. M. Sigaud, W. S. Melo, M. M. Sant'Anna, and E. C. Montenegro. "Absolute cross sections for projectile electron loss accompanied by target multiple ionization in collisions of He$^+$ with noble gases". In: *Journal of Physics B: Atomic, Molecular and Optical Physics* 44.4 (2011), p. 045202.

[173]   G. Schenk. "On the role of projectile electrons in an independent electron model description of dressed-ion impact on atoms". PhD thesis. Toronto; Ontario: York University, June 2016.

[174]   M. E. Rudd, T. V. Goffe, A. Itoh, and R. D. DuBois. "Cross sections for ionization of gases by 10–2000-keV He$^+$ ions and for electron capture and loss by 5–350-keV He$^+$ ions". In: *Phys. Rev. A* 32 (2 Aug. 1985), pp. 829–835.

[175]   I. Mančev. "Single-electron capture by hydrogen atoms and helium ions from helium atoms". In: *Phys. Rev. A* 54 (1 July 1996), pp. 423–431.

[176]   J. Bradley, S. F. C. O'Rourke, and D. S. F. Crothers. "Total and single differential cross sections for simple resonant collisions using a fully orthonormal continuum-distorted-wave basis". In: *Phys. Rev. A* 71 (3 Mar. 2005), p. 032706.

[177] I. Mančev. "Four-body continuum-distorted-wave model for charge exchange between hydrogenlike projectiles and atoms". In: *Phys. Rev. A* 75 (5 May 2007), p. 052716.

[178] N. V. Novikov, Y. A. Teplova, and V. S. Cherhysh. "Cross section for the single-electron capture by fast He^+ ions in inert gases". In: *Nuclear Instruments and Methods in Physics Research Section B: Beam Interactions with Materials and Atoms* 269.9 (2011), pp. 834 –836.

[179] E. Ghanbari-Adivi and H. Ghavaminia. "Single-electron capture from helium atoms by fast singly positive charged helium ions". In: *The European Physical Journal D* 66.12 (Dec. 2012), pp. 1–7.

[180] J. Loreau, S. Ryabchenko, and N. Vaeck. "Charge transfer in proton–helium collisions from low to high energy". In: *Journal of Physics B: Atomic, Molecular and Optical Physics* 47.13 (2014), p. 135204.

[181] Y. Suzuki, L. Lacombe, K. Watanabe, and N. T. Maitra. "Exact time-dependent exchange-correlation potential in electron scattering processes". In: (Aug. 2017). arXiv: arXiv:1708.08651 [physics.chem-ph].

[182] G. A. Korn and T. M. Korn. *Mathematical handbook for scientists and engineers: definitions, theorems, and formulas for reference and review*. Mineola, New York: Dover Publications, 2000.

[183] D. A. Polyanin and A. V. Manzhirov. *Handbook of mathematics for engineers and scientists*. Boca Raton, Florida: Chapman & Hall/CRC, 2007.

[184] A. C. Hindmarsh. *ODEPACK, A systematized collection of ODE solvers*. Ed. by R. S. Stepleman. Vol. 1. 1983, pp. 55–64.

[185] K. Radhakrishnan and A. C. Hindmarsh. *Description and Use of LSODE, the Livermore solver for ordinary differential equations*. Tech. rep. 1993.

[186] S.-j. Wang and W. Cassing. "Explicit treatment of N-body correlations within a density-matrix formalism". In: *Annals of Physics* 159.2 (1985), pp. 328 –350.

Appendix A

Coordinate Systems

This appendix contains the fundamentals of some non-rectangular coordinate systems used in the text. This discussion focuses on lesser known coordinate systems. For more detail the reader is referred to any mathematical handbook for physics, for example [182, 183].

A.1 Elliptical Coordinates

Elliptical coordinates are formed by the intersection of series of confocal ellipses and hyperboles. If we let (ξ, η) denote the elliptic and hyperbolic grid lines and $a > 0$ their focal length we can cover the plane with two charts. The first is given by

$$\begin{cases} x = a\xi\eta \\ y^2 = a\left(\xi^2 - 1\right)\left(1 - \eta^2\right), \end{cases} \tag{A.1}$$

while the second is defined similarly and covers the lower half space $((\xi, \eta) \mapsto (x, -y))$. Both charts are defined for $(\xi, \eta) \in [1, \infty] \times [-1, 1]$ and $a = \frac{R}{2}$.

This mapping is demonstrated in Fig. A.1. The coloured lines in the left panel represent a selection of ξ (blues and greens) and η (reds and oranges) grid lines. Grid lines are mapped by Eq. (A.1) to lines of corresponding colour in the right panel.
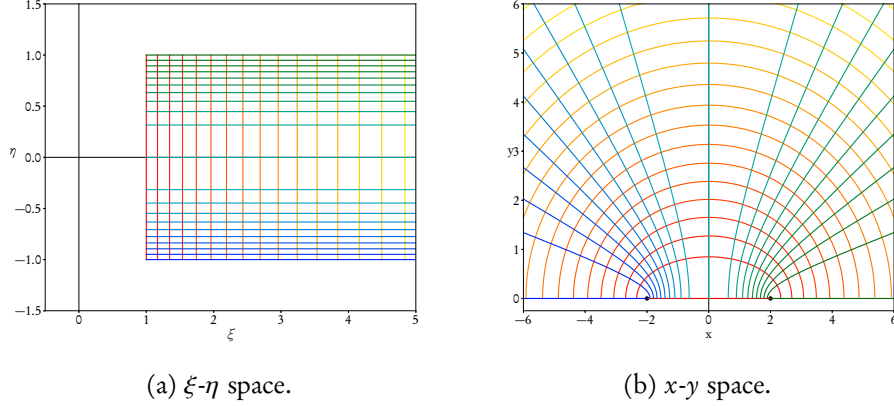
(a) ξ-η space.

(b) x-y space.

Figure A.1: The coordinate mapping of Eq. (A.1) is demonstrated by the correspondence between coloured grid lines.

A.2 Prolate Spheroidal Coordinates

Prolate spheroidal coordinates are a three-dimensional coordinate system that result from rotating the upper half space elliptical coordinates (defined in the proceeding section) around the line running through the co-foci of the elliptic and hyperbolic grid lines.

While several conventions exist, throughout this work prolate spheroidal coordinates are defined as

$$\begin{cases} x = a\sqrt{(\xi^2 - 1)(1 - \eta^2)} \sin \phi, \\ y = a\sqrt{(\xi^2 - 1)(1 - \eta^2)} \cos \phi, \\ z = a\xi\eta, \end{cases} \tag{A.2}$$

for $(\xi, \eta, \phi) \in [1, \infty) \times [-1, 1] \times [0, 2\pi)$.

One says that a function $f : \mathbb{R}^3 \to \mathbb{R}$ is cylindrically symmetric if it has no ϕ dependence, i.e. if $f(\xi, \eta, \phi) = f(\xi, \eta)$.

APPENDIX B

COMPUTATIONAL ASPECTS

In this appendix details of the code used to calculate the results presented in Sec. 4.3 are presented. This code is an amalgam of several components. These consist primarily of the code base developed for carrying out TC-BGM collision calculations, here referred to as BGM, the ground-state DFT structure code, DIAMOL, which can be used to produce a KS-potential for a given arrangement of a diatomic molecule, and a short programme, `hephe.py` which manages the execution of a single run.

Both BGM and DIAMOL are mature stand-alone programmes. While this makes them well suited to performing their intended function it also makes them somewhat less adaptable. With this in mind the design philosophy behind the development of a hybrid code proceeded from a desire to modify the existing code as little as possible. Essentially the only modifications made to the DIAMOL were to replace a subroutine which calculates the KS-orbitals with one which reads the orbitals from a file output by BGM. Similarly the BGM was altered to output orbitals to be fed into DIAMOL and to read in potentials output by DIAMOL. Additionally execution control was added to BGM which causes it to pause and wait for a signal to proceed at each time step, this allows time for a new potential to be calculated as necessary.

These pieces are monitored and controlled by `hephe.py`. This script serves several purposes. First, it sets up the input files needed by BGM and launches

two child threads. Each thread contains an instance of `BGM`, one for the spin-up electrons and another for spin-down. As these run `hephe.py` monitors their outputs for a flag which indicates that they are ready to receive a new potential. At this point the `BGM` instances are paused and input files needed for `DIAMOL` are generated from their outputs. Once `DIAMOL` has completed its execution the `BGM` threads are resumed. The `BGM` proceeds by expanding the KS-orbitals in the basis described in Sec. 4.1, the resulting coupled-channel equations are then solved using the Livermore solver [184, 185] which employs either an Adams method (predictor-corrector) in the case of non-stiff systems or a backward differentiation formula in the case of stiff systems. In this way the KS-orbitals are propagated in a time-dependent potential.

Appendix C

Three-Electron Correlation Integrals

The process of deriving three-electron versions of the equations presented in Sec. 3.2 begins as it did in the two electron state with the full N-body wave function. Unlike in the former case the wave function is not readily split into spatial and spin components. One is then forced to work with the function $\Psi(\mathbf{r}_1, \sigma_1, \mathbf{r}_2, \sigma_2, \mathbf{r}_3, \sigma_3, t)$. Our notation may be simplified by introducing combined spatial-spin coordinates $\mathbf{x}_j = (\mathbf{r}_j, \sigma_j)$ and a combined integral operator

$$\fint_V d^3x = \sum_{\sigma=\uparrow,\downarrow} \int_V d^3r. \tag{C.1}$$

With a slight modification to the definition of the one-particle density

$$n(\mathbf{x}) = N \fint d^3x_2 \ldots d^3x_N \, |\Psi(\mathbf{x}, \mathbf{x}_2, \ldots, \mathbf{x}_N, t)|^2 \tag{C.2}$$

the single-particle probabilities to find an electron on the target or the projectile may be obtained

$$p_T = \frac{1}{3} \fint_T n(\mathbf{x}, t_f) \, d^3x \tag{C.3}$$

and

$$p_P = \frac{1}{3} \oint_P n(\mathbf{x}, t_f) \, d^3x. \tag{C.4}$$

In addition to these probabilities we will define two varieties of correlation integral, one that involves three-particle interactions

$$I_c^{V_1 V_2 V_3} = \oint_{V_1} \oint_{V_2} \oint_{V_3} d^3x_1 d^3x_2 d^3x_3 \, g_c^{(3)}(\mathbf{x}_1, \mathbf{x}_2, \mathbf{x}_3, t) n(\mathbf{x}_1, t) n(\mathbf{x}_2, t) n(\mathbf{x}_3, t), \tag{C.5}$$

$$g_c^{(3)}(\mathbf{x}_1, \mathbf{x}_2, \mathbf{x}_3, t) = \frac{\rho(\mathbf{x}_1, \mathbf{x}_2, \mathbf{x}_3, t)}{n(\mathbf{x}_1, t) n(\mathbf{x}_2, t) n(\mathbf{x}_3, t)} - \frac{1}{9} \tag{C.6}$$

and a more familiar two-particle version

$$I_c^{V_1 V_2} = \oint_{V_1} \oint_{V_2} d^3x_1 d^3x_2 \, g_c^{(2)}(\mathbf{x}_1, \mathbf{x}_2, t) n(\mathbf{x}_1, t) n(\mathbf{x}_2, t), \tag{C.7}$$

$$g_c^{(2)}(\mathbf{x}_1, \mathbf{x}_2, t) = \frac{\rho_2(\mathbf{x}_1, \mathbf{x}_2, t)}{n(\mathbf{x}_1, t) n(\mathbf{x}_2, t)} - \frac{1}{3} \tag{C.8}$$

where V_1, V_2, and $V_3 \in \{T, P, I\}$, $\rho = 3|\psi|^2$, and $\rho_2 = \oint d^3x \rho$.

With these definitions established the ten outcome probabilities, p_{kl}, detailed in Sec. 4.2

$$p_{00} = \frac{1}{3} \oint_T \oint_T \oint_T \rho(\mathbf{x}_1, \mathbf{x}_2, \mathbf{x}_3, t_f) \, d^3x_1 d^3x_2 d^3x_3, \tag{C.9a}$$

$$p_{01} = \oint_T \oint_T \oint_I \rho(\mathbf{x}_1, \mathbf{x}_2, \mathbf{x}_3, t_f) \, d^3x_1 d^3x_2 d^3x_3, \tag{C.9b}$$

$$p_{02} = \oint_T \oint_I \oint_I \rho(\mathbf{x}_1, \mathbf{x}_2, \mathbf{x}_3, t_f) \, d^3x_1 d^3x_2 d^3x_3, \tag{C.9c}$$

$$p_{03} = \frac{1}{3} \oint_I \oint_I \oint_I \rho(\mathbf{x}_1, \mathbf{x}_2, \mathbf{x}_3, t_f) \, d^3x_1 d^3x_2 d^3x_3, \tag{C.9d}$$

$$p_{10} = \oint_T \oint_T \oint_P \rho(\mathbf{x}_1, \mathbf{x}_2, \mathbf{x}_3, t_f) \, d^3x_1 d^3x_2 d^3x_3, \tag{C.9e}$$

$$p_{11} = 2 \oint_T \oint_P \oint_I \rho(\mathbf{x}_1, \mathbf{x}_2, \mathbf{x}_3, t_f) \, d^3x_1 d^3x_2 d^3x_3, \tag{C.9f}$$

$$p_{12} = \oint_P \oint_I \oint_I \rho(\mathbf{x}_1, \mathbf{x}_2, \mathbf{x}_3, t_f) \, d^3x_1 d^3x_2 d^3x_3, \tag{C.9g}$$

$$p_{20} = \oint_T \oint_P \oint_P \rho(\mathbf{x}_1, \mathbf{x}_2, \mathbf{x}_3, t_f)\, \mathrm{d}^3 x_1 \mathrm{d}^3 x_2 \mathrm{d}^3 x_3, \qquad \text{(C.9h)}$$

$$p_{21} = \oint_P \oint_P \oint_I \rho(\mathbf{x}_1, \mathbf{x}_2, \mathbf{x}_3, t_f)\, \mathrm{d}^3 x_1 \mathrm{d}^3 x_2 \mathrm{d}^3 x_3, \qquad \text{(C.9i)}$$

$$p_{30} = \frac{1}{3} \oint_P \oint_P \oint_P \rho(\mathbf{x}_1, \mathbf{x}_2, \mathbf{x}_3, t_f)\, \mathrm{d}^3 x_1 \mathrm{d}^3 x_2 \mathrm{d}^3 x_3, \qquad \text{(C.9j)}$$

may be rewritten as

$$p_{00} = p_T{}^3 + \frac{1}{3} I_{\mathrm{c}}^{TTT}, \qquad \text{(C.10a)}$$

$$p_{01} = 3p_T{}^2(1 - p_T - p_P) + I_{\mathrm{c}}^{TT} - I_{\mathrm{c}}^{TTT} - I_{\mathrm{c}}^{TTP}, \qquad \text{(C.10b)}$$

$$p_{02} = 3p_T(1 - p_T - p_P)^2 - 2I_{\mathrm{c}}^{TT} - 2I_{\mathrm{c}}^{TP} + I_{\mathrm{c}}^{TTT} + 2I_{\mathrm{c}}^{TTP} + I_{\mathrm{c}}^{TPP}, \qquad \text{(C.10c)}$$

$$p_{03} = (1 - p_T - p_P)^3 + I_{\mathrm{c}}^{TT} + 2I_{\mathrm{c}}^{TP} + I_{\mathrm{c}}^{PP} - \frac{1}{3} I_{\mathrm{c}}^{TTT} - I_{\mathrm{c}}^{TTP} - I_{\mathrm{c}}^{TPP} - \frac{1}{3} I_{\mathrm{c}}^{PPP}, \qquad \text{(C.10d)}$$

$$p_{10} = 3p_T{}^2 p_P + I_{\mathrm{c}}^{TTP}, \qquad \text{(C.10e)}$$

$$p_{11} = 6p_T p_P(1 - p_T - p_P) + 2I_{\mathrm{c}}^{TP} - 2I_{\mathrm{c}}^{TTP} - 2I_{\mathrm{c}}^{TPP}, \qquad \text{(C.10f)}$$

$$p_{12} = 3p_P(1 - p_T - p_P)^2 - 2I_{\mathrm{c}}^{TP} - 2I_{\mathrm{c}}^{PP} + I_{\mathrm{c}}^{TTP} + 2I_{\mathrm{c}}^{TPP} + I_{\mathrm{c}}^{PPP}, \qquad \text{(C.10g)}$$

$$p_{20} = 3p_T p_P{}^2 + I_{\mathrm{c}}^{TPP}, \qquad \text{(C.10h)}$$

$$p_{21} = 3p_P{}^2(1 - p_T - p_P) + I_{\mathrm{c}}^{PP} - I_{\mathrm{c}}^{TPP} - I_{\mathrm{c}}^{PPP}, \qquad \text{(C.10i)}$$

$$p_{30} = p_P{}^3 + \frac{1}{3} I_{\mathrm{c}}^{PPP}. \qquad \text{(C.10j)}$$

Just like in the two-electron case the IEM may be recovered by setting all correlation integrals to zero. One finds

$$p_{00}^{\mathrm{IEM}} = p_T{}^3, \qquad \text{(C.11a)}$$

$$p_{01}^{\mathrm{IEM}} = 3p_T{}^2(1 - p_T - p_P), \qquad \text{(C.11b)}$$

$$p_{02}^{\mathrm{IEM}} = 3p_T(1 - p_T - p_P)^2, \qquad \text{(C.11c)}$$

$$p_{03}^{\mathrm{IEM}} = (1 - p_T - p_P)^3, \qquad \text{(C.11d)}$$

$$p_{10}^{\mathrm{IEM}} = 3p_T{}^2 p_P, \qquad \text{(C.11e)}$$

$$p_{11}^{\text{IEM}} = 6 p_T p_P (1 - p_T - p_P), \tag{C.11f}$$

$$p_{12}^{\text{IEM}} = 3 p_P (1 - p_T - p_P)^2, \tag{C.11g}$$

$$p_{20}^{\text{IEM}} = 3 p_T p_P{}^2, \tag{C.11h}$$

$$p_{21}^{\text{IEM}} = 3 p_P{}^2 (1 - p_T - p_P), \tag{C.11i}$$

$$p_{30}^{\text{IEM}} = p_P{}^3. \tag{C.11j}$$

Moving beyond an IEM description may prove difficult. The failings of the WB model, discussed in Chap. 3, essentially preclude its application in this more complex setting. Any new model envisioned may be aided in part by relations between the full three-particle density and its various reductions (see for example Ref. [186]).